

Chapter 1

Introduction

1.1 Information storage

Technological revolutions in many fronts of information technology, such as portable computing, information management, and communication devices create a huge and growing demand for higher capacity, long data retention, faster access, higher data transfer rate, low power consumption, and low cost data storage systems. Modern computer systems have a memory hierarchy consisting of CPU registers, external caches, hard drives, and removable storage devices. All the memory devices have shown significant improvements to meet the demand mentioned above. Generally, the memory hierarchy follows the access time with the fast CPU registers at the top and the slow hard drive and removable storage at the bottom. At the hierarchy level of hard drive, almost all the data must be stored non-volatile, and high capacity with quite low cost per bit has priority over the access and write times. Magnetic materials contribute greatly to provide hard drive, since they have features of non-volatility and long-range magnetic interaction. These features enable to manufacture hard disk drive (HDD) with huge storage density while quite low cost per bit of stored data. Removable storage at

the bottom of the hierarchy mainly includes digital versatile disk (DVD), compact disk (CD), and magneto-optical (MO) disk. DVD is a popular optical disk storage technology, and crystalline-amorphous phase change materials are commonly used for recordable DVD. Optical storage system offers a reliable and removable storage medium with excellent robustness and archival lifetime and with extremely low cost. New formats Blu-ray and HD-DVD, which have higher capacity than DVD, are available now. Modern types of solid-state memories such as static random access memory (SRAM) and a dynamic RAM (DRAM) sit at the top of the hierarchy due to their fast access and write times. The solid-state memories store a bit of data in either state of a flip-flop or as a charge in a capacitor, and the information stored is volatile at present. New types of non-volatile RAM, which will preserve data while powered down, are under development, since they will be able to eventually take a significant market share from either DRAM, SRAM, and will give another technological revolution in the information technology. Detail of the solid-state memories and the development of the non-volatile memories will be described in the following section.

1.2 Memory technologies

Semiconductor memory is an indispensable component of modern electronic systems. It is used in personal computers, cellular phones, digital cameras, smart-media, networks, automotive systems, and global positioning systems.

SRAM is the fastest type of semiconductor memory, with write/read times in the range of 1-10 ns. An SRAM cell, which stores one bit of information, is usually made of 6 transistors. As a result, SRAM is the most expensive and lowest density memory and is only used for the highest performance applications such as memory cache.

A Dynamic Random Access Memory (DRAM) cell consists of one transistor and one capacitor (1T1C) and provides very dense memory. It is superior to SRAM in many aspects except that the write speed is slower (50 ns). Its cell size is much smaller than that of SRAM and thus it is a low cost commodity memory device.

However, these memories are volatile and the data are stored only as long as electric power is supplied to refresh the capacitor charge in DRAM and to keep the transistors “ON” in SRAM.

The flash memory provides non-volatile semiconductor storage. Flash memory stores information in an array of floating-gate transistors, called “cells”. In traditional single-level cell devices, each cell stores only one bit of information. Some newer flash memory, known as multi-level cell devices, can store more than one bit per cell by controlling the amount of charge stored in its floating gate. However, flash memory exhibits some evident disadvantages: slow write access time in the μsec range and poor bit cyclability limited to 10^6 write events. Additionally, it requires a high voltage to program/erase the data [1].

None of the existing memory technologies satisfies all of the requirements simultaneously. A universal memory has to be developed to solve all or most of the memory problems. The universal memory should have a very high capacities, low power consumption and high data transfer rate and it would be non-volatile. Any new types of the memory with these specifications would face very hard challenges because it has to be superior to all the well established technologies. In recent years, there have been great advances in material developments, nanotechnology, and molecular electronics. A universal memory can benefit from and utilize these concepts.

1.3 Emerging memory technologies

Driven by the change of the market demand, a recent flurry of activity in the development of new memory technologies has emerged. Products based upon Magnetic Random Access Memory (MRAM), Ferroelectric RAM (FeRAM), Phase Change RAM (PCRAM), Conductive Bridging RAM (CBRAM), molecular memory, and single-electron memories, and so on are in various stages of development by many firms, and commercial release of some of these products is planned for the near future.

1.3.1 FeRAM

Ferroelectric random-access memory (FeRAM) is a type of nonvolatile random access memory combining both ROM and RAM advantages. FeRAM can achieve high-speed read/write operations comparable to that of dynamic RAM (DRAM), without losing data when the power is turned off (like ROM). Ferroelectric random access memory (FeRAM) uses a layer of ferroelectric material, typically lead zirconate titanate (PZT) shown in Fig.1.1 [2], as the dielectric layer in a storage capacitor. The basic storage element, a ferroelectric capacitor, is used in a DRAM-like configuration to take advantage of the capacitor's non-linear QV response that can be polarized into two different stable states, as shown in Fig.1.1, which are maintained when bias is removed. An electric polarization of PZT (shift up/down of Zn/Ti atom) remains after applying and removing an external electric field, from which a non-volatile property results [3]. FeRAM provides data retention for 10 years while eliminating reliability concerns, functional disadvantages and system design complexities of battery-backed up SRAM. FeRAM embedded in LSI circuits have been used in smart cards, radiofrequency identification (RFID) tags, and as a replacement for BBSRAM (batterybacked-up static RAM), which is used in various devices to protect data from an unexpected power

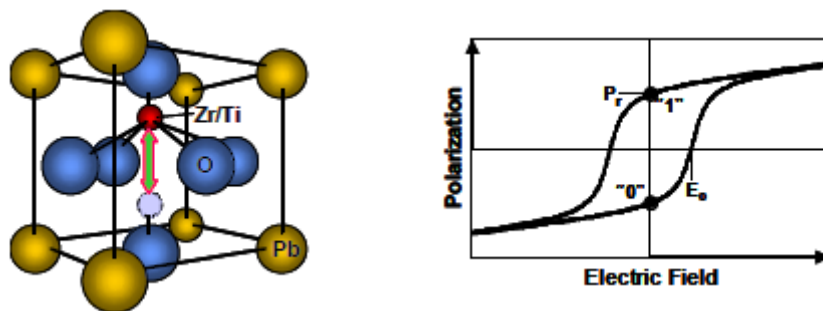


Fig. 1.1. Perovskite type crystal structure of PZT and hysteresis loop with two stable states at $E=0$.

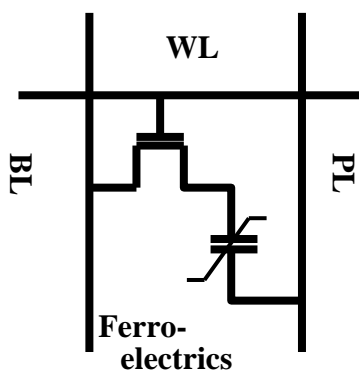


Fig. 1.2. Circuit diagram of 1T1C FeRAM cell.

failure, as well as in many other SoC (system on a chip) applications. FeRAM cells have been extensively developed to improve their density, speed, read/write endurance, and reliability. A memory cell, where one bit of data is stored, is composed of a cell-selection transistor and a capacitor for 1T1C (one transistor, one capacitor)-type FeRAM, as depicted in Fig.1.2 [4]. A major problem encountered is reducing the size of the memory cell without reliability degradation. The readout operation in a conventional FeRAM is destructive (i.e., reading the data destroys them), and thus there are limitations in the read/write cycles and the access time (the time required to read one bit of data). Recently, Masui *et al.* developed a 6T4C-type FeRAM with a nondestructive readout, unlimited read/write cycles, and an access time of less than 10 ns [5]. Because

of the six capacitors and four transistors, this type of FeRAM cell usually has high power consumption and is generally expensive. It is possible that the performance of FeRAM will be enhanced by the continuing improvements that are being made in the materials (including parameters such as switching charge, coercive field, fatigue, stability, leakage current, etc.), the processing steps (temperature control, uniformity, limiting damage due to processing, etc.), the device (scaling, improved processing steps, reliability, etc.), and the circuits (margin of operation, power consumption, access speed, reliability, etc.).

1.3.2 Phase change RAM (PCRAM)

In recent years, there has been a renewal of interest in phase-change random access memory (PCRAM) (or OUM) as a candidate for next-generation nonvolatile memory device because of many advantages such as nonvolatility, fast operation property, process simplicity, and possibility of multibit operation [6]. The use of phase-change chalcogenide alloy films to store data electrically was first reported in 1968 [7]. Particularly, chalcogenide alloys based on stoichiometric GeSbTe are the most popular due to their remarkable capability of providing fast kinetics of the phase change. The phase change memory concept is based on the reversible phase conversion between the amorphous and the crystalline state of a chalcogenide glass, which is accomplished by proper heating and cooling of the used phase change material. The aforementioned two physical states of matter differ in their resistivity with much better conduction in the crystalline phase of the chalcogenide than in the amorphous one. This is due to the reduced scattering of charge carriers in films with atomic long range order. The typical PCRAM cell is shown in Fig.1.3. Applying a very short electrical pulse (~10 ns) to the phase change material, results in the transition from the crystalline to the amorphous

state (RESET state). The melting causes the alloy to lose its crystalline structure and rapidly cooling it to below the glass transition temperature yields the amorphous phase. For effectively quenching the amorphous phase, a critical cooling rate exceeding the crystal nucleation rate must be achieved. Typical melting temperatures of commonly used chalcogenide glasses are about 600°C [6,7]. In order to write the crystalline state (SET state) into the cell a longer pulse (~100 ns) with a lower amplitude is applied, thereby heating the material over the critical crystallization temperature and leaving it in the low resistivity polycrystalline phase, as shown in Fig.1.4. The crystallization occurs below the melting temperature but above the glass-transition temperature (~200 °C), and at about 300 °C [8]. The difference in resistivity of the two states can be up to six orders of magnitude [8], however in realistic device applications the ratio is generally only about 1-2 orders of magnitude [6]. PCRAM give great opportunities in various applications. Fast random access with non-volatility can simplify the system architecture, thereby resulting in enhancing system performance comparing with Flash memory. Virtually unlimited endurance of PCRAM over 10^{12} cycles generates many opportunities over Flash memory where reliability of memory is essential. Due to the simple process for PCRAM resistor module, it can be readily implemented in the logic circuit with two or three additional photolithography steps. Thus, it has great opportunities for embedded memory or system on chip (SOC) application. There are several technical challenges in PCRAM in spite of its many advantages. The major obstacle of PCRAM is large programming current, which is limited by Reset. The programming current should be reduced in order to obtain the low cost, high density, low power consumption, and good reliability.

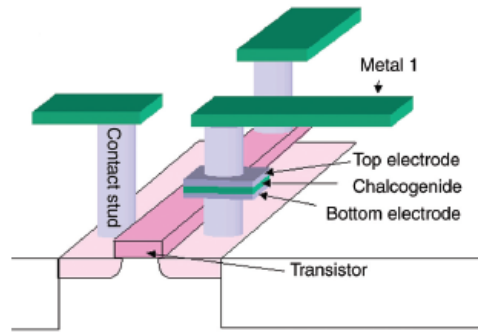


Fig. 1.3. Typical PCRAM cell [9].

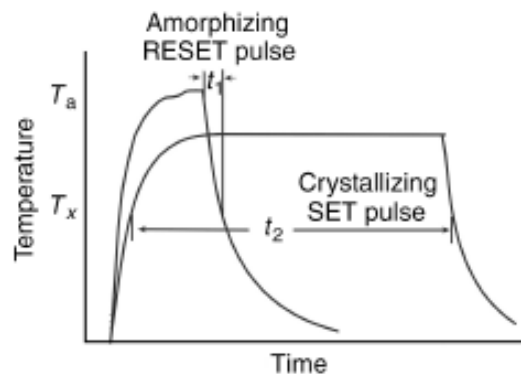


Fig.1.4. Schematic temperature–time relationship during programming in a phase change rewriteable memory device. T_a and T_x are the amorphization and crystallization temperatures, respectively [9].

1.3.3 Conductive Bridge RAM (CBRAM)

The CBRAM memory effect is based on a polarity-dependent, resistive switching at a low write threshold voltage V_{th} of ~ 250 mV with typically ~ 2 μ A write current and an erase voltage threshold of ~ 80 mV [10]. Key attributes are low voltage and current operations, excellent scalability, and a simple fabrication sequence. In Fig.1.5, the CBRAM switching mechanism is depicted. The ON-state of a CBRAM is achieved by applying a positive bias larger than the threshold voltage V_{th} at the oxidizable anode resulting in redox reactions driving Ag ions in the chalcogenide glass. This leads to the

formation of metal rich clusters, which form a conductive bridge between both electrodes. The device can be switched back to the OFF state by applying an opposite voltage. In this case, the metal ions are removed, which in turn erases the conductive bridge.

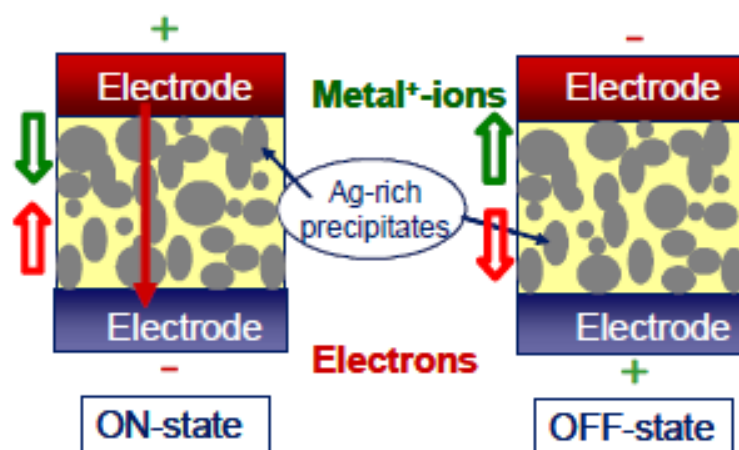


Fig. 1.5. Schematic illustration of the CBRAM switching mechanism: ON state: Redox reaction drives Ag ions in chalcogenide glass, resulting in a conductive bridge; OFF state: Size and number of Ag-rich clusters is reduced breaking the conductive bridge [11].

1.3.4 Molecular Memory

In this type of memories, a single device consists of a single layer of molecules or a single molecule that exhibits bi-stable resistance switching. These memory elements make use of physical effects which occur in single molecule involving quantum mechanical effects. The switching is based on several kinds which can cooperate to achieve switching. Some of these mechanisms are [12]:

- a. Reduction-oxidation (redox) process where a neutral molecule can be changed to an ionized acceptor/donor group.
- b. Configuration change through a reversible rearrangement reaction.
- c. Conformation change where there are two stable conformations at room temperature.

In Rose Bengal for example, redox and conformational change of the molecules cause the conjugation modification, and as a result, the conductance of the molecules is changed. Another example is the catenanes, which are molecules consisting of two interlocked rings. The interaction of different redox states makes it possible to rotate one ring within the other. The state of rotation can correspond to binary values.

1.3.5 Single/Few electron

Single/few electron memory is characterized by the confinement of electrons in a quantum dot by the “Coulomb blockade” effect. In single-electron devices, electron movement (e.g., the addition or subtraction of an electron to a small 3-D “island,” or quantum dot) is controlled with integer electron precision. Injection of each electron on to the quantum dot occurs through a tunneling barrier and is controlled by a separate gate electrode(s) via the Coulomb blockade effect. In such quantum dots, electrons are confined electrostatically in all three dimensions, forming a small island of electrons that is bounded on all sides by potential walls (Fig. 1.6). The electron island can accommodate only an integer number of electrons, and these electrons can occupy only certain discrete energy states. Connected through tunneling barriers, the conductance of the dot exhibits strong oscillations as the voltage of a gate electrode is varied. Each successive conductance maximum corresponds to the discrete addition of a single electron to the dot. A basic component of single electron memory is the single-electron transistor (SET). The SET is composed of a quantum dot connected to an electron source and to a separate electron sink through tunnel junctions with electron injection controlled by a gate electrode. Several concepts of single-electron memory have been experimentally demonstrated, including a SET/FET hybrid. Two major concerns for all single electron memories reported so far are designing for room-temperature operation

and the management of the impact of background charges. Several manufacturers have reported successes in treating these issues.

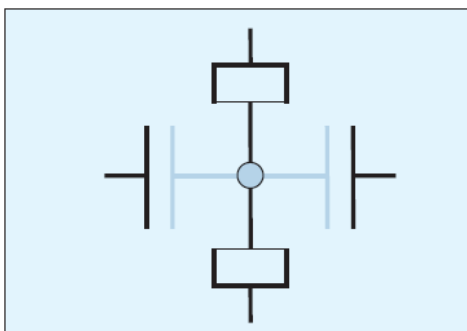


Fig. 1.6. Single/few electron memory cell cartoon [13].

1.3.6 MEMS memory

MEMS memory is a thermomechanical scanning-probe-based data-storage, uses an array of AFM cantilevers that can read and write in parallel, thereby dramatically increasing the throughput to the point where it can compete with some forms of electronic memory. Additionally, millipede's physical medium stores a bit in a very small area, leading to densities even higher than current hard disc drives. Each cantilever performs write/read/erase operations within an individual storage field. Write/read operations depend on a mechanical x/y scanning of either the entire cantilever array chip or the storage medium. Figures 1.7 illustrates this MEMS memory design [14]. To accomplish a read, the probe tip is heated to around 300 °C and moved in proximity to the polymer [15]. If the probe is located over a indentation the cantilever will push it into the hole, increasing the surface area in contact with the sled, and in turn increasing the cooling as heat leaks into the polymer from the probe. In the case where there is no pit at that location, only the very tip of the probe remains in contact with the

polymer, and the heat leaks away more slowly. The electrical resistance of the probe is a function of its temperature, rising with increasing temperature. Thus, when the probe drops into indentations and cools, this registers as a drop in resistance. A low resistance will be translated to a “1” bit, or a “0” bit otherwise. While reading an entire storage field, the tip is dragged over the entire surface and the resistance changes are constantly monitored. Thermomechanical writing is achieved by applying a local force through the cantilever/tip to the polymer layer and simultaneously heated to a temperature above the glass transition temperature of the polymer, which is generally acrylic glass. In this case the transition temperature is around 400 °C. To write a "1", the polymer in proximity to the tip is softened, and then the tip is gently touched to it, causing a indentation. Erasing

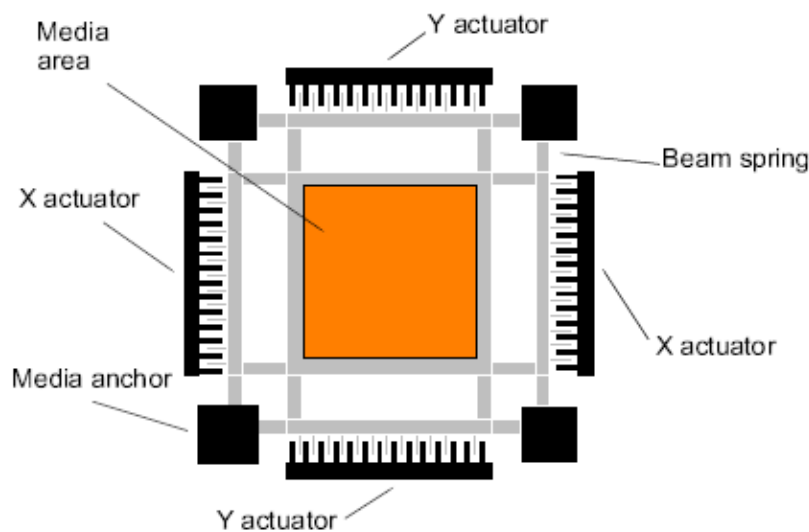


Fig. 1.7. Components of a MEMS-based storage device. The media sled is suspended above an array of probe tips. The sled moves small distances along the X and Y axes, allowing the stationary tips to address the media [14].

can be selective or non selective, which means that individual bits or the whole storage fields can be erased. Selective erasing is achieved by using the pile-up effect. Non selective erasing is accomplished by the thermal reflow of the storage fields by heating

the medium to about 150 °C for a few seconds. This erasing process does not allow bit level erasing: it will erase large storage areas. However, in most applications single-bit erasing is not required anyway, because files or records are usually erased as a whole.

1.4 MRAM--spintronic devices

Spintronics offers opportunities for a new generation of devices combining standard microelectronics with spin-dependent effects that arise from the interaction between spin of the carrier and the magnetic properties of the material [16]. Basic research in spintronics is moving rapidly to smaller structures and novel materials, as well as focusing on new physical phenomena. This research will focus on a novel non-volatile magnetic random access memory (MRAM).

Magnetic random access memories (MRAMs) are the technique based on the integration of Si CMOS with magnetic memory element. One of the most important characteristics of MRAM is the fact that it uses the spin of an electron, rather than the charge. MRAM has unlimited read and write endurance, and could enable truly non-volatile RAM with both the high speed of today's Static RAM and the high density of DRAM. O'Handley actually credits the first conception of MRAM to Schwee in the early 1970s [17,18] but the concept gained little notoriety [19]. The interest in MRAM started some 20 years ago with a crosstie RAM concept [20], followed by the use of the anisotropic magnetoresistance (AMR) materials [21], later replaced by higher sensitivity giant magnetoresistance (GMR) devices [22]. Not only is the signal strength larger, but the characteristics of the physical phenomenon itself are well suited for MRAM, which uses magnetic-moment direction as information storage and the resultant MR difference for sensing. A submicrometer critical dimension of the MRAM cell is essential for its competitiveness in the general memory market. A number of different memory-storage

methods using different types of GMR films have been explored for application in high-density MRAM [22,23]. Since the sheet resistance of the GMR film is small compared to that of a complementary metal-oxide semiconductor (CMOS) transistor, a number of GMR MRAM memory cells must be connected in series with a CMOS transistor, so that total resistance from the memory cells is much larger than that from the transistor. Although good from a design point of view, this scheme effectively decreases the usable signal, making it difficult to design a high-speed memory. Large (perpendicular) resistance of magnetic tunnel junctions (MTJs) allows the high packing density of a cross-point architecture for MRAM [24~26]. Spin dependent tunnel junctions showing significant magnetoresistance at room temperature using amorphous AlO_x barriers. Recent studies using crystalline MgO barriers have shown that it is possible to increase the available magnetoresistive signal to more than 200% resistance change at room temperature [27]. Such a MTJ material is quickly finding applications in MRAM and magnetic-field sensing [28,29]. Major advantages of the MTJ material include a larger signal, and its tunable product of resistance and area (RA), depending on barrier thickness and degree of oxidation. This kind of high-density architecture is suitable for fast-speed, low-power memory applications.

1.4.1 Conventional MRAM

In its most simple implementation, an MRAM cell is composed of a magnetic tunnel junction (MTJ) connected to a selection transistor [30], as shown in Fig. 1.8. The resistance of the memory bit is either low or high depending on the magnetization orientation of the free layer relative to the pinned reference layer, parallel or antiparallel. To read one bit, a particular cell is (typically) selected by powering an associated transistor, which switches current from a supply line through the cell to ground. The

value of the junction resistance is then compared to a reference resistance half-way between the high and low resistance values. In conventional approaches, the direction of the storage layer in MTJ is set in plane by orthogonal magnetic fields through shape anisotropy. The bit writing process proposed for MRAM relied on two orthogonal magnetic fields, which are generated by a current flow in bit and word lines, being applied to a cell, as depicted in Fig. 1.8. This switching approach is based on a coherent magnetization reversal in single domain particles. Energy minimization can be used to find that the easy axis field H_e required to reverse the magnetization is reduced by applying simultaneously a second perpendicular field along the hard axis H_h . The solution yields an astroid equation:

$$H_h^{2/3} + H_e^{2/3} \geq \left[\frac{2K}{M_s} \right]^{2/3} \quad (1.1)$$

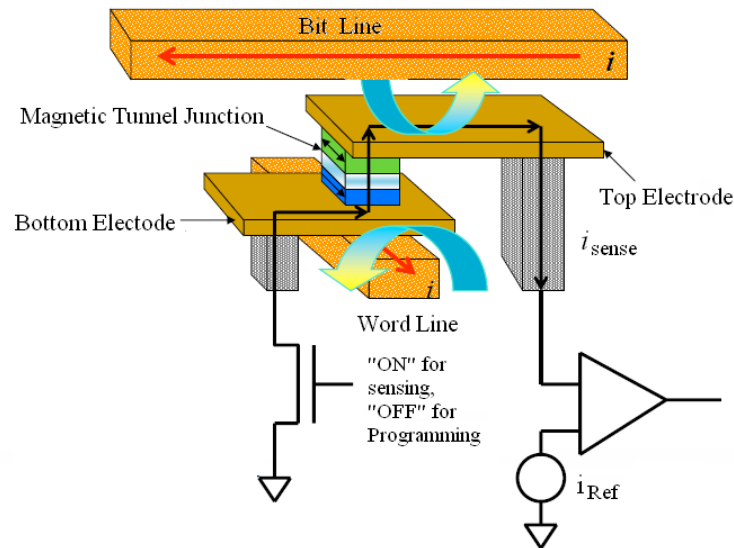


Fig. 1.8. Conventional architecture used in the first MRAM generation containing a MTJ cell.

where K is the effective anisotropy, accounting for crystalline and shape anisotropies, and M_s the saturation magnetization. Switching occurs for any combination of fields for which the resulting field vector lies outside the astroid. This allows the selective switching of one bit in the matrix by choosing easy and hard axis fields inside the astroid. This coherent reversal can be achieved in a few nanoseconds (3–7 ns) [27,31,32]. The magnetization direction of the reference pinned layer is fixed by the direct exchange coupling with an antiferromagnetic material.

1.4.2 The limitation of conventional MRAM

One of the major challenges is the temperature compatibility of spin-electronics with CMOS technology. If MTJ films are used in the back-end of a CMOS process, which seems to be the established route for MRAMs, then they need to survive a 400 °C anneal. The anneal is used to cure plasma induced damage during back-end processing [33]. Discussions of temperature compatibility are beyond the scope of this work. Switching uniformity, thermal stability and power consumption will be discussed as follow when the scalability of MRAM to smaller bit sizes.

1.4.2.1 Selectivity and switching field distribution

The scalability of MRAM to deep submicron bit sizes is faced with challenges. In a conventional MRAM design, MTJ cells are patterned and information is stored in free layers through their shape anisotropies. Therefore, at small dimensions, the magnitude of the switching field is critically governed by the precise shape of the single bit. Upon decreasing the size and the bit aspect ratio, the width of the switching field distribution is enlarged. This is due to deviations from the nominal bit geometry or edge roughness that appear during the nanofabrication. Finding a set of fields which can be used to program all cells becomes difficult or unusable due to the very narrow operating

window [24]. Ultimately the switching field depends on the dimensional control of the lithography and patterning process, which becomes less precise as the bit dimensions become closer to the minimum feature size. This becomes an important scaling limitation as the field write margin is reduced by the larger switching field distribution. To overcome the selectivity issue the Stoner–Wohlfarth (SW) writing approach was replaced by a ‘toggle’ switching proposed by Savtchenko at Freescale/Motorola [34]. The operating region in toggle MRAM writing is considerably larger than the SW operating window. The toggle switching approach solves the bit selectivity issue, but the scalability of the cell size to deep sub-micron dimensions still remains. For sizes below 100 nm the problems of long term data retention and high power consumption still subsist in toggle switching.

1.4.2.2 Thermal stability and power consumption

The recording of information in free layer of MTJ is similar in principle to traditional magnetic storage. To realize the MRAM device with bit densities of Gbit/cm² order, the size of the magnetic cell and the separation between adjacent cells must be an order of 0.1 μm or less. As the magnetic cell is downsized in low sub-μm scale, the amplitude of the energy barrier E_b for the magnetization switching becomes small, resulting in the degradation of the thermal stability due to an entropy effect [35,36]. Therefore, to guarantee the bit information for long time periods it is necessary to take into superparamagnetic limit. The energy barrier between stable configurations is proportional to the volume of the magnetic material, to the shape or uniaxial anisotropies. As the bit size is reduced, this energy barrier may become comparable to the thermal energy and unwanted thermally activated switching can occur, leading to data loss. The commonly accepted requirement for 10 year stability is $E_b \geq 65 k_B T$, with

$k_B T$ being the thermal energy. This creates a necessary compromise between write power consumption and bit stability. The magnetic volume reduction associated with the scaling must be compensated by higher anisotropy, leading to higher switching fields and an increase in write power consumption.

1.4.3 Thermally assisted MRAM

Recently a new write approach, called thermally assisted switching (TA-MRAM), was proposed to improve the thermal stability, write selectivity and power consumption in MRAM applications [37~39]. Heating had already been previously proposed to write the bit state of tunnel junctions by flowing a current in the write lines and heating the magnetic layers in the MRAM cell above their magnetic ordering temperature, greatly reducing the write fields [40,41]. So far, there are two methods to heat the cell. Initially, Daughton *et al.* suggested that two orthogonal current lines are used to heat the cell and generate the write field [41]. The coincident heating from two lines can be used to select one cell for thermal writing. The main disadvantage of such write architectures is that the heating is indirect and relies on heat diffusion, meaning high power consumption and long write cycles. To improve the Joule heating and write speed, for conventional high resistance junctions ($K\Omega \times \mu m^2$), to heat directly with the current flow through the MTJ was purposed, after turning the selection transistor ON during the write procedure. Since the heat is generated locally inside the junction this is a more efficient solution than the indirect diffusive heating. Conventionally, there are also two possible designs method in the thermal dependence of the magnetic properties of the MRAM cell varies^[42]. A first design proposed by Daughton and co-workers uses a low Curie point ferromagnetic cell with shape anisotropy. The bit can be relatively thick for thermal stability at low temperatures, and can be written with relatively small fields as the cell is

cooled through the Curie point. The write current raises the temperature of the heating element slightly above the Curie point of the storage layer. In a second design the MTJ stack of the cell is slightly modified: the storage layer comprises a ferromagnetic layer exchange biased by a low blocking temperature (T_B) antiferromagnetic material. When the storage layer temperature exceeds T_B , the ferromagnetic layer is freed and can be reversed under the application of a small magnetic field provided by a single digit line. The magnetic field is maintained beyond the heating voltage pulse in order to cool the MTJ under magnetic field and ensure a correct pinning of the storage layer. The reference and the storage layer must be exchange biased at different blocking temperatures.

1.5 Comments on emerging memories

Emerging memories which possess ideal properties, i.e, non-volatility, fast random access, unlimited endurance, can revamp memory management in systems, from the complicated memory solution of the systems which is due to the multiple usage of many different types of memories at the same time and in the same system, to simple memory solution where only single type of new memory may be of necessity. Fast random access with non-volatility of emerging memories can eliminate the separation between the data storage oriented memories like DRAM and code storage dedicated memory like NOR Flash. As a result, we can realize both data and code-storage memory function with a single new memory. Moreover, the capability of bit by bit data alteration with randomness of new types of memories can greatly simplify the data changing process, thereby resulting in enhancing system performance. Many merits of the emerging memories lead to the conclusion that the new types of memories having excellent functional properties will have great potential to displace the existing memories and

create the new types of applications such as instant-on PC, fast data storage, unified memory and so on. In these emerging memories, FeRAM, PCRAM(OUM)and MRAM are more mature and the most widely pursued non-volatile memory. The most important characteristics of conventional memories and three types representative emerging memory are summarized in Table 1.1 [42].

They can be used as universal memories, based on their nonvolatility, performance and high endurance. In hand held appliances like cell phones today, a combination of Flash (to store the data) and SRAM (to support the processor) is used. A universal memory is able to provide both functions in one IC, reducing the board space and simplifying the system architecture. With universal memories one can also build instant on computers.

Table 1.1. Comparison of memory technologies.

Feature	DRAM	SRAM (6T)	FLASH	OUM	MRAM	FeRAM
Cell size [F^2]	8–12	50–80	4–11	5–8	6–20	4–16
Non-volatile	No	No	Yes	Yes	Yes	Yes
Endurance write/read	∞/∞	∞/∞	$10^6/\infty$	$>10^{12}/\infty$	$>10^{15}/\infty$	$>10^{12}/>10^{12}$
Non-destructive read	No	Partial	Yes	Yes	Yes	No
Direct overwrite	Yes	Yes	No	Yes	Yes	Yes
Signal margin	100–200 mV	100–200 mV	Δ current	$10\text{--}100 \times R$	$60\text{--}200\% R$	100–200 mV
Write/read	50 ns/50 ns	8 ns/8 ns	200 μ s/60 ns	10 ns/20 ns	30 ns/30 ns	80 ns/80 ns
Erase	50 ns	8 ns	1–100 ms (block)	50 ns	30 ns	80 ns
Transistor performance	Low	High	High voltage (HV)	High	High	High
Scalability limits	Capacitor	6 Transistors	Tunnel oxide/HV	Litho.	Current density	Capacitor

1.6 MTJ

A magnetic tunnel junction (MTJ) is defined as a multilayer consists of two ferromagnetic layers separated by a thin insulating barrier layer ($\sim 20 \text{ \AA}$). Application of a voltage bias at the electrodes leads to a tunneling current whose magnitude depends on the relative orientation of the magnetizations of the ferromagnetic layers.

Conventionally, the resistance of MTJ, with ferromagnetic electrodes (e.g. Co, Fe, and Ni) is higher when the magnetizations of the two electrodes are antiparallel as compared to parallel alignment.

The first successful tunnel junction was prepared by Julliere in 1975 [43]. He observed a 14% junction magnetoresistance ratio for Fe/Ge/Co tunnel junctions at 4.2 K and in zero voltage bias. MR ratio decreased monotonically as voltage bias increased. Later, in the 1980s, Maekawa *et al.* [44] showed this effect in Ni-NiO-Co junctions. They were able to observe only 2 % of TMR at liquid helium temperature. Large magnetoresistance (18%) at room temperature for magnetic tunnel junctions was prepared using amorphous Al₂O₃ barriers by two different groups (Miyazaki [45] and Moodera [46]) in 1995. Since then, significant improvements have been made to both the understanding and fabrication of the MTJ. With this, the TMR values with Al₂O₃ as barrier were increased more than 40 % [47]. The research in Al₂O₃ based MTJs focused on changes in the material used for free layer electrode have improved TMR values to 60 % [48], especially with CoFeB electrodes. The latest known TMR with Al₂O₃ barrier with CoFeB as electrode is 70 % [49]. Interest in MgO as a potential tunnel barrier started with the theoretical predictions independently made in 2001 [50,51] of getting very high TMR values with epitaxial Fe/MgO/Fe. Since then the investigation into this junction gave very high values of TMR at room temperature. Yuasa *et al.* observed the TMR of 180 % in 2004 for Fe-MgO-Fe junctions [52]. The most promising electrode for MgO based MTJ devices has been found to be CoFeB. The values of TMR observed for CoFeB/MgO/CoFeB based MTJ at room temperature has shown an increasing trend with 230 % of TMR achieved by Djayaprawira *et al.* in 2005 [53], 361% by Ikeda *et al.* [54,55] and in 2006, 472 % [56]. At room temperature

(RT) a 500% signal is achieved by Tohoku-Hitachi in 2007. At 5K temperature that value raises to 1010% [57]. This is the highest TMR public reported so far.

The first explanation for the tunneling magnetoresistance effect was given using a simple but useful model by Julliere [43]. Julliere proposed that the TMR can be written as

$$TMR = \frac{\Delta R}{R_{\min}} = \frac{2P_1P_2}{1 - P_1P_2} \quad (1.2)$$

with $P_{1,2}$ being the spin polarization of the electrodes defined as:

$$P_{1,2} = \frac{|M_{\uparrow}|^2 N_{\uparrow} - |M_{\downarrow}|^2 N_{\downarrow}}{|M_{\uparrow}|^2 N_{\uparrow} + |M_{\downarrow}|^2 N_{\downarrow}} \quad (1.3)$$

Here the tunneling matrix elements $|M_{\uparrow,\downarrow}|^2$ denote tunneling probabilities for tunneling of spin up and spin down electrons respectively and $N_{\uparrow,\downarrow}$ the corresponding density of states at the Fermi energy. The spin polarization $P_{1,2}$ can be measured directly using superconducting tunneling spectroscopy and is then referred to as tunneling spin polarization. According to Julliere's model, P_1 and P_2 is directly related to TMR value, in other words, the higher spin polarization of the electrode leads to the larger TMR. Large TMR ratio is an important criterion for industrial application due to the increase of signal to noise ratio (SNR) and output voltage. Since Julliere's model is based on some ideal assumptions, the TMR values calculated by this model usually are an upper limit for the measured ones at low temperatures and zero applied bias. Given the shortcomings of Julliere's model, other models were proposed [58~60].

The TMR is highly dependent on temperature and applied bias. The TMR generally decreases monotonically with applied voltage bias for bias voltages up to ~1V but the voltage dependence can be asymmetric with respect to zero bias [61]. Moreover, The zero bias anomaly has been observed for tunnel junctions with one or

more ferromagnetic electrode [62]. Clear implications may be inferred from the theoretical treatment of the MR dependence on voltage bias: the barrier must be high quality and the barrier/ferromagnet interface clean and abrupt. Increasing the temperature generally diminishes the TMR, most likely due to a reduction of the magnetic moment at the electrode interfaces by thermally excited spin waves [63].

The tunneling barrier (including its interfaces with the electrodes) is the most crucial part in any magnetic tunnel junction. For a proper operation of the tunnel junction, the following issues must be taken care of: The barrier must be homogeneous, without pinholes (paths of higher conduction) or impurities that will cause large parasitic, unpolarized currents parallel to the polarized tunnel current, decreasing the TMR. The barrier must be smooth. Some roughness of the barrier thickness can cause inhomogeneous currents through the layer that can lead to very local heating and breakdown of the barrier, creating shorts. Roughness of the barrier can cause a magnetic coupling between the two electrodes, which results in the situation that the layers do not switch independently and an anti-parallel state cannot be achieved anymore. Obtaining a thinner tunnel barrier without losing MR is one of the key factors to achieving low RA. As bit sizes are reduced, MRAM may require material with lower RA. In addition, use in hard-disk read heads would require a much lower resistance for the first generation of product.

1.7 Motivation for this thesis

In this thesis, we suggest the thermally assisted MTJ composed of RE-TM alloys for future ultra high density MRAM, since the perpendicular magnetized MTJ cell exhibits uniform magnetization throughout the cell even though the cell has small

dimensions and a low aspect ratio [64]. The layer structure of this type MRAM is shown in Fig. 1.9. The TbFe film is an ideal candidate for the storage layer in thermally assisted MRAM, because they have excellent properties suitable for thermomagnetic writing such as high anisotropy at room temperature, low Curie temperature and strong temperature dependence of the coercivity. High Curie temperature is necessary for a pinned layer, and is easily achieved by the addition of Co into TbFe alloys. We will discuss in detail their magnetic and magnetoresistance properties in chapter 3. The TbFe(Co) alloys are used as ferromagnetic layers, and it is expected that the spin polarization of the TbFe(Co) is much lower than that of Fe or Co. In addition, the rare earth element is quite easily oxidized. Therefore, to increase the MR ratio of MTJs with perpendicularly magnetized RE-TM amorphous alloy films, high spin-polarized FeCo is suggest to be inserted between the RE-TM and oxide layers.

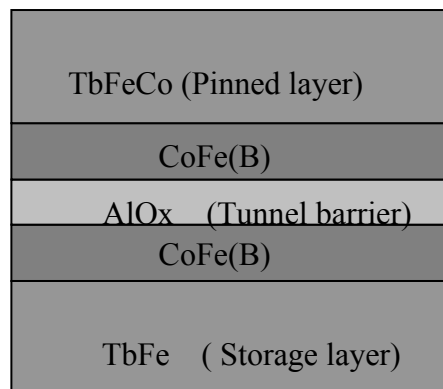


Fig. 1.9. Layered structure of the cartoon MTJ composed of RE-TM alloys for a thermally assisted MRAM.

The thermally assisted MRAM using RE-TM alloys offers many advantages in their write scheme. First, the bit selectivity is quite improved since only the heated

junction can be written in a small external field. Second, the RE-TM storage layer has good magnetic properties for the thermomagnetic writing, e.g., (i) high anisotropy at room temperature which allows thermally stable cells even for small feature sizes (ii) high coercivity by using near compensation composition RE-TM alloys (the low magnetization of the storage layer guarantees a high protection against magnetic erasure), (iii) strong temperature dependence of the coercivity (switching field). Finally, the Curie point of the storage and pinned layers can be easily tuned according to the requirement. Therefore, it is possible to reduce the heating power to switch the storage layer using low Curie point storage layer, while ensuring the stability of the pinned layer with high Curie point pinned (reference) layer.

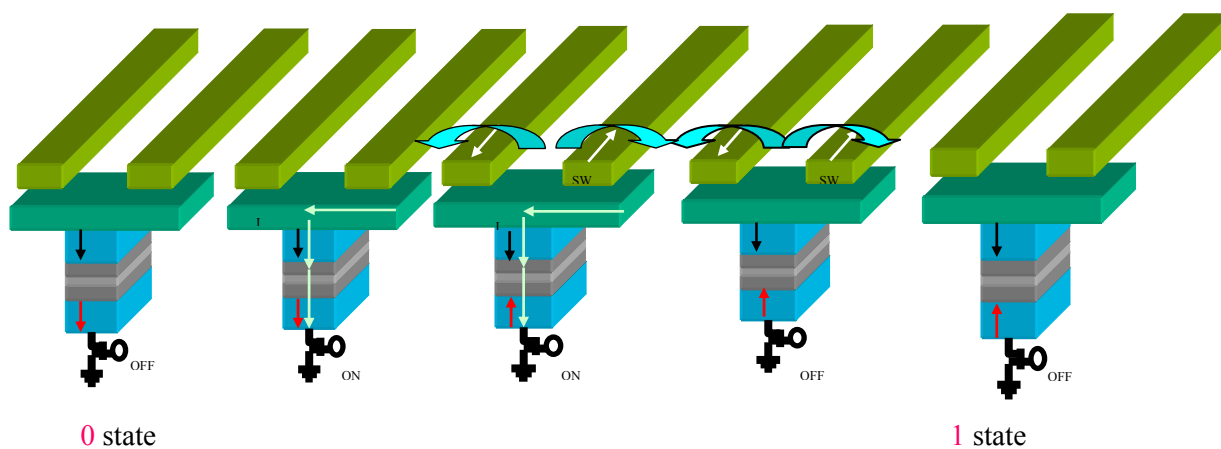


Fig. 1.10. The writing steps of the thermally assisted switching of the perpendicular magnetized MTJ.

The writing sequence of Curie point writing on the perpendicular MRAM (using ferromagnetic RE-TM) is similar to that of blocking temperature writing as discussed in 1.4.3 [27]. The initial orientation of the storage layer with high coercivity (uniaxial anisotropy) (leftmost drawing in Fig. 1.10) sets the bit in a low resistance state ‘0’. The

reversal of the storage layer is achieved by heating the TbFe storage layer to around above its Curie temperature with a current pulse and applying simultaneously a relatively small magnetic field H_{sw} (middle of Fig. 1.10). The field is applied in a direction that opposes to previous magnetization direction of the storage layers. The current pulse for heating is terminated and the system is cooled in a magnetic field. The result is a reversal of the storage layer and a bit state changes to a high resistance '1' shown in the rightmost drawing of Fig. 1.10.

In this thesis, I have focused on the studying of the required heating power for thermomagnetic writing of the storage layer. I have designed the experiment method to estimate the required heating power, and investigated that the dependence of the required heating power/energy density on the patterned size, pulse duration and writing field.

1.8 Organization of this thesis

The practical techniques of the film deposition, lithography and processing are considered in chapter 2. The properties of RE-TM alloys and the magnetoresistance of the MTJ structure using RE-TM alloys are discussed in chapter 3. MFM study of thermomagnetic writing of the patterned TbFe-films is introduced in chapter 4, dynamic heating of the patterned TbFe films is investigated in chapter 5, and conclusion is given in chapter 6.

References

- [1] Semiconductor Flash Memory Scaling, Min She, Ph.D Dissertation, University of California, Berkeley, 2003.
- [2] G. Muller, N. Nagel, C. U. Pinnow, and T. Rohr, Proceedings of the 29th European Conference on Solid-State Circuits, 2003, pp.37.

- [3] C. A. Pazde Araujo, L. D. McMillan, B. M. Melnick, J. D. Cuchiario, and J. F. Scott, *Ferroelectrics*, **104** (1990) 241.
- [4] Y. Arimoto and H. Ishiwara, *MRS Bulletin*, **29** (2004) 823.
- [5] S. Masui, W. Yokozeki, M. Oura, T. Ninomiya, K. Mukaida, Y. Takayama, and T. Teramoto, *Proc. Conf. IEEE Custom Integrated Circuits*, 2003, p. 403.
- [6] R. Neale, *Electron. Eng.*, **73** (2001) 67.
- [7] S. R. Ovshinsky, *Phys. Rev. Lett.*, **21** (1968)1450.
- [8] G. Wicker, *SPIE Conference on Electronics and Structures for MEMS*, **3891** (1999) 2.
- [9] S. Hudgens and B. Johnson, *MRS Bulletin*, **29** (2004) 829.
- [10] G. Muller, T. Happ, M. Kund, G. Y. Lee; N. Nagel, R. Sezi, *Electron Devices Meeting, 2004. IEDM Technical Digest. IEEE International*, 2004, pp. 567.
- [11] M. Kund, G. Beitel, C. U. Pinnow, T. Rohr, J. Schumann, R. Symanczyk, K. Ufert, G. Muller, *Electron Devices Meeting, 2005. IEDM Technical Digest. IEEE International*, 2005, pp.754.
- [12] Design and analysis of future memories based on switchable resistive elements, Jakob Mustafa, Ph.D thesis, RWTH Aachen University, Germany, 2006.
- [13] J.E. Brewer, V.V. Zhirnov, J.A. Hutchby, *Circuits and Devices Magazine, IEEE*, **21** (2005) 13.
- [14] Using MEMS-based storage devices in computer systems, Steven W. Schlosser, Ph.D Dissertation, Carnegie Mellon University, 2004.
- [15] http://en.wikipedia.org/wiki/IBM_Millipede.
- [16] S. A. Wolf, D. D. Awschalom, R. A. Buhrmann, J. M. Daughton, S. von Molnar, M. L. Roukes, A. Y. Chtchelkanova, and D. M. Treger, *Science*, **294** (2001)1488.
- [17] R. C. O' Handley, *Modern Magnetic Materials: Principles and Applications*, 1st ed. (Wiley-Interscience, New York, 2000).
- [18] L. J. Schwee, *IEEE T. Magn.* **8** (1972) 405.
- [19] Investigation of spintronic materials systems: deposition and characterization, Neal C. Oldham, Ph.D Dissertation, California Institute of Technology, 2004.
- [20] L. J. Schwee, P. E. Hunter, K. A. Restorff, and M. T. Shephard, *J. Appl. Phys.*, **53** (1982) 2762.
- [21] A. Pohm, J. Daughton, C. Comstock, H. Yoo, and J. Hur, *IEEE Trans. Magn.*, **23** (1987) 2575.
- [22] S. Tehrani, E. Chen, M. Durlam, M. DeHerrera, J. M. Slaughter, J. Shi, and G. Kerszykowski, *J. Appl. Phys.*, **85** (1999) 5822.
- [23] E. Y. Chen, S. Tehrani, T. Zhu, M. Durlam, and H. Goronkin, *J. Appl. Phys.*, **81** (1997) 3992.

- [24] J. Daughton and Y. Chen, *IEEE Trans. Magn.*, **29** (1993) 2705.
- [25] P. K. Najj, M. Durlam, S. Tehrani, J. Calder, and M. F. DeHerrera, 2001 ISSCC Digest of Technical Papers, pp. 122.
- [26] R. Scheuerlein, 2000 ISSCC Digest of Technical Papers, pp. 128.
- [27] I L Prejbeanu, M Kerekes, R C Sousa, H Sibuet, O Redon, B Dieny, and J P Nozières, *J. Phys.: Condens. Matter*, **19** (2007) 165218.
- [28] S.S.P. Parkin, K.P. Roche, M. G.. Samant, P. M. Rice, R. B. Beyers, R. E. Scheuerlein, E. J. O'Sullivan, S. L. Brown, J. Bucchigano, D. W. Abraham, Y. Lu, M. Rooks, P. L. Trouilloud, R. A. Wanner, and W. J. Gallagher, *J. Appl. Phys.*, **85** (1999) 3741.
- [29] S. Tehrani, J. M. Slaughter, E. Chen, M. Durlam, J. Shi, and M. D. herrera, *IEEE Trans. Mag.*, **35** (1999) 2814.
- [30] M. Durlam, S. Tehrani, J. Calder, M. F. DeHerrera, and P. K. Najj, 2000 ISSCC Digest of Technical Papers, pp. 130.
- [31] R. H. Koch, J. G. Deak, D. W. Abraham, P. L. Trouilloud, R. A. Altman, Y. Lu, W. J. G. lagher, R. E. Scheuerlein, K. P. Roche, and S. S. P. Parkin, *Phys. Rev. Lett.*, **81** (1998) 4512.
- [32] T. Yamamoto, H. Kano, Y. Higo, K. Ohba, T. Mizuguchi, M. Hosomi, K. Bessho, M. Hashimoto, H. Ohmori, T. Sone, W. Otsuka, N. Okazaki, M. Motoyoshi, H. Nagao, and T. Sagara, *J. Appl. Phys.*, **97** (2005) 10P503
- [33] H. Boeve, C. Bruynseraede, J. Das, K. Dessenin, G. Borghs, J. De Boeck, R.C. Sousa , L.V. Melo, and P. Freitas, *IEEE Trans Magn.*, **35**(1999) 2820.
- [34] L. Savtchenko, B. N. Engel, N. D. Rizzo, M. DeHerrera, and J. Janesky, 2003 US Patent Specification 6545906 B1.
- [35] W. F. Brown, *Phys. Rev.*, **130** (1963) 1677.
- [36] Y. Nozakia and K. Matsuyama, *J. Appl. Phys.*, **93** (2003) 7295.
- [37] I. L. Prejbeanu, W. Kula, K. Ounadjela, R. C. Sousa, O. Redon, B. Dieny, and J. P. Nozieres, *IEEE. Trans. Magn.*, **40** (2004) 2625.
- [38] J. Wang and P. P. Freitas, *Appl. Phys. Lett.*, **84** (2004) 945.
- [39] R. C. Sousa, I. L. Prejbeanu, D. Stanescu, B. Rodmacq, O. Redon, B. Dieny, J. Wang, and P. P. Freitas, *J. Appl. Phys.*, **95** (2004) 6783.
- [40] R. S. Beech, J. A. Anderson, A. V. Pohm, and J. M. Daughton, *J. Appl. Phys.*, **87** (2000) 6403.
- [41] J. M. Daughton and A. V. Pohm, *J. Appl. Phys.*, **93** (2003) 7304.
- [42] R.C. Sousa, I.L. Prejbeanu, *C. R. Physique*, **6** (2005) 1013.
- [43] M. Julliere, *Phys. Lett.*, **54 A** (1975) 225.
- [44] S. Maekawa and U. Gafvert, *IEEE Trans. Magn.*, **18** (1982) 707,

- [45] T. Miyazaki and N. Tezuka, *J. Magn. Magn. Mater.*, **139** (1995) L231.
- [46] J. S. Moodera, *Phys. Rev. Lett.*, **74** (1995) 3273.
- [47] S. S. P. Parkin, K. P. Roche, M. G. Samant, P. M. Rice, R. B. Beyers, R. E. Scheuerlein, E. J. O'Sullivan, S. L. Brown, J. Bucchignano, D. W. Abraham, Y. Lu, M. Rooks, P. L. Trouilloud, R. A. Wanner, and W. J. Gallagher, *J. Appl. Phys.*, **85** (1999) 5828.
- [48] H. Kang, K. Bessho, Y. Higo, K. Ohba, M. Hashimoto, T. Mizuguchi, and M. Hosomi, Digest of Technical Papers, IEEE INTERMAG Europe Magnetism Conference, 2002, BB4.
- [49] D. Wang, C. Nordman, J. M. Daughton, Z. Qian, and J. Fink, *IEEE Trans. Magn.*, **40** (2004) 2269.
- [50] W. H. Butler, X. G. Zhang, T. C. Schulthess, and J. M. MacLaren, *Phys. Rev. B (Condens. Matter & Matter Phys.)*, **63** (2001) 054416/1.
- [51] J. Mathon and A. Umerski, *Phys. Rev. B (Condens. Matter & Matter Phys.)*, **63**(2001) 220403/1.
- [52] S. Yuasa, *Jpn. J. Appl. Phys.*, **43**(2004) L588.
- [53] D. D. Djayaprawira, INTERMAG ASIA 2005: Digests of the IEEE International Magnetism Conference, pp. 234, 2005.
- [54] S. Ikeda, J. Hayakawa, Y. M. Lee, R. Sasaki, T. Meguro, F. Matsukura, and H. Ohno, *Jpn. J. Appl. Phys.*, **44** (2005) L1442.
- [55] S. Ikeda, J. Hayakawa, Y. M. Lee, T. Tanikawa, F. Matsukura, and H. Ohno, *J. Appl. Phys.*, **99** (2006)08A907.
- [56] J. Hayakawa, *Appl. Phys. Lett.*, **89** (2006)232510.
- [57] J. Hayakawa, S. Ikeda, Y. M. Lee, M. Yamanouchi, D. Chiba, T. Dietl, Y. Ohno, and F. Matsukura, International Symposium on Advanced Magnetic Materials and Applications, 2007.
- [58] J. C. Slonczewski, *Phys. Rev. B*, **39** (1989) 6995.
- [59] J. M. MacLaren, X. G. Zhang, and W. H. Butler, *Phys. Rev. B*, **56** (1997) 11827.
- [60] I. I. Oleinik, E. Y. Tsymbal, and D. G. Pettifor, *Physical Review B*, **62**(2000)3952
- [61] Novel materials for magnetic tunnel junctions, Christian Kaiser, Ph.D Dissertation, RWTH Aachen University, Germany, 2004.
- [62] E. L. Wolf, *Principles of Electron Tunneling Spectroscopy*, Oxford Scientific Publications (1985).
- [63] Jagadeesh S. Moodera, Janusz Nowak, and Rene J. M. van de Veerdonk, *Phys. Rev. Lett.*, **80** (1998) 2941.
- [64] N. Nishimura, T. Hirai, A. Koganei, T. Ikeda, K. Okano, Y. Sekiguchi, and Y. Osada, *J. Appl. Phys.*, **91** (2002) 5246.

Chapter 2

Experimental methods

2.1 Deposition of thin film

Deposition can occur by physical or chemical means (ex: Chemical Vapor Deposition) [1]. In the case of evaporation, a crucible with source material is heated, leading to evaporation of the source atoms. Due to the low vacuum pressure, the evaporated atoms move collision-free through the vacuum chamber and condense on the substrate.

Physical processes are used in deposition, such as sputtering and ion beam deposition. The physical process behind these two methods is similar, as in both techniques the material is sputtered from a target on the substrate. The term “Sputtering” was first used in the 1920s by I. Langmuir, and K. H. Kingdon and derives from Latin “sputare” (to emit saliva with noise) [2]. It describes a deposition process that was originally discovered about 150 years ago by Grove (1852) and Plücker (1858) where high energetic particles are generated which erode the surface of a target. The basic concept of sputtering is ejection of surface atoms from the target surface by momentum transfer by bombarding ions. The substrate is placed in a vacuum chamber

with the source material, named a target, and an inert gas (such as argon) is introduced at low pressure. A gas plasma is struck using an RF power source, causing the gas to become ionized. The ions are accelerated towards the surface of the target, causing atoms of the source material to break off from the target in vapor form and condense on all surfaces including the substrate.

2.1.1 Description of RF sputtering

The usefulness of RF methods for sputtering nonconducting materials is based upon the fact that a self-bias voltage, negative with respect to the plasma floating potential, develops on any surface that is capacitively coupled to a glow discharge. When an alternating voltage is applied to such an electrode, more electron current flows when the electrode is positive relative to the floating potential than ion current flows when the

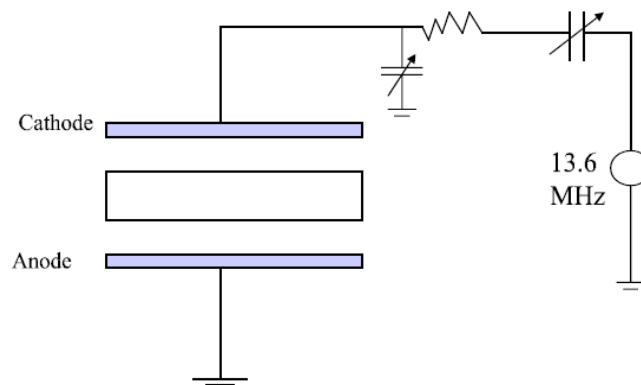


Fig. 2.1. Schematic drawing of a RF sputter apparatus.

electrode is negative relative to the floating potential. Fig. 2.1 shows a schematic drawing of a typical RF planar-diode-sputtering configuration in which a nonconducting target is placed over one electrode and substrates are placed on the other one [3,4].

2.1.2 Description of cylindrical magnetron sputtering

The magnetron sputtering method is used to deposit a target material, and effect of the magnetron can be described as a closed drift path of crossed electric and magnetic

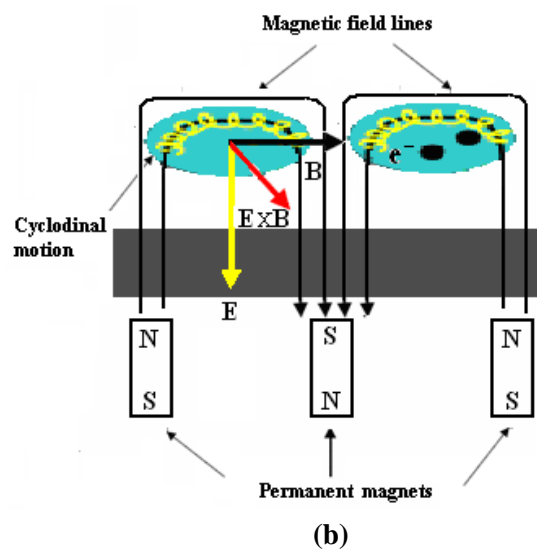
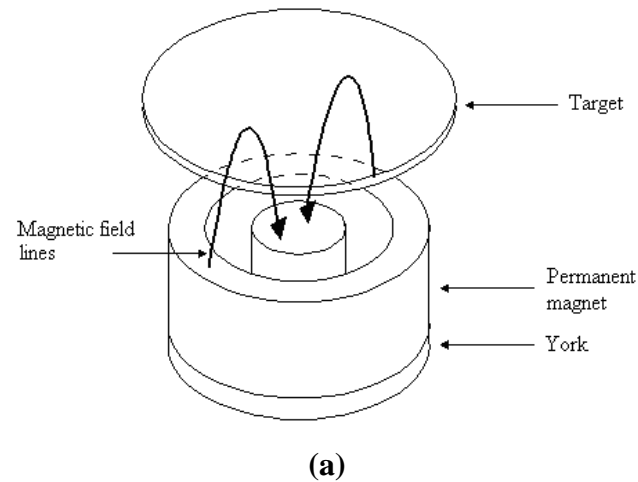


Fig. 2.2. (a) The configuration permanent magnets under target, and (b) geometry and electron motion of magnetron sputtering.

fields for electrons in a plasma discharge. For a simple cylindrical magnetron cathode, the arrangement consists of the cylindrical cathode (target) backed by permanent magnets that provide a toroidal field, with field lines forming a closed path on the

cathode surface as shown in Fig. 2.2. The difference in the mobilities of the ions and the electrons causes a positive ion sheath to be developed close to the target cathode, floating at a negative potential relative to the plasma. Because of the field due to the ion sheath at the cathode, ions are extracted from the plasma and accelerated to strike the target, resulting in the sputtering of the target material. The produced secondary electrons, upon entering the region of crossed electric (E) and magnetic (B) fields, are trapped in orbits that permit long travel distances close to the cathode. In the zones of the efficient electron trapping, the electron density reaches a critical value, at which the ionization probability due to the trapped electrons is at its maximum. This means that a higher rate of secondary electron production by high-energy positive ions is not necessary for effective sputtering.

The sputtering rate is influenced by the distance between target and substrate, the applied voltage, and to a lesser degree by the sputtering gas pressure. The sputtering rate is approximately inverse proportional to the distance and - above the plasma ignition threshold value - proportional to the voltage. With these parameters fixed, the thickness of a deposited film can be determined with the time of deposition and the film thickness-derived sputtering rate of a previously measured reference sample.

2.1.3 Preparation of the sample

All the samples described in the work were prepared on Si substrates with an oxidized surface layer (500 nm) using RF magnetron sputtering system. Before placing Si substrates with an oxidized surface layer (500 nm) on the sputtering chamber, it has been cleaned by Aceton and IPA for 5 minutes, respectively, using ultrasonic bath, to remove foreign materials and grease which may be attached on the surface of the substrate. Prior to the sputtering, so-called reverse-sputtering (substrate sputtering) was

performed after the chamber was evacuated to a low base pressure using a turbo molecular pump. The reverse-sputtering is the process of cleaning the substrate on atomic level to smooth out any uneven surface irregularities and to knock out top layered alien contaminations present on the substrate. Another advantage of the reverse-sputtering of the substrate is to enhance the adhesive force between sputtered atom and the substrate surface. Presputtering was also performed for cleaning the target surface before the sputtering deposition.

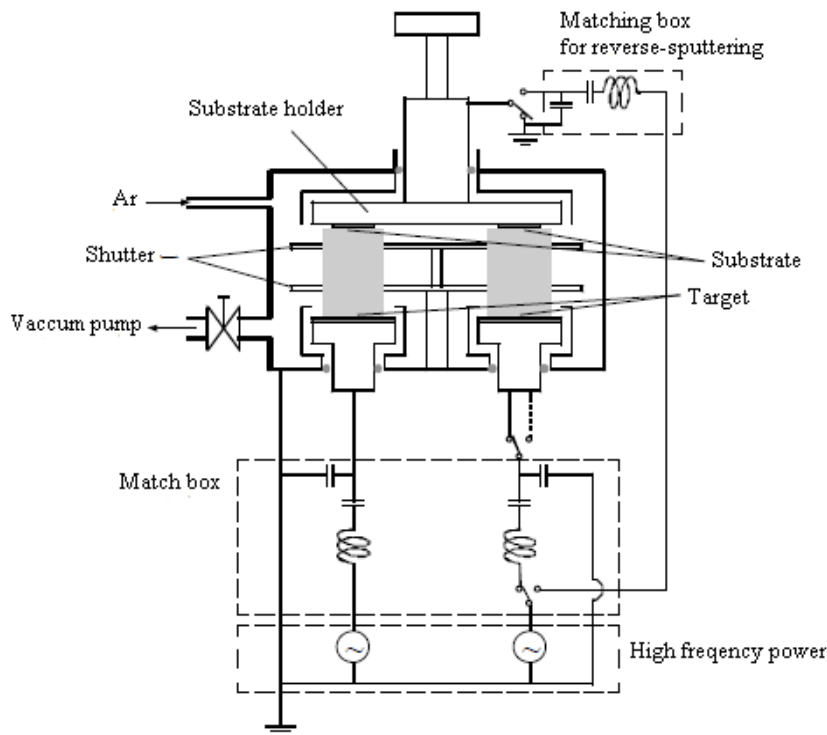


Fig. 2.3. Schematic diagram of 3-target RF magnetron sputtering system.

SiN(10nm) / TbFe (80 nm) / SiN(10nm) trilayer films were prepared by using 3-target RF magnetron sputtering (Shimadzu HSR-522) depicted in Fig. 2.3. Prior to film deposition the system was baked overnight at temperature of about 400 K and

evacuated using a turbo molecular pump to the pressure of 2×10^{-5} Pa. To explore the composition dependence of the magnetic properties of TbFe films, Tb chips were placed on the Fe target. RF-generator provides powers of 100 W for SiN target and 150 W for Fe target with Tb chips, respectively. Argon gas of purity (99.9999%) was used as the sputtered gas and the working pressure was set to be constant of 1.33 Pa.

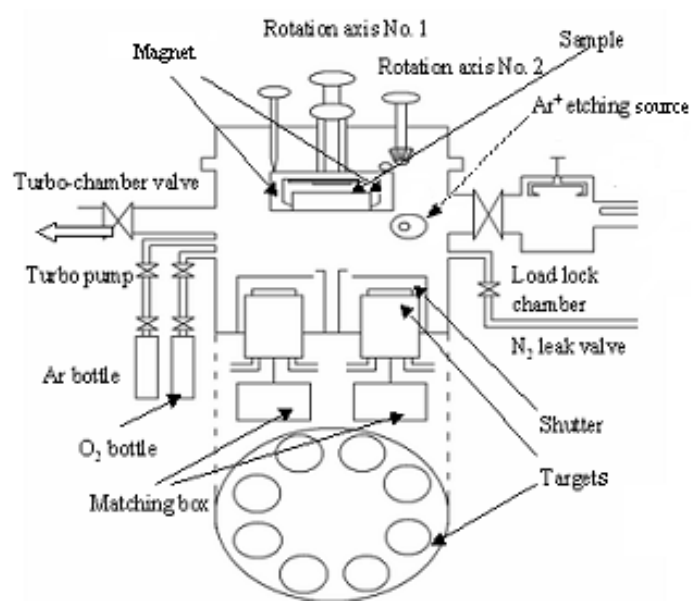


Fig. 2.4. Schematic diagram of 8-target magnetron sputtering system.

The MTJ stack composed of RE-TM alloys was prepared using 8-target RF magnetron sputtering system, as depicted in Fig.2.4. This system contains both a main chamber and a load-lock chamber, and transfer arm is utilized to transfer the samples between these two chambers. The base pressure of main chamber is less than 2.0×10^{-7} Pa and the pressure of load-lock chamber is less than 1.0×10^{-5} Pa. TbFe layers were deposited by co-sputtering of Tb and Fe targets. Oxide barriers were fabricated by

plasma oxidization of the Al metal target. The O₂ plasma was ignited on the Al₂O₃ target flowing O₂ gas at a pressure of 4 Pa.

5-target sputtering system was used to deposit the metallic top electrode, and insulating layer between top and bottom electrodes for the MTJ fabrication. The background pressure of chamber is less than 2.0×10^{-5} Pa. The sputtering conditions for Al top electrode and Al₂O₃ insulating layer are tabulated in Table 2.1.

Table 2.1. Sputtering condition using 5-target sputtering.

Target	power [W]	Ar pressure [Pa]
Al ₂ O ₃	200	0.4
Al	150	0.4

2.2 Process of sample

2.2.1 Lithography

Lithography is the process of defining the regions or patterns on the wafer where the material is to be deposited or removed, or where dopants are to be introduced.

2.2.1.1 Photo-lithography technique

Photo-lithography, including contact printing, proximity printing and projection printing, is a special technique used to transfer a pattern designed on a mask, onto a photosensitive resist that covers the sample. The resist patterns are transferred to the layer stacks either by deposition of additional films followed by the lift-off of the resist (positive lithography) or by ion beam etching (negative lithography). Therefore, there are two alternative techniques that are generally used to obtain patterned samples: i) etching and/or ii) lift-off techniques, seeing Fig. 2.5

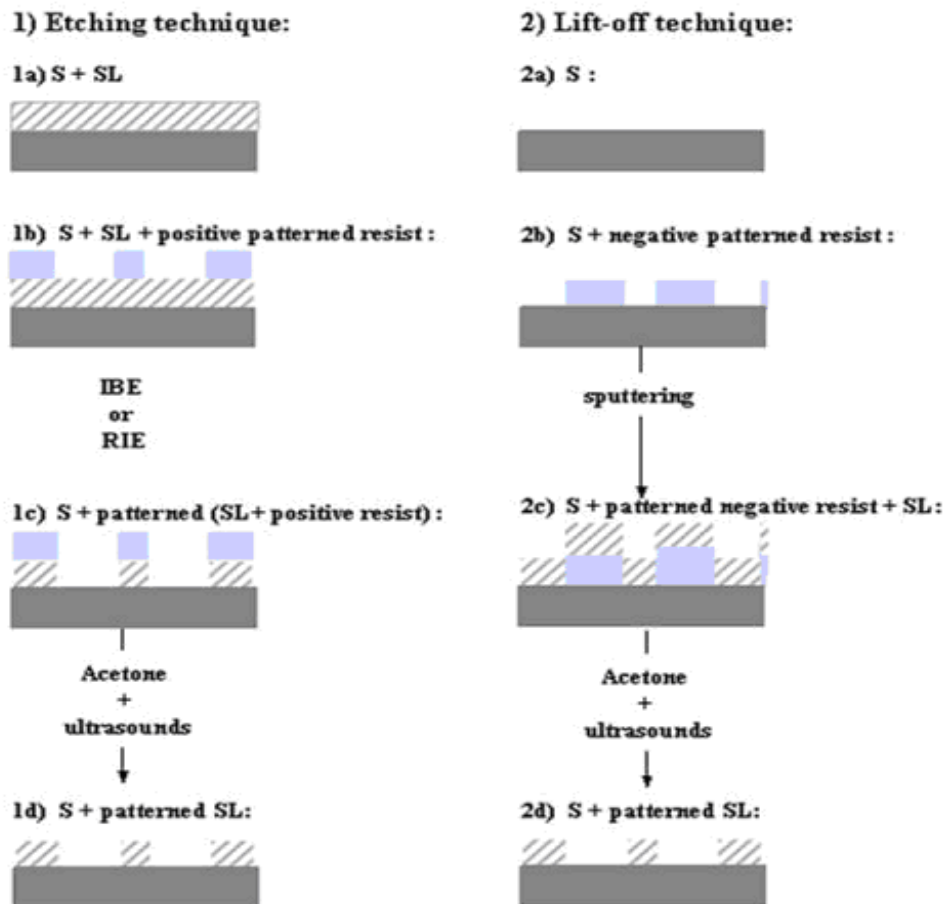


Fig. 2.5. Etching and lift-off techniques. S is substrate, SL is sputtering layer.

i) The etching technique

For etching process, a photoresist is spun onto the film deposited on the substrate and the mask design is transferred on the photo-resist. Then, the entire sample surface is etched resulting in non-etched regions, which are covered with resist, and etched regions, which are not covered. After the etching of the film, the resist is dissolved by a solvent in an ultrasonic bath.

ii) The lift-off technique

In this case, after the mask design was transferred on the resist, the thin film is deposited on the entire of the sample. Then, the deposited film onto the resist are

removed by a solvent in an ultrasonic bath, obtaining the patterned sample. For the fabrication of the MTJ, both etching and liftoff techniques were employed, while for the patterned TbFe film only the etching process was used.

2.2.1.1.1 Photoresist (PR) components

In general, photoresist is made up of the following three chemical components [5]:

1. Polymer - some types of polymers such as rubber are used to form the chemical backbone of the photoresist.
2. Solvent - a solvent is used to keep the polymer in solution (keeps the photoresist a liquid for the spin coating). The solvent controls the viscosity of the PR.
3. Photo Active Compound (PAC) - The photo active compound is the portion of the photoresist that actually reacts to the exposing light.

In a negative photoresist, the PAC forms bonds between the polymer molecules during exposure (cross-linking). The polymers cross-linked by the PAC hold onto the substrate during developing, so that the exposed portion of the photoresist remains on the substrate. The unexposed portion of the photoresist has not cross-linked and the polymer is dissolved in the developer.

In a positive photoresist the polymer is insoluble in the developer prior to any exposure. When the photoresist is exposed - the PAC reacts with the polymer to break down the polymer into compounds that are soluble in the developer.

2.2.1.1.2 The process of photolithography

Step 1) Substrate cleaning and dehydration prior to photolithography

A brand new sample may only require an isopropyl alcohol (IPA) or methanol rinse. If there is grease on the wafer, methylene chloride may be required to remove it. If the wafer has been coated with resist before, this should be stripped before recoating.

Prior to the application of resist to a sample, the sample must be free of moisture and contaminants, both of which cause a multitude of resist processing problems. In this work, acetone and IPA rinse in ultrasonic bath was carried out for 5 min, respectively, to remove particles or grease on the sample. After that, dehydration baking of 170 °C for 2 min on a hot plate was performed to eliminate any moisture adsorbed by sample surfaces, since hydrated substrates result in adhesion failures.

Step 2) Priming

If necessary, after the dehydration baking, the wafer is coated with a pre-resist priming layer designed to enhance the adhesion properties of the wafer even further. One of the most common primers used for this purpose is hexamethyldisilazane (HMDS). This is especially important for samples that oxidize easily (silicon, for example). The oxides will then bond to water vapor available in the air. When the PR is

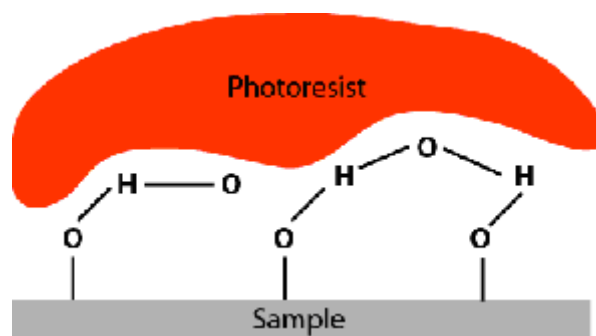


Fig. 2.6. The cartoon showing photoresist directly coated the sample with oxidized surface [6].

then coated onto the sample, the PR will adhere to the H_2O and not to the sample, see Fig. 2.6.

After dehydration baking these oxidized samples, it is important to spin coat them first with HMDS primer. The HMDS primer will bond with the oxide groups to seal out

the moisture, as shown in Fig. 2.7. In addition, the $\text{Si}(\text{CH}_3)_3$ groups are compatible with the PR, creating adhesion between the sample and the PR.

It is important to make sure that the sample is not coated with an excess amount of HMDS, as it reduces the photosensitivity of PR. Resist coating must follow as soon as possible after priming (within an hour after priming).

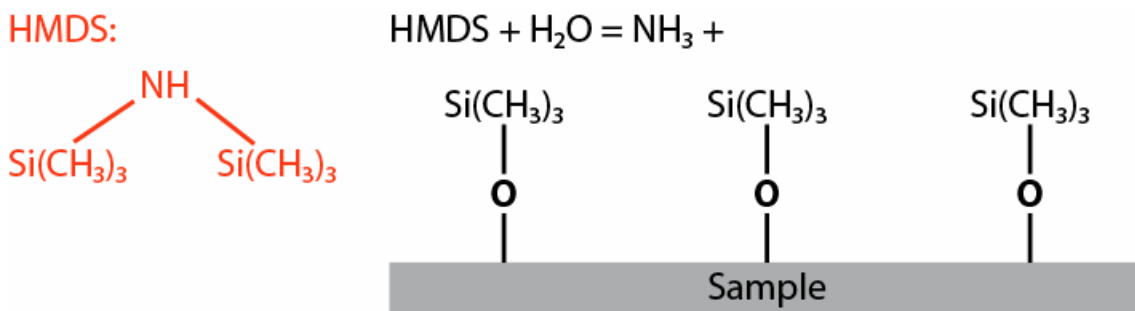


Fig. 2.7. The carton showing HMDS bond with oxide group [6].

Step 3) Resist coating

Resist coating, producing a uniform, adherent, and defect-free resist film of required thickness over the sample, is usually performed by spin-coating. Spin-coating consists of dispensing the resist solution over the sample surface and rapidly spinning the wafer until it becomes dry. The physics of spinning is complicated, and depends strongly on the evaporation rate of the solvent used. This is why there are only a few solvent systems in use for resist. Of the two types of photoresist, positive photoresist is used almost exclusively. Positive photoresists are more expensive than negative photoresists, but positive photoresists are capable of much better resolution [5]. Resist spinning thickness T depends on spin speed ω (rpm), solution concentration C (the polymer concentration in grams per 100 ml solution), and molecular weight (measured

by intrinsic viscosity η). There is half-empirical formula to express their relationship [7]:

$$T = \frac{KC^\beta \eta^\gamma}{\omega^\alpha} \quad (2.1)$$

here, K is a calibration constant. Once the various exponential factors (α , β and γ) have been determined the equation can be used to predict the thickness of the film that can be spun for various molecular weights and solution concentrations of a given polymer and solvent system. Equation (2.2) was found to be true for S1813 resist which was used in this work [8].

$$T \propto \omega^{-0.5} \quad (2.2)$$

The units of T and ω is nm and krpm, respectively. The proportional constant in this work is almost same to that of reference [8], and around $3000[\text{nm}/(\text{krpm})^{1/2}]$.

Step 4) Soft bake

A pre-exposure bake, or soft bake, is used to: 1) drive away the solvent from the spun-on resist; 2) improve the adhesion of the resist to the wafer; and 3) anneal the shear stresses introduced during the spin-coating. Soft baking may be performed using one of several types of ovens (e.g., convection, IR, hot plate). Soft-bake ovens must provide well-controlled and uniformly distributed temperatures and a bake environment that possesses a high degree of cleanliness. This is a critical step in that failure to sufficiently remove the solvent will affect the resist profile, as will excessive baking, which destroys photoactive compound and reduces sensitivity. The photo-resist S1813 was pre-baked at 110 °C for 10 min in the convection oven in this study.

Step 5) Exposure

After the sample has been coated with photoresist and subjected to soft baking, it has to undergo exposure to some form of radiation that will produce the pattern image

on the resist. Usually an UV lamp with proper intensity is used to illuminate the resist. The pattern is formed on the wafer using a mask, which defines which areas of the resist surface will be exposed to radiation and those that will be covered. The mask is a glass or plastic plate, onto which the patterns that we want to transfer on the sample are designed as a succession of transparent and opaque surfaces. It can be negative or positive. A positive mask corresponds to opaque regions associated to the designed geometries. The chemical properties of the resist regions struck by radiation change in a manner that depends on the type of resist used. Irradiated regions of positive photoresists will become more soluble in the developer, thus positive resists form a positive image of the mask on the wafer. Negative resists form a negative image of the mask on the wafer because the exposed regions become less soluble in the developer. It is important to keep the mask as close to the sample as possible by using the high precision vacuum seal on the aligner. This reduces diffraction of light caused by the gap between the mask and the sample, and hence improves the resolution. This also makes a steady distribution of UV light across all of the exposure area. In this work, resist S1813 on the sample was exposed to the mixed light of g-line (436 nm), h-line (405 nm) and i-line (365 nm) offered by high pressure Hg lamp using mask alignment (Canon PLA502F).

Step 6) Post exposure bake

A post-exposure bake, or PEB, is used to: 1) reduce standing waves in regular positive resist; 2) rearrange the overexposed and underexposed PR molecules; 3) smooth PR sidewall and improve resolution. For the same kind of PR, PEB usually requires a higher temperature than soft bake. Insufficient PEB will not completely eliminate the standing wave pattern, while over-baking will cause polymerization and

affects photoresist development. Post exposure bake was carried out at 90 °C for 20 min in this case.

Step 7) Development

The development process involves chemical reactions wherein unprotected parts of the resist get dissolved in the developer. As a function of the resist used (positive or negative), the lithographic process leads to a positive or negative reaction between the photosensitive substance and the UV irradiation. After a positive reaction, the resist that has been irradiated is developed while in a negative one the non-irradiated region is developed. Consequently, as a function of the mask polarity and of the resist type we have two situations: i) a positive mask and a positive resist is equivalent to a negative mask and a negative resist, and ii) a positive mask and a negative resist is equivalent to a negative mask and a positive resist. Development time is critically dependent on the temperature, humidity and exposure condition.

A good development process has a short duration (less than a minute), results in minimum pattern distortion or swelling, keeps the original film thickness of protected areas intact, and recreates the intended pattern faithfully. Development is carried out either by immersion developing, spray developing, or puddle developing. Regardless of method used, it should always be followed by thorough rinsing and drying to ensure that the development action will not continue after the developer has been removed from the wafer surface. In this work, the sample was developed in SHIPLEY MF CD-26 DEVELOPER. The sample was soaked for 15 sec and agitated softly for 45 sec in developer. Followed by puddling in pure water for 1 min.

2.2.1.1.3 Theoretical limits of photo lithography

For contact and proximity printing, the wavelength value of the incident irradiation, the thickness of the resist and the performance of the mask aligner limit the spatial resolution of the process. The resolution of a grating is limited by diffraction [9]:

$$2b_{\min} = 3\sqrt{\lambda(s + \frac{z}{2})} \quad (2.3)$$

where b is the period of the grating, λ is the wavelength of the light, z is the photoresist thickness, and s is the height above the mask. In contact printing, s is zero. Contact printing was used to define features on the chips, as it gives good resolution and minimises the effect of vibration. If we assume that the wavelength of the light λ in contact printing is $0.4 \mu\text{m}$ and photoresist thickness is $1.2 \mu\text{m}$, the b_{\min} is about $0.7 \mu\text{m}$ by substituting the values into the equation above. In practice the resolution is often limited by the uniformity of the resist coverage and debris between mask and wafer.

2.2.1.2 EB lithography

Because of its diffraction limit, conventional optical or ultraviolet photolithography is becoming increasingly inadequate. Other lithography techniques, which use different forms of radiation, including extreme UV, x-ray, electron beams, and ion beams, to offer higher resolution, are growing in importance. A great deal of research has been done on these techniques to scale lithography technology down to the nano-scale arena. Electron beam lithography (EBL) is a specialized technique for creating high resolution patterns. The process for fabrication of EBL is almost similar to that of photolithography. EBL offers higher patterning resolution than the conventional

optical lithography because of the shorter wavelength λ ($=1.2/\sqrt{V_b}$) possessed by the 10-50 keV accelerating voltage V_b .

2.2.1.2.1 Principle of operation

The EBL system is very similar to a scanning electron microscope (SEM), where an electron beam is focused to a spot onto the substrate and scanned over the desired field of view. The major differences between an SEM and an EBL system is that in an SEM, the emphasis is on capturing signals emitted from the sample, due to the incident electron beam, for imaging and analysis, while an EBL system is focused on controllably applying the desired dose of electrons in a localized pattern on the substrate [10]. Therefore, the EBL system includes a highly accurate positional control stage using laser interferometry to measure the position of the stage and sample, a Faraday cup with a picoampere current detector, high speed blanking system for blocking the electron beam during the stage movement, sophisticated software and routines for automatically correcting for focus, stigmatism, and a computer interface to feed data from a CAD file into the instrument. For this research, the JEOL JBX-6000FS EBL system was utilized. It comprises substrate holders with an interferometrically controlled xy stage, high quality vacuum units, a vibration isolated electron optical column, a wafer handling system that automatically feeds wafers to the system and unloads them after processing; and a computer system that controls the equipment. The system is illustrated in Fig. 2.8. The JBX-6000FS/E forms a high current density electron beam using a thermal field emission gun with a ZrO/W emitter. The system is capable of high-speed pattern exposure on high-resolution (low sensitivity) resists. The JBX-6000FS/E uses in-lens electrostatic deflector free from hysteresis, assuring high

stability. It incorporates two different objective lenses for fine and ultra fine pattern exposures with a beam diameter range of 5 nm to 200 nm.

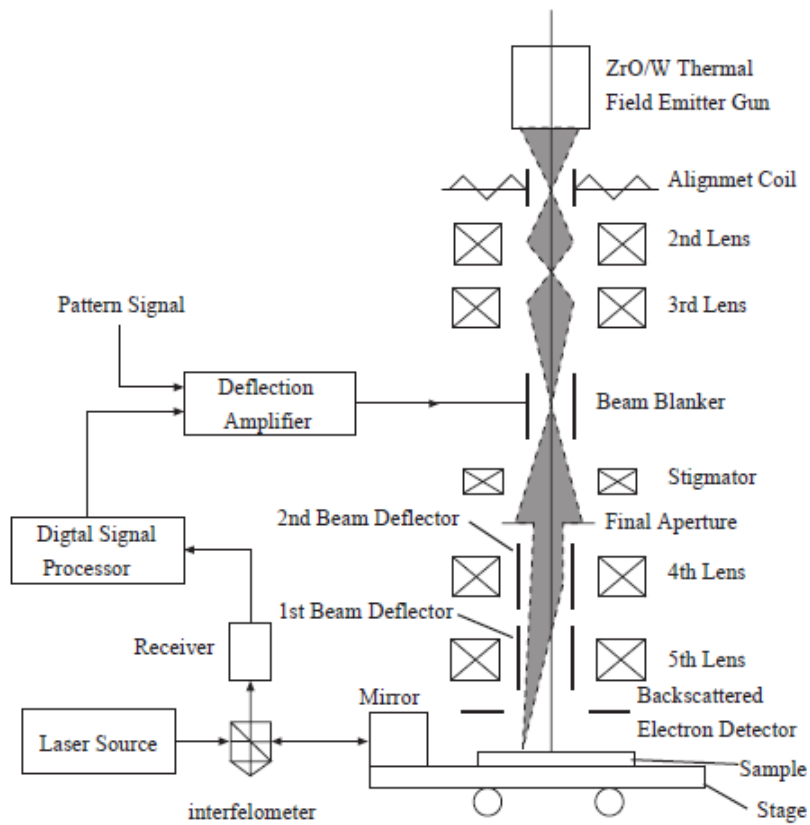


Fig.2.8. The schematic diagram of EB exposure system.

2.2.1.2.2 EB resist

The resists used for microlithography must have a high resolution, high sensitivity, and good dry-etch resistance as basic properties. Usually, the e-beam resists are high molecular-weight polymers dissolved in a liquid solvent. The polymer changes its

structure when exposed to radiation, including electron beam radiation. Electron beam resists can be either positive or negative [11].

A. Positive resists

Polymethyl methacrylate (PMMA) was one of the first resists developed for EBL and remains the most commonly used positive resist that has a moderate glass transition temperature of 114 °C. The PMMA comes in powder form and is dissolved in a solvent, such as anisole or chlorobenzene, of desired concentration. PMMA has extremely high resolution, and its ultimate resolution has been demonstrated to be less than 10 nm [9]; its major problems are the relatively poor sensitivity, poor dry etch resistance. Other important positive resists include PBS (PolyButene-1-Sulfone) and EBR-9 (a copolymer of trifluoroethyl α -chloroacrylate and tetrafluoropropyl α -chloroacrylate) which have high sensitivity and ZEP (a copolymer of chloromethacrylate and methylstyrene) which has high-resolution. In this work, ZEP520A is used for EB resist. ZEP520A is high performance positive EB resists which show high resolution, high sensitivity and dry etch resistance.

B. Negative resists

Negative resists tend to have less bias but they have problems with scum and swelling during development and bridging between features. Popular negative e-beam resists consist of the Shipley advanced lithography (SAL) product line, an epoxy copolymer of glycidyl methacrylate and ethylacrylate [P(GMA-EA)], also known as COP, and a partially chloromethylated polystyrene (CMS). Also, PMMA can exhibit negative tone when exposed to a dose one order of magnitude higher. While COP has high sensitivity, CMS possesses modest resolution at modest sensitivity.

2.2.1.2.3 The challenge of E-beam lithography

The electron de Broglie wavelength of a typical EBL operating condition, acceleration voltage of 50 keV, is less than 10 pm or 0.01 nm, which is far below typical atomic sizes. Hence, diffraction is not a limiting factor of the resolution. Ideally, e-beam diameters are possible on the order of 1 nm. However, The resolution achievable with any resist is limited by two major factors: 1) the tendency of the resist to swell in the developer solution and 2) electron scattering within the resist [11].

A. Resist swelling

Resist swelling occurs as the developer penetrates the resist material. The resulting increase in volume can distort the pattern, to the point that some adjacent lines, that are not supposed to touch, become in contact with each other. Resist contraction after the resist has undergone swelling can also occur during rinsing. However, this contraction is often not enough to bring the resist back to its intended form, so the distortion brought about by the swelling remains even after rinsing. Unfortunately, a swelling/contraction cycle weakens the adhesion of the smaller features of the resist to the substrate, which can create undulations in very narrow lines [12]. Reducing resist thickness decreases the resolution-limiting effects of swelling and contraction.

B. Scattering or proximity effect

When the electron beam strikes the resist solid, many of the electrons experience small-angle forward scattering, which tends to enlarge the initial beam size. As the electrons penetrate through the resist into the substrate, some of them undergo large angle scattering events leading to backscattering, in which these electrons return back through the resist in a region far from the desired exposure. This causes additional

exposure in the resist and is also known as the e-beam proximity effect. Also, as the primary electrons slow down, much of their energy is dissipated in the form of secondary electrons in which a small portion may have significant energies, on the order of 1 keV. These so-called fast electrons are responsible for the bulk of actual resist exposure and can contribute to the proximity effect in the range of a few tenths of a micron.

Some simple remedies include using a thin resist that is less than the feature size or a thin coating between the resist and the substrate to partially “filter” the secondary and some backscattering electrons. The most systematic way is dose control. Different feature sizes have different dose requirements. If the pattern is uniform, the overall dose is simply adjusted until the desirable pattern size is achieved. If the pattern is rather complex, dose modulation should be considered.

2.2.2 Etching

Etching is the process of removing regions of the underlying material that are no longer protected by photoresist after development. In general, there are two classes of etching processes: wet etching where the material is dissolved when immersed in a chemical solution, and dry etching where the material is sputtered or dissolved using reactive ions or a vapor phase etchant. Wet etching is accomplished by submersion of the sample in an acid bath. Wet etch processes can lead to undercutting, resulting in an isotropic etch profile where the vertical etch rate is approximately equal to the horizontal etch rate (Fig. 2.9) [13]. As semiconductor manufacturers continue to shrink feature sizes, this undercutting becomes more intolerable, making wet etching a less desirable technique for material removal. Fortunately, dry etching techniques can be made anisotropic, and so can avoid significant undercutting of the resist pattern. Dry

etching uses plasma generated and free radicals to remove material only from the area dictated by a resist pattern created during the lithography step. Dry etching may be

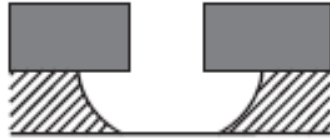


Fig. 2.9. Example of wet (isotropic) etching.

accomplished by any of the followings: 1) through chemical reactions that consume the material, using chemically reactive gases or plasma; 2) physical removal of the material, usually by momentum transfer; or 3) a combination of both physical removal and chemical reactions. Plasma etching is an example of a purely chemical dry etching technique. A radiofrequency (RF) energy ionizes the gas and forms the etching plasma, which reacts with the samples to form volatile products which are pumped away. Plasma etching systems have been developed that can effectively etch silicon, silicon dioxide, silicon nitride, aluminum, tantalum, tantalum compounds, chromium, tungsten, gold, and glass. On the other hand, physical sputtering and ion beam milling are examples of purely physical dry etching techniques. Physical etching processes are similar to sandblasting; argon gas atoms are used to physically bombard the layer to be etched, and a vacuum pump system is used to remove dislocated material. Sputter etching is one physical technique involving ion impact and energy transfer. The wafer to be etched is attached to a negative electrode, or "target," in a glow-discharge circuit. Positive argon ions bombard the wafer surface, resulting in the dislocation of the surface atoms. Power is provided by an RF energy source. Ion beam etching and milling are similar physical etching processes which use a beam of low-energy ions to dislodge

material. The ion beam is extracted from an ionized gas (argon or argon/oxygen) or plasma, created by an electrical discharge. Lastly, reactive ion etching is an example of dry etching that employs both physical and chemical processes. Reactive ion etching (RIE) is a combination of chemical and physical etching. During RIE, a wafer is placed in a chamber with an atmosphere of chemically reactive gas (CF_4 or CCl_4) at a low pressure. An electrical discharge creates an ion plasma with an energy of a few hundred electron volts. The ions strike the wafer surface vertically, where they react to form volatile species that are removed by the low pressure in-line vacuum system.

There are different chamber geometries and plasma driving frequencies used in commercial plasma etch tools. Within them, Reactive Ion Etcher (RIE), and Inductively Coupled Plasma or Transformer Coupled Plasma (ICP or TCP) tool and Electron Cyclotron Resonance (ECR) tool are extensively used for dry etching [14]. In this research, ECR physical etching process is used to etch the sample. The system is shown in Fig.2.10. ECR tool is a low-pressure, high-density plasma source with permanent magnet. Microwaves (power 2.45 GHz) are injected axially through a dielectric window into the source plasma; a large resonant magnetic field is used (875 G). The source plasma that controls the ion/radical flux streams out into the process vacuum chamber where the sample is located. Due to higher driving frequency there is a higher ion flux generated than with ICP tools, thus providing for faster dry etching (and, thus, higher throughput). Since the operating pressure for ECR plasmas (typically < 1 mTorr, about 0.1 mTorr in this work) is also lower than for typical reactive ion etching (10~100 mTorr). The anisotropy of the etched features is greater in the former case, with substantially less ion-induced damage to the etched surface.

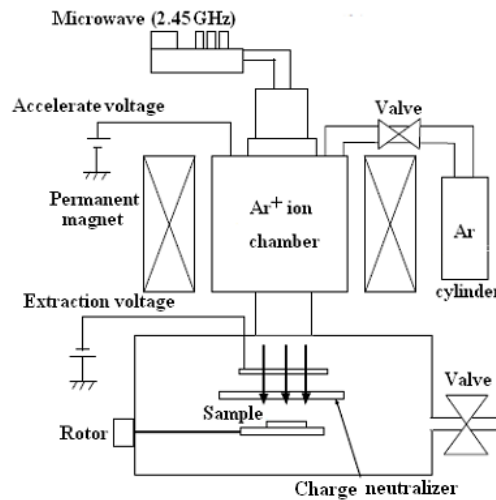


Fig. 2.10. Schematic diagram of ECR system.

2.2.3 Resist stripping

Resists are composed of polymers with a hydrocarbon backbone. The material properties of resists and their residues vary due to differences in the chemistry of the pendant groups on this backbone. Common to all resists is the fact that an insoluble, cross-linked hydrocarbon residue remains on the substrate after processing.

After pattern transfer it is necessary to remove or strip the resist. There are several ways to accomplish this. The simplest is to dissolve the photoresist away in acetone, Shipley 1165 Remover or AZ 300T. The latter two chemicals are more effective than acetone and leave less of a residue. The ZEP520A, EB resist, can be dissolved by ZDMAC Remover. Sidewall polymers from etching also tend to be highly resistant to wet-stripping chemistries. This problem causes plasma (“dry-ashing”) techniques to be preferred for polymer and residue removal in fabrication processes at reduced geometries. Sometimes a combination of soaking in remover and plasma stripping is required to remove stubborn resist (in fact, it is usually recommended to follow a wet strip with a brief plasma strip to remove resist

residues). If this does not work, you can resort to Nanostrip or Hot Piranha. These are acid etches specifically designed for the removal of organics. Unfortunately, both of these processes will also etch some thin films.

2.3 Measurement methods

Magnetic properties of TbFe thin films and MTJ stacks were measured by magneto-optical Kerr effect (MOKE) and alternating gradient field magnetometry (AGM). The microstructure was characterized by atomic force microscope (AFM) and Magnetic Force Microscope (MFM). The MR effect and I-V property of TMR junctions were measured by four-point probe method.

2.3.1 Magneto-optical Kerr effect (MOKE)

Magneto-optical Kerr Effect (MOKE) is a common technique used to investigate the static and dynamic properties of ferromagnetic samples. This effect is named after John Kerr who observed a rotation of the plane of polarization of the linearly polarized light when reflected from a polished iron plate in the field of a permanent magnet [15]. The surface-MOKE effect made its debut as an experimental technique to study magnetism in 1985, when it was first used to detect ferromagnetic hysteresis loops from epitaxial Fe deposited on Au(100) [16]. The MOKE is based on the interaction of polarized light with magnetic matter. On a microscopic level, MOKE is a consequence of the interaction between the electro-magnetic wave comprising the light and the electrons in the medium. An incident linearly polarized beam is reflected by the magnetic samples and experiences the transformation to elliptically polarized light. The detection of the Kerr rotation enables to measure a signal that is proportional to the magnetic moment of the ferromagnetic sample, the degree of rotation is proportional to

the magnetic moment at the film surface but is also strongly dependent on other parameters such as the magnetic composition, the angle of incidence, the probe wavelength and any material surrounding the film such as protective coatings. Because of this, MOKE is used only for qualitative analysis of films allowing measurements of the coercivity, the remanence ratio and the shape of the magnetic hysteresis. The MOKE setup is arranged in polar configuration to measure perpendicular magnetisation hysteresis loops. It consists of water-cooled electromagnetic coils, a Xe lamp, two

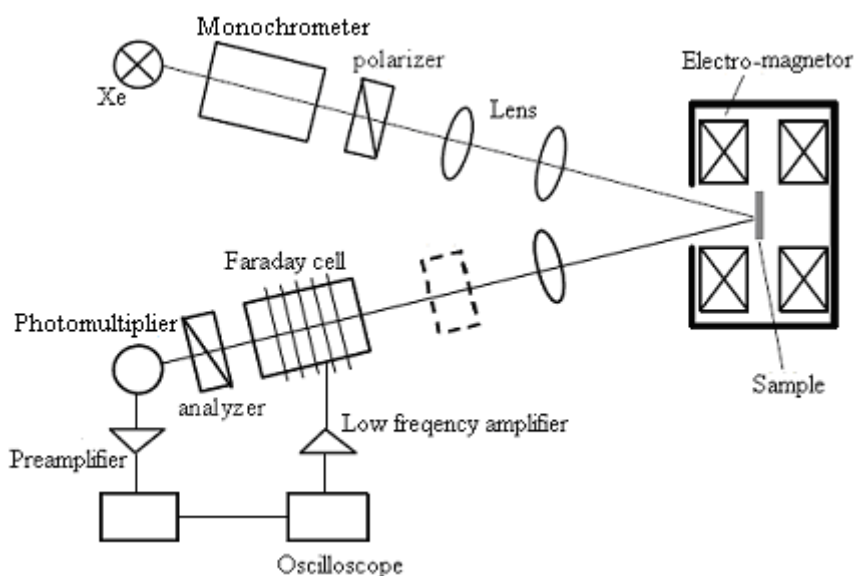


Fig. 2.11. Schematic of the MOKE setup.

polarizing elements (polarizer and analyzer) and a sensitive photodetector. The sample is mounted between the coils with a plastic holder and non-magnetic metal fasteners, and is placed between the polarizer and the analyzer (see Fig. 2.11). The electromagnets are manually operated with a current supply to provide a magnetic field perpendicular to the sample with a maximum strength of ± 1.6 T.

2.3.2 Alternating gradient field magnetometer (AGM)

Different types of magnetometers are used to measure the magnetic moment. One of these methods is the alternating gradient field magnetometer (AGM), which has a sensitivity exceeding (10^{-8} emu). The principle of the alternating gradient field magnetometer (AGM) is that the alternating field gradient exerts an alternating force on the sample, proportional to the magnitude of the field gradient and the magnetic moment of the sample. So as to determine the magnetic moment of the sample, the acting force has to be measured. The magnetic sample is mounted on the end of a cantilevered rod that incorporates a piezoelectric element. The sample is magnetized by a DC field and simultaneously subjected to a small alternating field gradient. The sample is mounted on the tip of a vertical extension rod, which is oriented along the z -axis, and the gradient field is along the x or the y -axis. The top end of the sample rod is attached to the bottom end of the piezoelectric element, as shown in Fig.2.12. The force of the field gradient on the magnetized sample produces a bending moment on the piezoelectric element, which generates a voltage proportional to the force on the sample. The output from the piezoelectric element is synchronously detected at the frequency of the gradient field. The amplitude of this voltage is proportional to the magnetic moment of the sample, which can be varied by changing the applied DC magnetic field H_{ext} . The gradient field varies in orders smaller than the coercive fields of the investigated sample and is applied by small coils placed in the greater field coils providing the magnetic bias field. The sensing element is composed of two polarized sheets of a metallized piezoelectric, which are cemented back to back to both sides of a thin brass vane [17~19]. The preamplifier is the front ends of a lock-in the amplifier, which automatically tracks the frequency of the AC current in the gradient coils. The main

advantages with respect to MOKE are the volume and the absolute magnetic moment sensitivity. For the AGM used in this research, the maximum field is 22 kOe and measurement frequency is from 100 Hz to 1000 Hz.

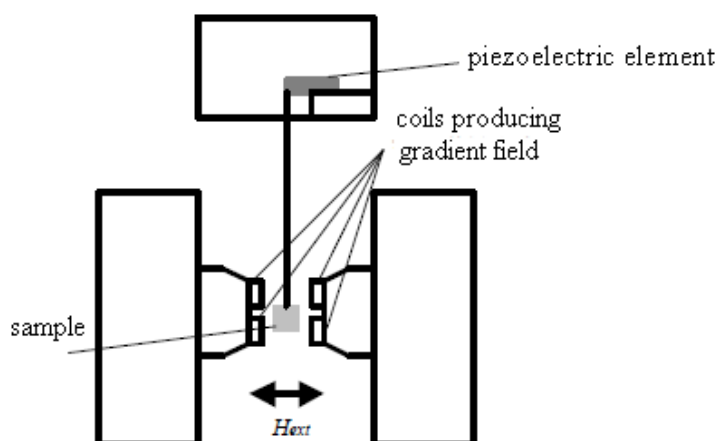


Fig. 2.12. Schematic diagram of AGM.

2.3.3 Atomic force microscopy (AFM)

AFM is one method of scanning probe microscopy (SPM) techniques. The AFM is useful for investigating surface profile of films and assessing their quality. A sharp tip located at the end of a cantilever is used to scan a sample surface with different modes (contact, non-contact, tapping). The AFM consists of several parts including a cantilever with a sharp tip, a laser generator, a position sensitive photodiode (PSD), and a set of piezoelectric tubes (PZT) as shown in Fig. 13. The atomic force microscopy tip usually consisted of a micron-sized silicon nitride pyramid on the end of a silicon nitride microcantilever which is a few hundred microns long and fabricated by semiconductor lithography and etching techniques. In this study, tapping mode is the method of operation for operation AFM. The working principal of tapping mode AFM

is that the cantilever is driven at its resonant frequency (often hundreds of kHz) as the tip is scanned over the surface. This is still contact with the sample, but the very short time over which this contact occurs means that lateral forces are dramatically reduced as the tip scans over the surface. Tapping mode is usually preferred to image samples with structures that are weakly bound to the surface or samples that are soft (polymers, thin films). There are also two other types of image contrast mechanisms in tapping mode:

1) Amplitude imaging. The feedback loop adjusts the z-piezo so that the amplitude of the cantilever oscillation remains (nearly) constant. The voltages needed to keep the amplitude constant can be compiled into an (error signal) image, and this imaging can often provide high contrast between features on the surface.

2) Phase imaging. The phase difference between the driven oscillations of the cantilever and the measured oscillations can be attributed to different material properties. For example, the relative amount of phase lag between the freely oscillating cantilever and the detected signal can provide qualitative information about the differences in chemical composition, adhesion, and friction properties.

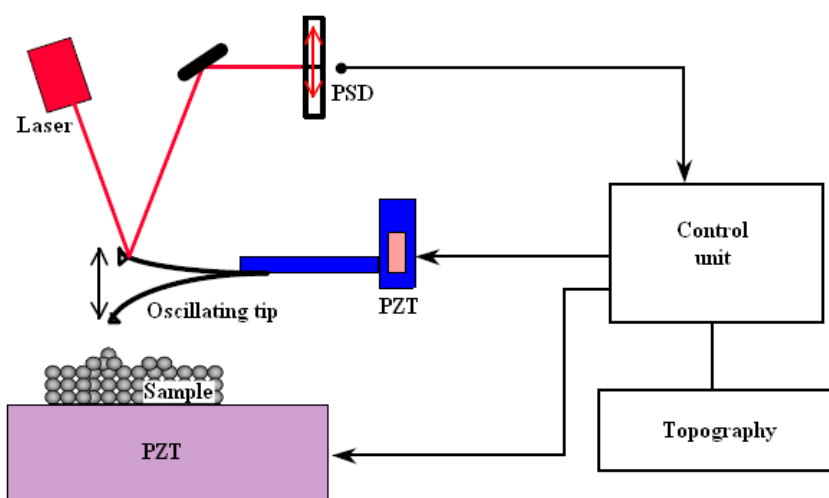


Fig. 2.13. The schematic diagram of the basic principle of AFM measurement.

2.3.4 Magnetic force microscopy (MFM)

Magnetic force microscopy (MFM) is a special measurement technique to characterize magnetic properties of sample with high spatial resolution. In general, there are three methods including constant frequency shift mode, constant height mode or tapping/lift mode to be used in MFM measurement [20~24]. The most common of the three modes is tapping/lift mode, developed by Digital Instruments [21].

The principle of the tapping/lift method in MFM measurement is that a tapping cantilever with special magnetized tip scans over the sample surface in order to obtain topography information and magnetic information of the sample surface at the same

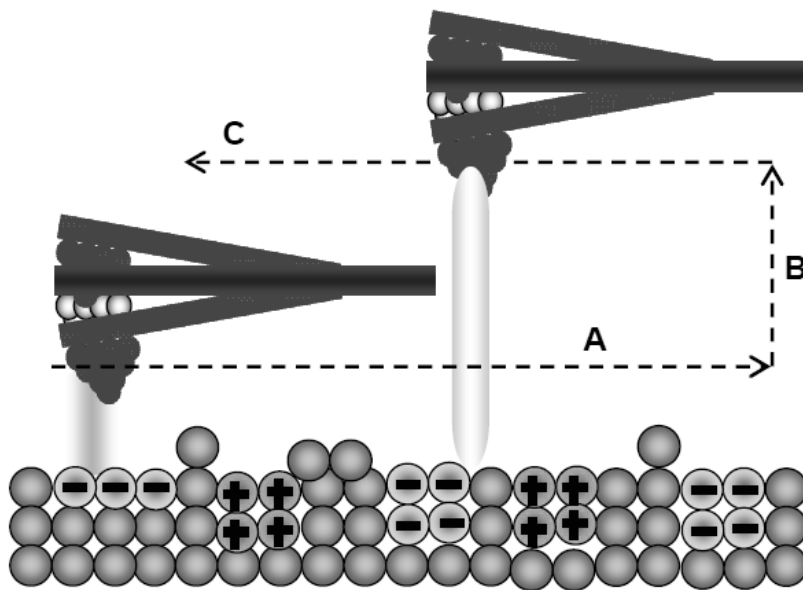


Fig. 2.14. Principle of magnetic force microscopy imaging. The cantilever moves along the surface to obtain topography and magnetize surface (A). Then, cantilever is slightly lifted (B) over surface and re-profiles topography to get the magnetic influence (C).

time. The tip for MFM is different from the AFM, which has a ferromagnetic material at the top of the tip. Then, the tip is slightly lifted, called lift mode, just above the sample

surface and re-scans the surface to monitor the magnetic influence between tip and magnetized surface. This magnetic influence can react with the free resonating frequency of the cantilever (f_x) by altering the frequency $f_x \pm \delta$. Therefore, bigger alternation of frequency represents stronger magnetic influenced area. To enhance the sensitivity, most MFM instrument oscillates the cantilever near its resonant frequency (around 100 kHz) with a piezoelectric element. Both hard and soft magnetic materials can be imaged by the magnetic force microscopy. Figure 2.14 shows the concept of MFM tape/lift mode technique [19,25].

2.3.5 TMR device characterization methods

The transport properties of MTJ multilayers are measured by 4-point probe station in this study. 4-point method is an accurate measurement for sample resistance by eliminating the contact resistance and spreading resistance. TMR effect and tunneling I-V characteristic are only happened when a current tunnel through an AlO_x barrier layer, therefore, the current direction must be designed to be perpendicular to the TMR film plan. This geometry is called as current-perpendicular-to-the-plane (CPP) measurement, as shown in Fig. 2.15. For I-V measurements of the junctions, a computer controlled current is applied and the voltage across the barrier is measured. The current was supplied by YOKOGAWA 7651 programmable current source. The voltage is measured using a Keithley 2182 nanovoltmeter. The I-V curve is normally taken by sweeping the current from a negative value to a positive value. Typically I-V diagrams are taken in the voltage range of (-500 to 500 mV). Magnetoresistance measurements were carried out using the same apparatus as described above where the sample was mounted between two magnetic coils. The magnetic field in this system is controlled by a DC power current source. A field of up to 1.8 T can be applied. The

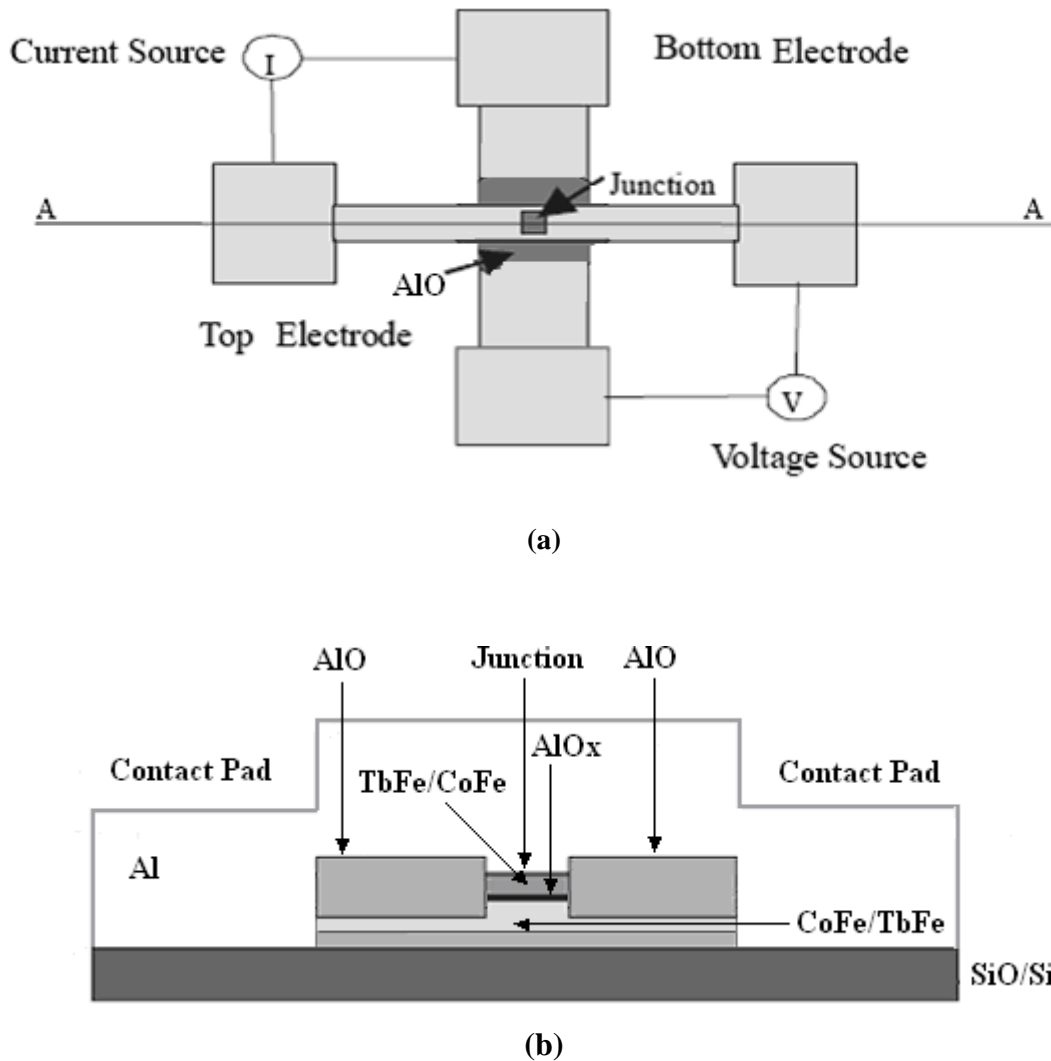


Fig. 2.15. (a) Top view of the TMR junction for the four points measurements and (b) its A-A cross section.

field is estimated from the current flowing the magnetic coils, which is recorded by the computer. During the magnetoresistance measurement, the junction is biased with a constant current and the voltage is monitored by sweeping the magnetic field. The bias dependence of the magnetoresistance is obtained by measuring the resistance R (V/I) at various bias voltage for the situation of parallel and anti-parallel alignment of the magnetization direction of the two ferromagnetic layers.

References

- [1] R. Waser; Nanoelectronics and information technology – Advanced electronic materials and novel devices; Wiley-VCH; Germany; 2003.
- [2] K.H. Kingdon and I. Langmuir, Phys. Rev., **22** (1923) 148.
- [3] P. D. Davidse and LM. Maissel, J. Appl. Phys., **37** (1966) 574.
- [4] Development of ferromagnetic/insulator/ferromagnetic devices for digital magnetic data storage and magnetic field sensors, Emad Azmy Sultan Girgis, Ruhr-Universität Bochum, Germany, Ph.D Dissertation, 2000.
- [5] Process Technologies for the 21st Century, <http://193.49.104.5>.
- [6] Alyssa Pasquale and Jong Kyu Kim, Prof. E. F. Schubert Group (Dept. of Electrical, Computer & Systems Engineering, Rensselaer Polytechnic Institute) Seminar, <http://www.ecse.rpi.edu/~schubert/Course-Teaching-modules/A36-The-photolithography-process.pdf>.
- [7] Teaching materials of Dr. H. Noh (Mechanical Engineering and Mechanics, Drexel University), <http://www.mem.drexel.edu/noh>.
- [8] Fabrication of superconducting nanowire single photon detectors, Joel K. Yang, Massachusetts Institute of Technology, master Dissertation, 2005.
- [9] The development of magnetic tunnel junction fabrication techniques, Clifford Alastair Elwell, Ph.D Dissertation, the University of Cambridge, 2002.
- [10] Unraveling photonic bands: characterization of self-collimation effects in two dimensional photonic crystals, Tsuyoshi Yamashita, Georgia Institute of Technology, Ph.D Dissertation, 2005.
- [11] A. A. Tseng, K. Chen, C. D. Chen, and K. J. Ma, IEEE Trans. on electronics packing manufacturing. **26**(2003)141.
- [12] http://www.siliconfareast.com/lith_electron2.htm.
- [13] M. Khoury and D. K. Ferry, J. Vac. Sci. Technol., **B14** (1996) 75.
- [14] <http://www.pall.com>.
- [15] J. Kerr, Philos. Mag., **3** (1877) 321.
- [16] S. D. Bader and E. R. Moog, J. Appl. Phys., **61** (1987) 3729.
- [17] H. Zijlstra, Rev. Sci. Inst., **41** (1970) 1241.
- [18] W. Roos, K. A. Hempel, C. Voight, H. Dedericks, and R. Schippan, Rev. Sci. Inst., **51** (1980) 612.

-
- [19] Development of ferromagnetic/insulator/ferromagnetic devices for Digital Magnetic Data Storage and Magnetic Field Sensors, Emad Azmy Sultan Girgis, Ruhr-Universität Bochum, Germany, Ph.D Dissertation, 2000.
- [20] E. Meyer, H. J. Hug, and R. Bennewitz, Scanning Probe Microscopy: The Lab on a Tip, Springer (2004).
- [21] <http://www.di.com>.
- [22] T. R. Albrecht, P. Grutter, D. Horne, and D. Rugar, J. App. Phys., **69**(1991) 668
- [23] Y. Martin, C. C. Williams, and H. K. Wickramasinghe. J. App. Phys., **61** (1987) 4723.
- [24] J. J. Siaenz, N. Garcia, P. Grutter, E. Meyer, H. Heinzelmann, R. Wiesendanger, L. Rosenthaler, H. R. Hidber, and H. J. Güntherodt, J. App. Phys., **62** (1987) 4293.
- [25] Instruction manual V. 4.11, Digital Instruments, Feb. 1996; Command reference manual V.5.12 Rev. B, April (2003).

Chapter 3

RE-TM alloys and their spin dependent tunneling in MTJ structure

3.1 Introduction

The alloys of rare earth elements, elements of the lanthanide series and ferromagnetic transition metals, Co, Fe and Ni, are usually denoted as rare-earth-transition-metal (RE-TM) materials. These materials display a wide variety of unique properties such as ferrimagnetic ordering, amorphous structures and perpendicular magnetic anisotropy in thin films that cannot be found in conventional materials. Discovered in 1973 by IBM researchers, RE-TM materials ushered in the modern era of high-density magneto-optic (MO) storage and remain to this day the industry's material [1]. For the MO storage application, the amorphous structure (which reduces the grain noise), tunable Curie temperature (which enables Curie point writing [2,3]), high perpendicular anisotropy [1] and high Kerr effect [3] are the most important. RE-TM films have also played important roles in the applications such as MEMS and actuators in the past years, due to their large magneto elastic energy densities which is

related to magnetic perpendicular Anisotropy [4~6]. Recently, RE-TM alloys have extensively studied for perpendicular magnetic recording, heat assisted magnetic recording (HAMR) [7,8] and perpendicular MTJ application [9~11].

In this chapter, rare earth – transition metal (RE-TM) alloys will be discussed emphasizing properties important for their use in thermally assisted MRAMs. The magnetic properties of RE-TM have been investigated as a function of temperature and films compositions and thickness. The high TMR effect, together with high thermal stability and suitable magnetic anisotropy illustrates the potential use of these materials in applications.

3.2 Material properties

The development of RE-TM materials can be traced back to the early works on RE-TM permanent magnets (SmCo_5). The magnetic properties of the rare earths are dominated by a partly filled 4f shell which can result in very high magnetic moments per atom. The exchange in RE metals is mediated by the 4s–5d conduction electrons via the RKKY interaction. Thus the Curie temperatures of RE metals are very low and the REs are unsuitable for practical applications. Research showed that the Curie temperature of REs could be increased by alloying with TM components, as a result of exchange coupling between RE and TM spins. Moreover, the RE elements in RE-TM alloys retain their high moments even at higher temperatures than the Curie temperature of the pure RE metals. We can obtain the permanent magnets by combining the high Curie temperature of the TM with the high moment of the RE element. For this application, light RE elements are used because these couple ferromagnetically with the TM moments giving rise to large saturation magnetization. By contrast heavy rare

earths (Gd to Lu) couple antiferromagnetically with the TM moments thereby reducing the net moment. This different coupling between the LRE and HRE can be understood from Hund's rule. Hund's rule states that the spin and orbital angular momenta couple antiparallely when the 4f shell is less than half-filled, because the lowest value of J lies lowest in energy. The total angular momentum can be written as: $J = |L - S|$. On the other hand, for a shell which is more than half-filled, the spin and orbital angular momenta prefer parallel alignment with each other, because the highest J is the lowest energy state. The total angular momentum can be denoted as $J = |L + S|$. The 4f shells of the light REs are less than half-filled, while the heavy REs have more than half-filled 4f shells. As the orbital moment is always greater than the spin moment for the light RE

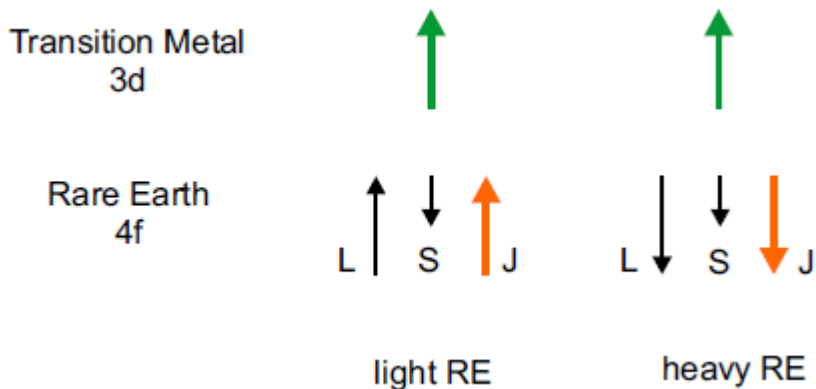


Fig. 3.1. Relative orientation of spin and orbital moments for alloys between transition metals (TM) and light and heavy rare earths (RE).

elements, the total moment is antiparallel to the spin moment based on the above statements. On the contrary, the total moment is parallel to the spin moment for HRE-TM. Because the 4f spin moment couples antiparallel to the TM moment (mediated through positive 4f-5d and negative 5d-3d exchange [12]) the total moment

on the RE couples parallel to the TM moment for the light REs and antiparallel for the heavy REs. The relative orientation between spin and orbital moments is schematically illustrated in Fig. 3.1.

However, in amorphous alloys, the actual situation is a bit more complicated than depicted in Fig.3.1. The different classes of magnetic structures (including ferromagnetic, sperimagnetic and speromagnetic structure) were found in amorphous RE-TM alloys [13].

The ferrimagnetic ordering leads to interesting dependences of the magnetization on composition and temperature for alloys between transition metals and heavy rare earths. Since the TM and the RE subnetworks are coupled (antiparallel) with each other, the net magnetization (M_s) may be very small or even zero known as magnetic compensation, where the magnetizations of RE and TM subnetworks are nearly

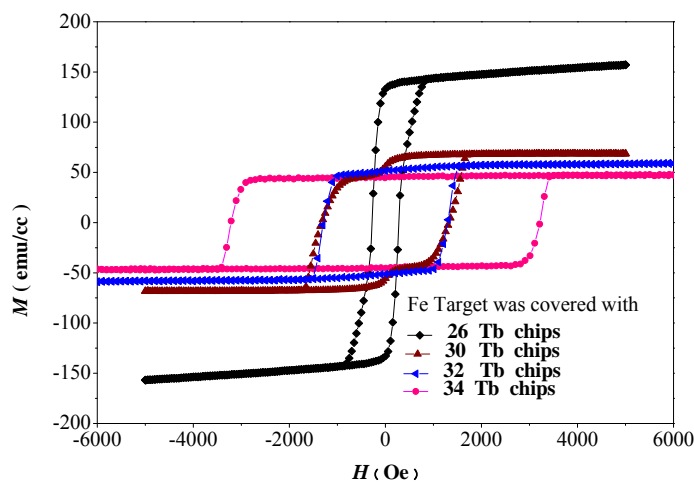


Fig. 3.2. The M-H loops for different composition TbFe alloys.

cancelled. In such compositions, low demagnetizing energy and perpendicularly magnetized films with the remanence ratio of one can be obtained. In MO recording, HRE and TM, whose composition is close to compensation composition, are usually used as recording media since they will be robust for external field application.

As RE and TM composition approaches the compensation point, extremely large external field must be applied to overcome energy barriers to reverse the magnetization, and the coercive force increases to infinity since the net magnetization M decreases to zero. This compositional dependence was also confirmed in our experiment. In order to vary the composition ratio in TbFe alloys, the number of Tb chips (5×5 mm) placed on Fe target more changed. Since the TbFe is easily oxidized, it was sandwiched by SiN layers (10 nm) to prevent the oxidation of the TbFe layer. The M - H loops for TbFe alloys with different composition were shown in Fig. 3.2. The increase of coercivity as well as the decrease of the magnetization was confirmed with the increase of Tb content. And the thickness dependence is also studied in this work, and was shown in Fig. 3.3. The magnetization is almost constant in the TbFe thickness range of 40-160 nm while the coercivity decreased with the increase of thickness. The coercivity of the RE-TM alloys strongly depends on their microstructure. The increase of the RE-TM thickness is considered to results in the decrease of the density of the magnetic wall pinning site.

The temperature profile of the spontaneous magnetization is one of the most important parameters for thermomagnetic writing scheme. Since the RE-TM alloys exhibit ferrimagnetic, the temperature dependence of the net magnetization is the difference from the temperature dependence of the RE and TM sub-network moments. As illustrated in Fig. 3.4, the magnetization of TM, M_{TM} , typically varies slightly until the temperature closes to the Curie temperature (T_C), while, the magnetization of RE,

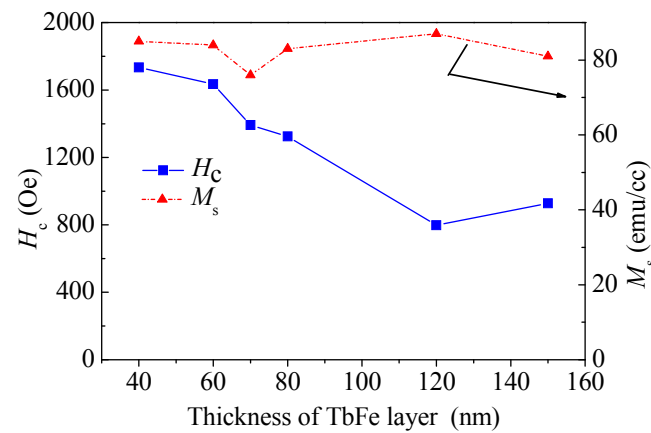


Fig. 3.3. Dependences of magnetic properties (H_c and M_s) on TbFe thickness.

M_{RE} , is more thermally sensitive than the M_{TM} [14]. At the compensation temperature (T_{comp}), the two subnetwork magnetizations are equal and opposite in direction, which causes the net magnetization to go to zero. And at T_{comp} the coercivity becomes nearly

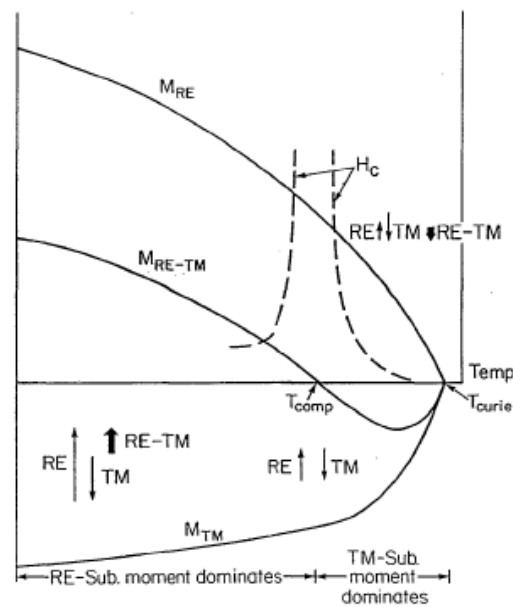


Fig. 3.4. The temperature dependences of the various magnetization components and of the coercive force for rare-earth transition-metal amorphous films.

infinite because of the zero magnetization. For further decrease of the temperature lower than the T_{comp} , the M_{RE} dominates the net magnetization. On the other hand, when the temperature is higher than the T_{comp} , the net magnetization points in the direction of the transition metal magnetization. The compensation temperature of RE-TM alloys is determined primarily by the ratio of rare earth to transition metal in the film, but independent of processing conditions [15]. Generally, the compensation temperature of TM-rich is lower than that of RE-rich for RE-TM alloys with same elements. At sufficiently high temperatures, thermal energy overcomes the exchange coupling and the ferrimagnetic behavior vanishes at the Curie temperature, T_{Curie} . The magnetization and coercive force go down to zero at the Curie temperature. The temperature dependence is usually analysed by using mean field approximation introducing exchange energies between TM and TM, $J_{\text{TM-TM}}$, RE and RM, $J_{\text{RE-TM}}$, and RE and RE, $J_{\text{RE-RE}}$ [16].

The Curie temperature, T_{Curie} , is primarily affected by the Co/Fe ratio in RE-FeCo films. When some Fe atoms are replaced with Co, the TM-TM interaction is dramatically enhanced, causing higher the Curie temperature [3]. For this reason, RE-Fe amorphous alloys, having low Curie temperature, are suitable for thermomagnetic recording. In contrast, RE-Co amorphous alloys, having high Curie temperatures, are very stable during a typical thermomagnetic writing. In RE-Fe binary alloys, the Curie temperature is much influenced by the kind of RE elements through the interaction between RE and TM atoms which is proportional to the magnitude of RE spin. The Curie temperature is the highest for GdFe with the largest RE spin, and it decreases in the order of TbFe, DyFe. Consequently, amorphous RE-TM system is considered to be the most suitable material for the thermo-magnetic writing because a

wide variety of temperature profiles can be easily obtained by adjusting Co and/or RE contents.

The temperature dependence of the coercivity was also investigated by experiment. The typical M - H loop of the $\text{Tb}_{20}\text{Fe}_{80}$ alloy film at room temperature was shown in Fig. 3.5. It can be seen that the films has large uniaxial magnetic anisotropy with the easy axis perpendicular to the film plane. It was also observed high squareness out-of-plane in the loop, and the magnetization and coercivity was about 80 emu/cm^3 , 1800 Oe , respectively. The temperature dependence of the coercivity for this film was measured by magneto-optical Kerr effect (MOKE) at various temperatures. The Kerr loops measured at different temperature are shown in Fig. 3.6. Both the saturated Kerr angle and the coercivity decreased with elevating the temperature. The coercivity of the film was about 2400 Oe at room temperature, and decreased to about 100 Oe when the temperature arrives at $90 \text{ }^\circ\text{C}$. The Kerr signal disappeared at a temperature of $120 \text{ }^\circ\text{C}$, and this temperature is generally considered as Curie temperature of the thin film. The

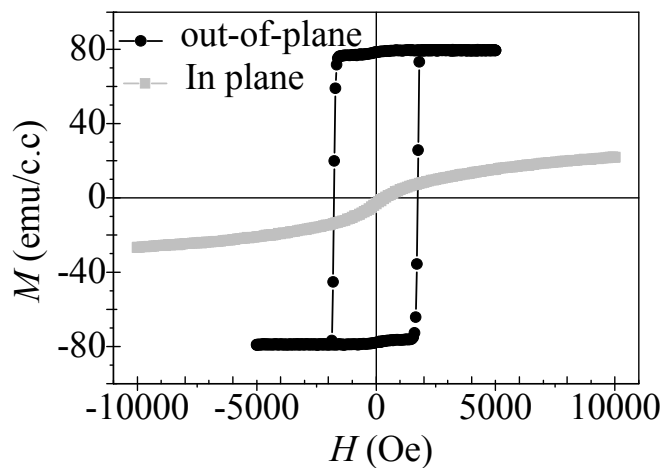
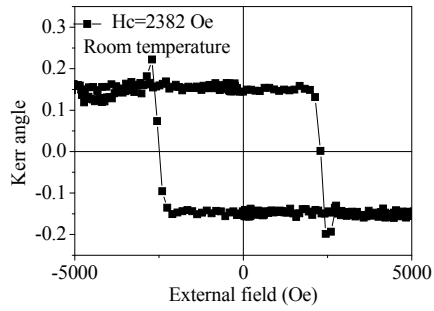
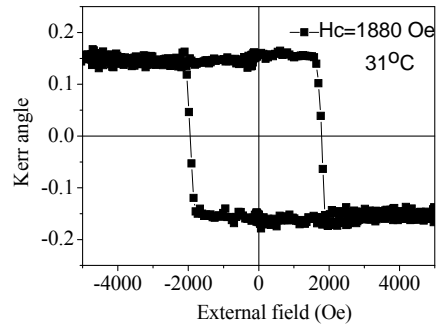


Fig. 3.5. M - H loop of certain TbFe films.

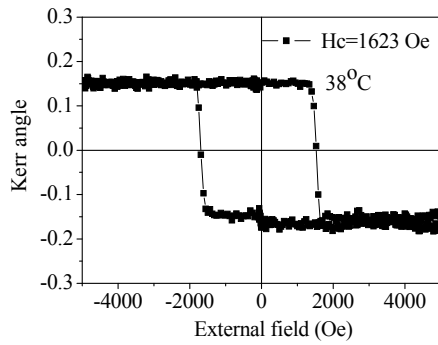
compensation temperature of this type TbFe alloys is below room temperature due to the fact the the film is TM-rich alloy, which is indicated from the polarity of Kerr rotation angle.



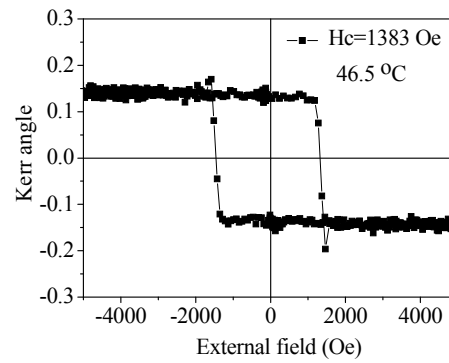
(a) Room temperature



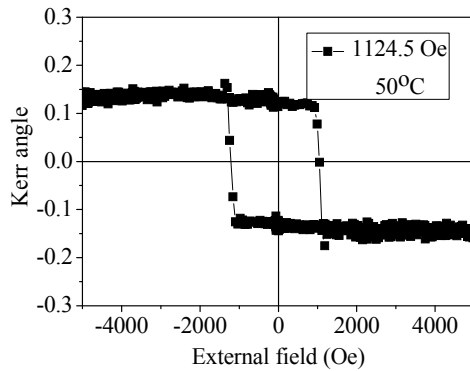
(b) 31 °C



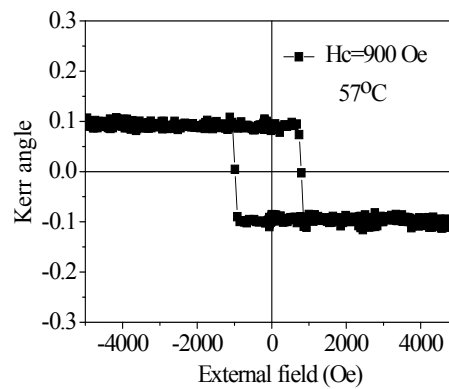
(c) 38 °C



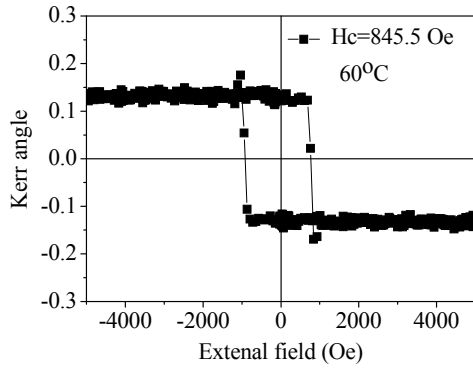
(d) 47 °C



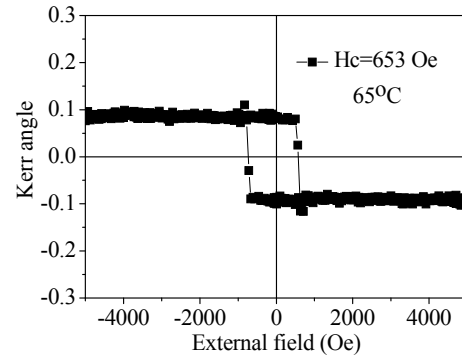
(e) 50 °C



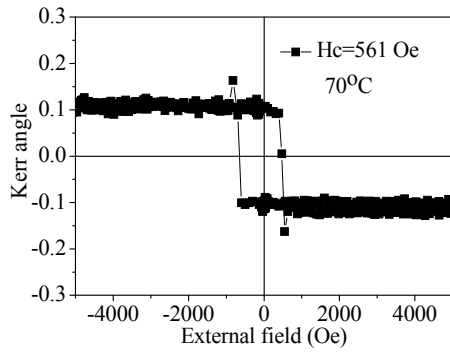
(f) 57 °C



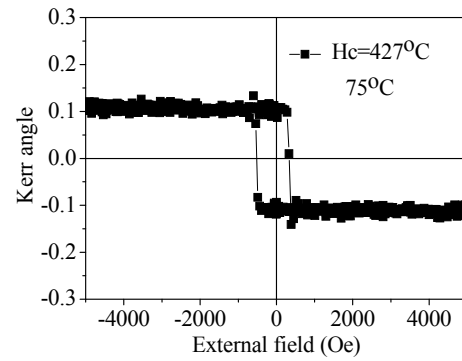
(g) 60 °C



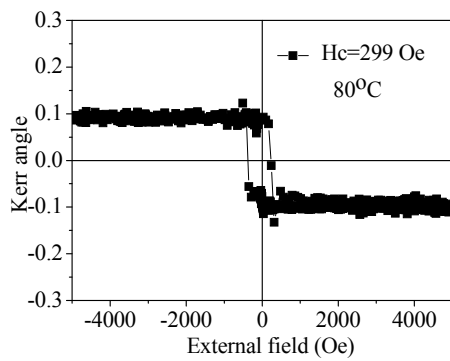
(h) 65 °C



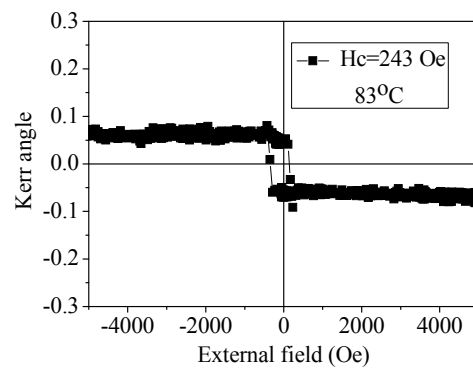
(i) 70 °C



(j) 75 °C



(k) 80 °C



(l) 83 °C

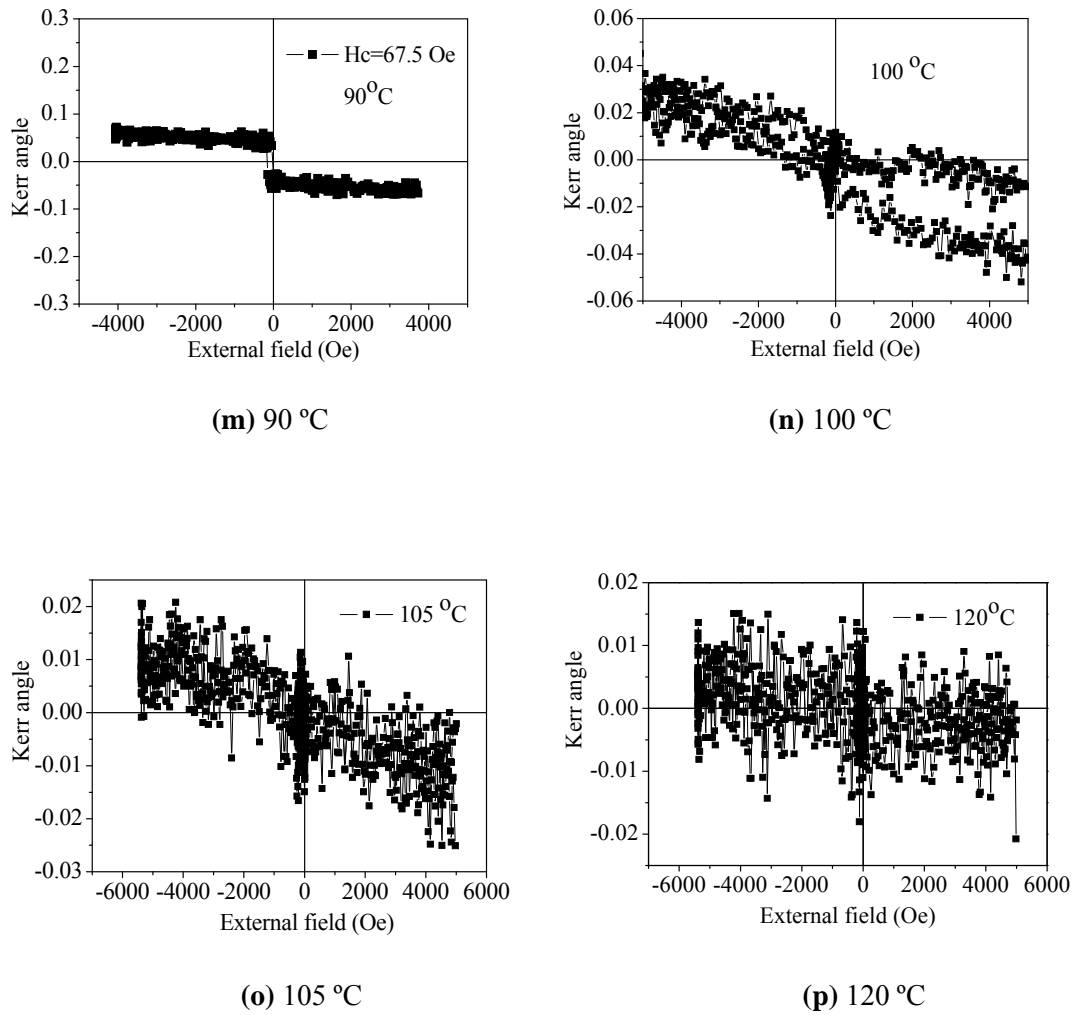


Fig. 3.6. Kerr loop from different temperature.

Similar to magnetization compensation at T_{comp} , RE-TM ferrimagnets can exhibit an angular compensation at a temperature T_A where the net angular momenta of the two subnetworks converge to zero, as shown in Fig. 3.7. The frequency of the homogeneous spin precession as well as the Gilbert damping parameter, are expected to diverge towards infinity at temperature T_A [17]. So that, RE-TM ferrimagnetic compounds are intriguing materials for the study of the ultrafast magnetization reversal, since the

combination of the large precessional frequency and damping constant would provide an ultrafast ringing-free magnetization reversal via precessional motion.

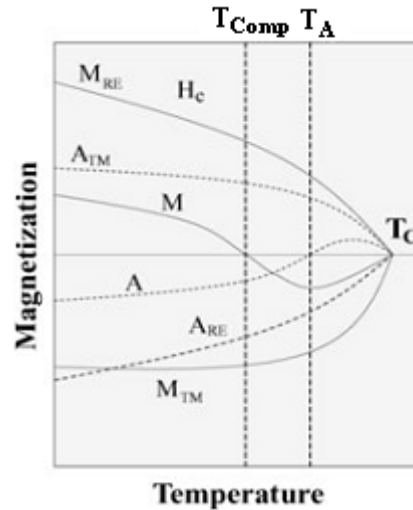


Fig. 3.7. Magnetization (M) and angular momentum (A) of the sublattices versus temperature.

3.3 Perpendicular magnetic anisotropy (PMA)

In amorphous materials, unlike their more common crystalline cousins, atoms are disordered in their relative placement to each other. As such, a magnetic property that is traditionally determined by crystalline order, such as the magnetic anisotropy that preferentially aligns the magnetization vector within a material, becomes very small. In the amorphous RE-TM alloys, however, magnetic anisotropy is often large and the magnetization spontaneously aligns perpendicular to the film plane. Since the rare earth atom's shape, determined by its valence charge cloud, is non-spherical (for Tb it is more football like), some form of local electrostatic anomaly had been proposed as the source of this property.

The origins of the perpendicular anisotropy, K_u , in RE-TM films are not well understood even though they are very critical to the performance of these films in magneto-optical recording or heat assisted magnetic recording. At least four different mechanisms have been proposed to explain the perpendicular anisotropy in RE-TM films. Pair-ordering [14,18], single-ion anisotropy [19,20], inverse magnetostriction [21,22], and shape effects caused by columnar growth [23,24] have all been discussed.

1. Pair-ordering anisotropy:

Magnetic anisotropy induced by pair-ordering originates from the differences, on an atomic scale, in the distribution of anisotropic atomic pairs between the directions parallel and perpendicular to the plane of the film. These differences in atomic pairs can result from resputtering during film growth.

2. Single-ion anisotropy

Non-S-state RE elements such as Tb and Dy have non-spherical 4f electron density distributions and non-zero orbital moments. The orbital moment is coupled with the spin moment, so called spin-orbital coupling, which ultimately ties to crystal lattice bridged by electrostatic interaction. Because of this bondage between spin and orbital moment, magnetization shows the direction behavior under the application of magnetic field (magnetic anisotropy). This anisotropy is given by the following equation [25],

$$K_u = 2\alpha_j J(J - \frac{1}{2}) A_2 \langle r^2 \rangle \quad (3.1)$$

Where A_2 is the uniaxial anisotropy of the crystal field around 4f electrons, α_j the Steven's factor, J the total angular momentum quantum number and $\langle r^2 \rangle$ the average of the square of the orbital radius of 4f electrons. The 4f electron cloud of pancake

(positive α_j) or cigar (negative α_j) like shape exhibits a magnetic anisotropy when it exists in anisotropic crystal fields.

3. Stress-induced anisotropy:

The perpendicular anisotropy can be introduced by the stress in the films or the substrate because of the inverse magnetostriction effect. The stress-induced anisotropy coefficient can be written as below:

$$K_\sigma = -(3/2)(\delta/l)\sigma \quad (3.2)$$

The δ/l and σ represent the linear strain of magnetostriction and planar stress, respectively. The large magnetostriction is directly related to the non-spherical 4f electron density distribution.

4. Shape anisotropy:

The columnar growth of the films can cause a magnetic anisotropy through shape effects. The demagnetizing field H_d in a magnetic thin film arises from dipole-dipole interaction. The shape anisotropy constant can be represented by the following equation,

$$K_s = (1/2)(N_x - N_z)M^2 \quad (3.3)$$

where N_x and N_z are demagnetizing factors along x - and z -axes of the column in the film.

3.4 Chemical Stability

Amorphous rare-earth transition metal films have been regarded as very promising materials for various applications. However, these materials exhibit some intrinsic problems in resisting corrosion and oxidation. This can be accomplished by means of a protective layer coating, or by improving the RE-TM film itself. To some extent the susceptibility of a given film to oxidation is structure-dependent and it is now known

that films that are dense, with no pin-holes or voids, deteriorate much more slowly. This is probably because any oxidation can only occur at the film surface, whereas films with many voids or similar open structures are clearly very likely to undergo a bulk oxidation reaction. From this point of view, one way to improve the film stability is to consider the deposition conditions and method of production. The majority of investigations have attempted to reduce the progressive oxidation of the medium by the use of protective 'passivation' layers. Commonly, the media today are made with a dielectric such as AlN or Si₃N₄, which is impervious to water vapor and oxygen between the polycarbonate or glass substrate and the RE-TM film. The RE-TM film is then coated with a similar dielectric and a thick overcoat to protect it from the environment. Investigations have shown that a coating and underlayer Si₃N₄/AlN do not influence the magnetic properties and the thermal stability [26]. Alternatively, the introduction of additional elements to the RE-TM alloy has proved beneficial. That corrosion resistance could be improved markedly by the addition of an active metal that tends to form passivated layers such as Be [27], In [28, 29], Al, Cr, [30] or Ti [31] to the TbFe film. In this research, TbFe was sandwiched by SiN which protects the thin film from contamination from substrate and environment. However, we should pay special attention to the oxidation at the sidewall of the patterned TbFe film, although we didn't find any trace of oxidation from the hall effect measurement of the patterned films [32].

3.5 Rare earth–transition metal alloys in tunneling structures

3.5.1 Spin polarization of RE-TM alloys

The spin–dependent transport properties of ferromagnetic transition metal alloys with paramagnetic 3d, 4d and 5d elements have been studied for many years, since the material properties (e.g. saturation magnetization, coercivity, and magnetic anisotropy) can be tailored by alloying Co, Fe, and Ni with other ferromagnetic or non–magnetic elements, and the spin-polarization of their alloys can significantly exceed that of pure transition metal ($\text{Co}_{70}\text{Fe}_{30}$ is typically used in the ferromagnetic layers of the MTJ electrodes since its spin-polarization significantly exceeds the polarization of Co or Fe metal [33]). According to Julliere’s model, the TMR value is determined by the spin polarization of the ferromagnetic layers. That is, the higher tunneling spin polarization (TSP) of the ferromagnetic layers leads to the larger TMR. Therefore, it is crucial and basic to investigate the spin polarization of materials. The TSP of a given FM/barrier combination can be measured using superconducting tunneling spectroscopy. All materials of this type under investigation have so far been measured to be positively spin polarized with the exception of magnetite (Fe_3O_4) [34] and SrRuO_3 [35]. The nature of spin dependent tunneling was also gradually understood with further study of the spin polarization of the materials. Recently, much attention has been focused on alloys of Co, Fe and Ni with the ferromagnetic 4f elements (rare earth – transition metal alloys) for spin dependent tunneling application, due to they display various unique properties such as ferrimagnetic ordering, amorphous structures and perpendicular magnetic anisotropy in thin films as described above. The spin polarization for RE-TM

alloys are very different from that for alloys of Co, Fe and Ni with paramagnetic transition metals. The sign of TSP for RE-TM is reversed if the orientation of the RE and TM moments with respect to the applied field is varied. Therefore, its sign can be reversed around compensation composition and compensation temperature. It proves that even in the case of vanishing net moment the tunneling electrons can be sizably polarized due to the fact that the tunneling matrix elements for tunneling from different atoms are different and their relative polarization is different. This reinforces the view that a spin polarized tunneling current can be created from a material that does not possess an overall spin imbalance. The results suggest that it should be possible to find materials with high polarization which have no net moment. The temperature and composition dependence of TMR for MTJs using RE-TM layers shows some striking and unique features. Moreover, the Curie temperature and coercivity of the free layer and pinned layer can be tuned over a wide range. While these are fascinating properties that has not been yet observed in other MTJ systems, there are some disadvantages which would likely prevent the use of these materials in applications such as MRAM: these drawbacks include especially their poor chemical stability since RE element is more likely to form oxygen bonds at the interface with the barrier to get partially oxidized, thus being driven magnetically inactive. Low room temperature TSP values are an other challenge. These values (list in table 3.1 [13]) are low compared to conventional MTJs with two Co-Fe layers. So it is necessary to create a method to increase both TMR values and chemical stability of MTJs using RE-TM alloys. To address the above issue, it is simple and feasible way to insert interlayer with high spin polarization between the barrier and RE-TM layer. The concept here is that a highly spin polarized thin interlayer will create a highly spin polarized tunneling current.

Moreover, the insertion of a Co-Fe interlayer can also prevent the RE atoms from reacting with the oxygen in the barrier and improves the chemical stability of these junctions so much.

The material of choice for this interlayer of this study is CoFe as it shows the high spin polarization of the transition metals alloys [36].

Table 3.1. TSP values for some Fe-Tb and Co-Tb alloys.

Material	TSP
Co ₈₀ Tb ₂₀	+27%
Co ₇₅ Tb ₂₅	-13%
Co ₅₈ Tb ₄₂	-15%
Co ₂₀ Tb ₈₀	+1%
Fe ₉₂ Tb ₈	+25%
Fe ₅₈ Tb ₄₂	-11%
Fe ₄₀ Tb ₆₀	-4%
Fe ₂₀ Tb ₈₀	+3%
Tb	+2.5%

3.5.2 Process of MTJ

The TMR devices with the electrodes and tunnel barrier are deposited as follows; the first electrode is sputter deposited on the top of Si/SiO₂ followed by a very thin aluminum film, which is oxidized using plasma oxidation methods. Finally the top electrode is sputter deposited on the top of the aluminum oxide. The junction is defined using optical lithography with different size areas. The junction is surrounded by AlO_x in order to insulate the top and the bottom electrodes, followed by depositing an Al film on the top of the junction as contact pads to measure the tunnel current. Therefore, for the fabrication of the MTJ devices a combined deposition and patterning process was utilized, including sputter deposition, etching, and optical lithography. The crucial point

of the fabrication of the tunneling junctions is the barrier. It needs to be of homogenous thickness, pinhole free, and is usually only 1 to 2 nm thin to allow a sufficiently high tunneling current. Instead of direct deposition of the insulating barrier material, experience has shown that deposition of a metal and subsequent oxidation yield the best results. The cause of this behavior is the wetting effect of aluminium on several transition metals which leads to a decreased roughness of a thin film stack after aluminium is deposited. For the oxidation of the tunneling barrier an optimized process has to be developed.

3.5.2.1 Magnetic tunnel junction architecture

The MTJ structure cannot be described, as being a simple structure of two ferromagnetic electrodes separated by a thin insulating barrier. Both electrodes are in reality comprised of several layers each with it's own objective, some of them were already addressed. In principle this structure could be made to work for a memory if the coercivity of one of the layers, a “reference” layer, is much higher than that of the other, or is set via exchange coupling. The typical architecture is shown in Fig. 3.8.

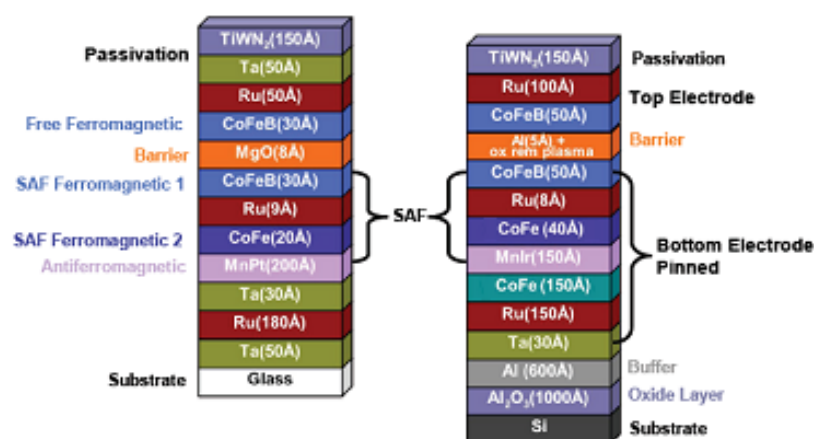


Fig. 3.8. Typical longitudinal MTJ structure.

Apart from the evident role of the insulating layer, to provide the tunneling barrier, the other layers can be divided in the following groups. The main purpose of the buffer layer is providing a smooth interface and a low resistance contact to the junction. The ferromagnetic layer at each side of the barrier provides the electron spin polarization on the base of the spin dependent tunneling effect. Since the tunnel junction signal also depends on the relative magnetization directions of the ferromagnetic layers, the antiferromagnetic layer and the Synthetic Anti-Ferromagnetic (SAF) layers used have the purpose of keeping the magnetization direction of the ferromagnetic layer fixed via exchange-coupling, to set the reference direction and its magnetization should only rotate for fields much higher than the reversal fields of the free layer. The capping layer is used to protect the full structure from all the chemicals used in processing and oxidation in ambient atmosphere.

3.5.2.2 Film (stack) deposition

The MTJ stack of Ta(5)/TbFe(x)/CoFeB(t)/AlO(1.6)/CoFeB(t)/TbFe(x)/Ta (5) (the unit is nm) for MTJ stack was deposited onto a Si/SiO₂ substrate. TbFe layers were deposited by co-sputtered of Tb and Fe. Oxide barriers were fabricated by plasma oxidization of the metal Al oxidation, and it is discussed in detail later. In order to obtain the different coercivities from the two TbFe layer, the composition of TbFe was varied by controlling the sputtering power of Tb target keeping the power applied to Fe target constant. The two TbFe layer with high and low coercivities act as a pinned and a free layer, respectively. The sputtering condition is listed in Table 3.2

The most challenging step in the MTJ stack deposition is the fabrication of the insulating barrier. The barrier is required to be continuous and without pinholes at thicknesses below 20 Å, to ensure the tunneling current conduction through the barrier.

It must be a non-magnetic oxide to prevent spin flips events in the tunneling process and form a stable oxide that preserves the integrity of the ferromagnetic electrodes.

Table 3.2. Sputtering condition for multilayer films.

Target	Power (W)	Ar(O ₂) pressure (Pa)
Ta	80	0.4
TbFe	17~26 (Tb)/120(Fe)	0.4
CoFeB	120	0.4
Al	120	0.4
Al ₂ O ₃	200	(O ₂) 4.0
CoFeB	120	0.4
TbFe	17~26 (Tb)/120 (Fe)	0.4
Ta	80	0.4

Deposition is also performed during the fabrication process of the tunnel junctions, for instance, the deposition of oxide aluminum to isolate the bottom from the top electrode and the deposition of aluminum for the top contact.

3.5.2.3 Oxidation processes

The tunneling junctions fabricated for this work always have aluminium-oxide (AlO_x) as tunneling barrier. The fabrication of this oxide was achieved by the depositing 1.6 nm of metallic aluminium followed by oxidization of the metal, which is 200 Watt RF plasma generation on the faced Al₂O₃ target at a oxygen pressure of 4 Pa.

Since the barrier resistivity is exponentially dependent on its thickness, the biggest part of current will flow through the thinnest parts (“hot spots”) of a rough barrier.

Since this will lead to higher thermal stress in these hot spots, a break-down of the barrier becomes more likely which makes it necessary to produce barriers as smooth as possible.

The parameters of the oxidation process must also be tuned so that there is neither over- nor under-oxidation. If there is an amount of unoxidized Al left at the interface between the ferromagnetic electrode and the barrier, the paramagnetic aluminium will lead to an increase of the spin-flip and a decrease of the TMR value of the magnetic tunneling junction. The oxidation process also affects the ferromagnetic electrode, and various metal oxidation may be formed. Some of these exhibit antiferromagnetic behavior which also leads to a strongly reduced spin conservation and thus a reduced TMR value. In this study, RE oxides were easily formed at the interface between the ferromagnetic electrode and the barrier due to the chemical instability of RE elements. sensitive to plasma oxidation. When the Al layer was oxidized for 60 sec, the over-oxidation wasn't observed from the measurement of the M-H loop of the MTJ stack, and RA and TMR were not increased significantly with further increase of oxidation time from 60 sec for longitudinal MTJ comprised of CoFe(B) [37]. Therefore, the 60 sec is optimum time for plasma oxidizing 1.6 nm Al layer when inserting the CoFe(B) ferromagnetic electrode between RE-TM layers and barrier layer.

3.5.2.4 Process steps

Photolithography pattern transfer technique

For transport measurements, a deposited tunneling multilayer has to be structured laterally. Shadow mask technologies which utilize masks on top of substrates during the deposition don't allow small enough feature sizes. Therefore, in this study optical lithography and ECR ion etching was employed. We have already discussed these

microfabrication techniques in chapter 2. The detail condition of the lithography process used here is resumed in the following:

- 1) Samples were cleaned in an ultrasonic bath using acetone and isopropyl alcohol (IPA) for 5 min, respectively. Then the samples were dried on the hot plate at 170 °C for 2 minutes for dehydration.
- 2) The HMDS primer was spin-coated with 500 rpm for 5 seconds, and with 4000 rpm for 30 seconds in spin coater (KYOWA RIKEN K-359 S-1). After spin coating of HMDS, a baking was performed in a convectional oven at 75 °C for 15 minutes.
- 3) The positive resist of SHIPLEY (S1813) was spin-coated with 1000 rpm for 10 seconds, and with 5000 rpm for 35 seconds.
- 4) Soft baking of The photo-resist was pre-baked at 110°C for 10 minutes in the convectional oven.
- 5) Resist layer on the TbFe film was exposed to the mixed light of g-line (436 nm), h-line (405 nm) and i-line (365 nm) offered by high pressure Hg lamp using mask alignment (Canon PLA502F). The light power is 250W and exposure time is determined depending on the exposure area (typically 5 sec. ~ 13sec.).
- 6) Post exposure bake (PEB) was carried out at 90 °C for 20min.
- 7) The sample was developed in SHIPLEY MF CD-26 DEVELOPER. The sample was soaked for 15 sec and agitated for 45 sec. in developer. And followed by puddling in pure water for 1 minute.

After the patterning of the photoresist layer, an etching process was employed to transfer the pattern of the photoresist to the thin film. The etching was carried out in ECR etching system, and etching condition is listed in Table 3.3. Finally, the photoresist

was stripped by MICROPOSIT REMOVER 1165 for 10 min twice in an ultrasonic bath at 80 °C, and then rinsed in IPA for 5 min.

Table 3.3. Etching conditions

Base pressure	$< 2.0 \times 10^{-6}$ Pa
Ar pressure	1.2×10^{-2} Pa
Input/reflect power	110 / < 10 W
Accelerate/extraction voltage	600V/-100 V

Step 1. Bottom electrode definition

The first step in the lithographic tunnel junction fabrication is the definition of the bottom electrode.

Step 1.1 - The photoresist is patterned to cover the bottom electrode lead and contact areas. The side view in Fig. 3.9, shows the photoresist protected area during the etching

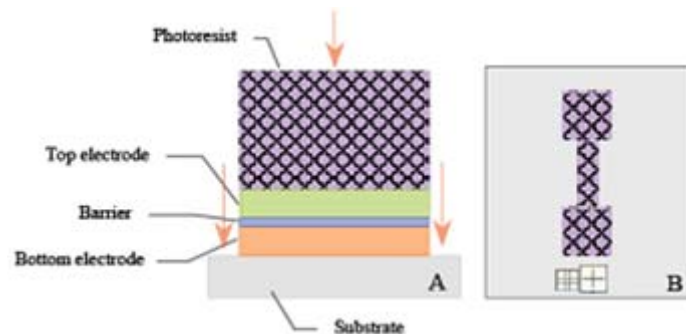


Fig. 3.9. MTJ structure after the first etching that defines the bottom electrode. **A** – Side view; **B** –Top view.

process. The top view illustrates the shape of the electrodes where the junction will be defined at the center and the two large contact pads are seen. The alignment marks (+)

are simultaneously fabricated for the adjustment of the masks of junction area and top electrode definitions.

Step 1.2 - The material uncovered by the photoresist pattern was etched away by ECR Ar⁺ ion beam milling. It has to be etched until the oxide layer above the silicon substrate.

Step 1.3 – the resist was strip with a hot remover (photoresist solvent MICROPOSIT REMOVER 1165).

Step 2. Junction area definition

The second step is to define the junction geometry and area. This is the most crucial and sensitive step in all the junction fabrication processes.

Step 2.1 - The photoresist is patterned to cover a small area around the center on the bottom lead and also at the part of bottom lead and large bottom contact areas. In this lithography step, the time for exposure was set to 4.5 sec~ 6 sec, a little bit shorter than the one used for the bottom lead, because the dimensions required are much smaller.

Step 2.2 - The unprotected material was etched by ECR. Since the bottom electrode serves as a contact layer between the contact pad and the junction, the etching must be stopped before the bottom electrode material is completely removed. Typically, the etching was stopped just after the tunnel barrier was removed, which can be detected from the SIMS signal. The side view of the sample just after the etching is shown below.

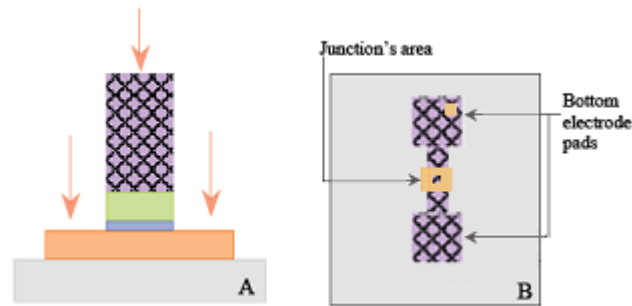


Fig. 3.10. **A** – Side view after 2nd etch; **B** -Top view after 2nd etch.

Step 3. Insulating layer deposition

In this step, an insulating layer Al_2O_3 covered to avoid the shortcut between top and bottom electrodes and also forces the current to pass through the barrier perpendicular to the film plane. Normally, 200 nm thick Al_2O_3 layer was deposited by 5-target sputtering system.

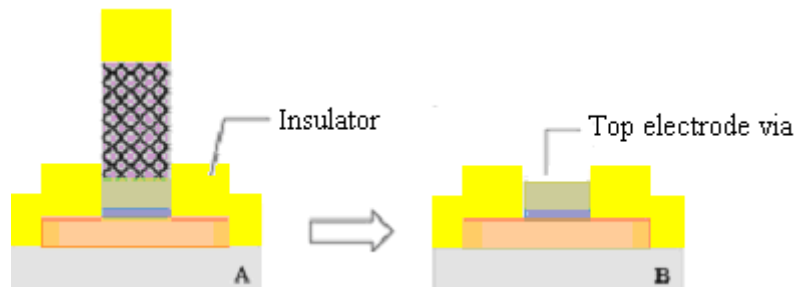


Fig. 3.11. Side view of the junction area. **A** - After insulating passivation layer deposition; **B** - After liftoff and opening the contact to the junction area and pads.

After the deposition of Al_2O_3 layer, the photoresist was removed. This liftoff process opens a via in the insulating layer as a contact hole between the top electrode and junction.

Step 4. Top electrode deposition

After the liftoff of the Al_2O_3 insulating layer, the via to the junction area was opened.

The next step provides the lead and contact pads for the top electrode.

Step 4.1- The photoresist is patterned to cover the sample, except for the top lead and the large contact pad areas, as shown in Fig. 3.12.

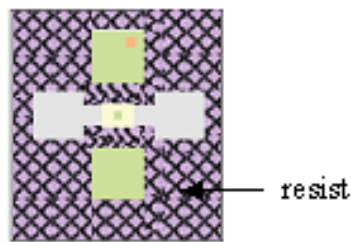


Fig. 3.12. Top view of the sample after the photoresist patterning.

Step 4.2 - Al with 200 nm thickness was deposited by 5-target sputtering system.

Step 4.3 – Part of Al layer was Lifted-off with hot Microstrip (photoresist solvent) in the ultrasonic bath. The sample was rinsed by IPA for 5 min in ultrasonic bath. The Al metal is removed from the sample, except for the uncovered area (top lead and the large contact pad areas). The final view of the fabricated sample are illustrated in Fig. 3.13.

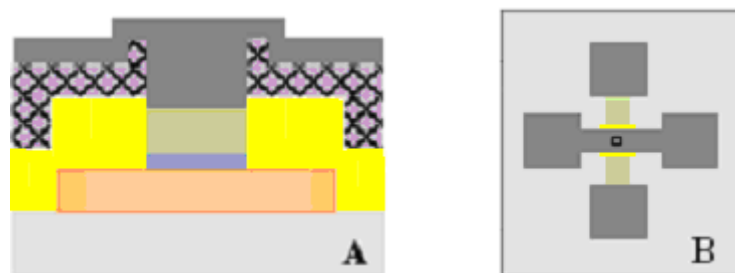


Fig. 3.13. **A** - Cross-sectional view of the junction sandwiched between top and bottom electrodes. **B** - Top view of the sample after the Al lift-off.

3.5.2.5 Discussion of MTJ

Magnetic properties can be characterized for plain MTJ stacks, using the AGM, which is especially useful to interpret magneto-transport measurements. It provides information on the exchange coupling between TbFe with perpendicular anisotropy and $\text{Co}_{90}\text{Fe}_{10}$ or $(\text{Co}_{90}\text{Fe}_{10})_{92}\text{B}_8$ with longitudinal anisotropy, and the coercive fields of the free and pin layers.

After the fabrication, the tunnel junctions are ready to be characterized for their electrical properties. For the transport measurement, resistance of the tunnel junction depending on a magnetic field and on an applied current were recorded. TMR loops and I-V curves in the patterned element are obtained from these measurements.

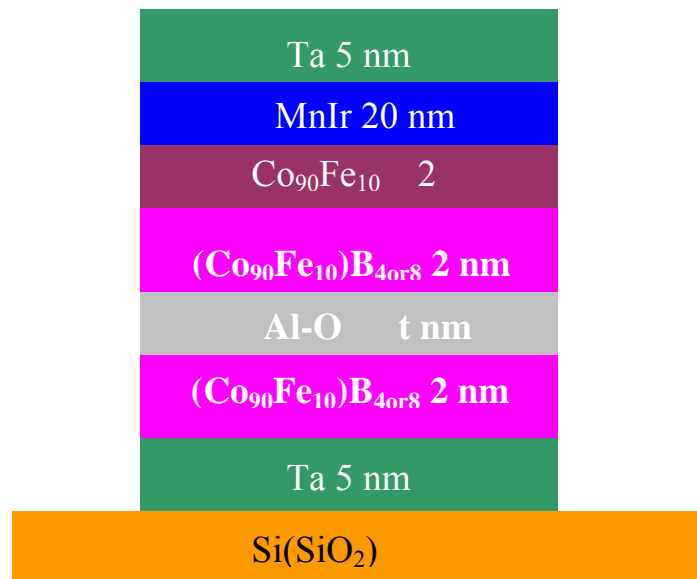


Fig. 3.14. Longitudinal MTJ stack studied preliminarily.

Before preparing the perpendicular MTJ (p-MTJ) using TbFe layers, the other research team of our laboratory studied standard longitudinal MTJ (the structure is shown in Fig. 3.14) to get a better insight of the preparations of the tunneling barrier

and electrodes. In the study of standard longitudinal MTJ, the deposition parameters and process conditions were optimized to obtain the best transport properties. For the optimum conditions, high TMR ratio of ~50% has been achieved [37].

3.5.2.5.1 Effect of plasma oxidation on RE-TM layer

In this perpendicular MTJ fabrication, the simple structure perpendicular MTJ was studied at first (see Fig. 3.15). By controlling the sputter power of Tb target (the 23 W and 17 W for $Tb_{17}Fe_{83}$ and $Tb_{13}Fe_{87}$, respectively) keeping the power of Fe target constant of 120 W, TbFe alloys with different composition can be achieved and considered as pin and free layers.

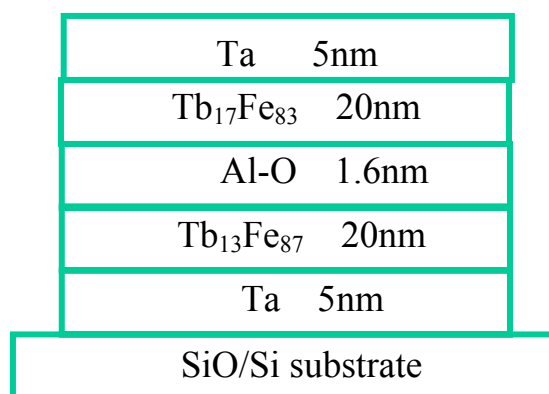


Fig. 3.15. The simple structure p-MTJ without CoFe layer

The samples were exposed to exactly the same oxidation process, which is 200 Watt RF plasma generation on the faced Al_2O_3 target at a oxygen pressure of 4 Pa. The $M-H$ loops of the MTJ having the barrier layer oxidized for 0 s, 60 s, 45 s, are shown in Fig. 3.16. Two steps magnetization reversal process can be clearly observed from the stack without oxidation of Al, however, this two steps become unclear with increasing

oxidation time of Al. This may be associated with the oxidation of the TbFe layers during the plasma oxidation process.

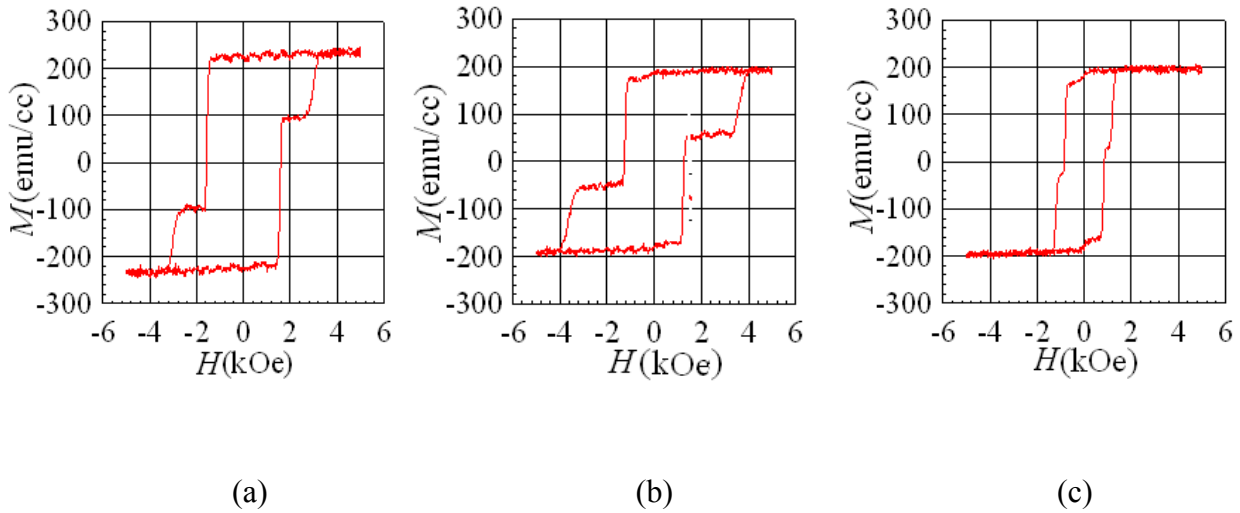


Fig. 3.16. M - H loops for MTJ stacks with Al oxidation time of (a) 0 s; (b) 45 s; (c) 60s.

3.5.2.5.2 P-MTJ with inserting CoFe(B) layer

In order to prevent the RE-TM layer from oxidation, $\text{Co}_{90}\text{Fe}_{10}$ layers were inserted between the barrier layer and TbFe layers, as seen in Fig. 3.17. M - H loop measurements show that the magnetic properties of the stacks are not affected by the oxidation of the barrier, and the stack always exhibited the M - H loop as shown in Fig. 3.18. The presence of $\text{Co}_{90}\text{Fe}_{10}$ layer in this case 1 nm thickness, affects the squariness. The exchange coupling between low coercivity $\text{Tb}_{13}\text{Fe}_{87}$ and $\text{Co}_{90}\text{Fe}_{10}$ seems to be insufficient which results in gradual increase of the magnetization in the range of H from 0 to 7 kOe.



Fig. 3.17. The structure of p-MTJ with inserting CoFe layer.

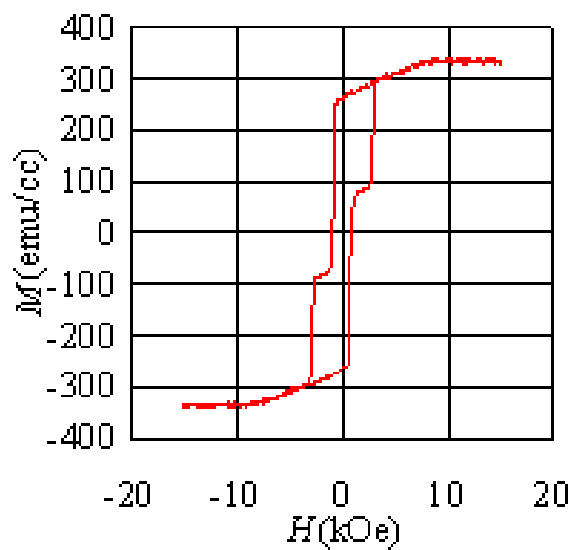


Fig. 3.18. M - H loop of stacks with inserting 1nm CoFe layer.

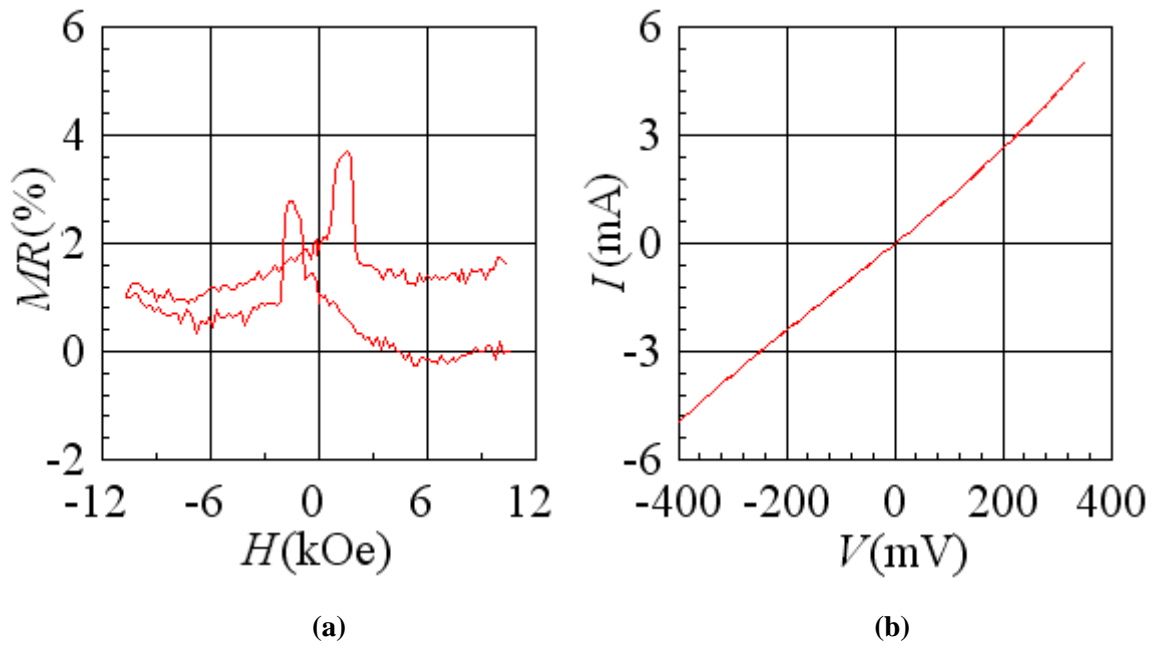


Fig. 3.19. (a) MR and (b) I - V curves for the $15 \times 15 \mu\text{m}^2$ sample.

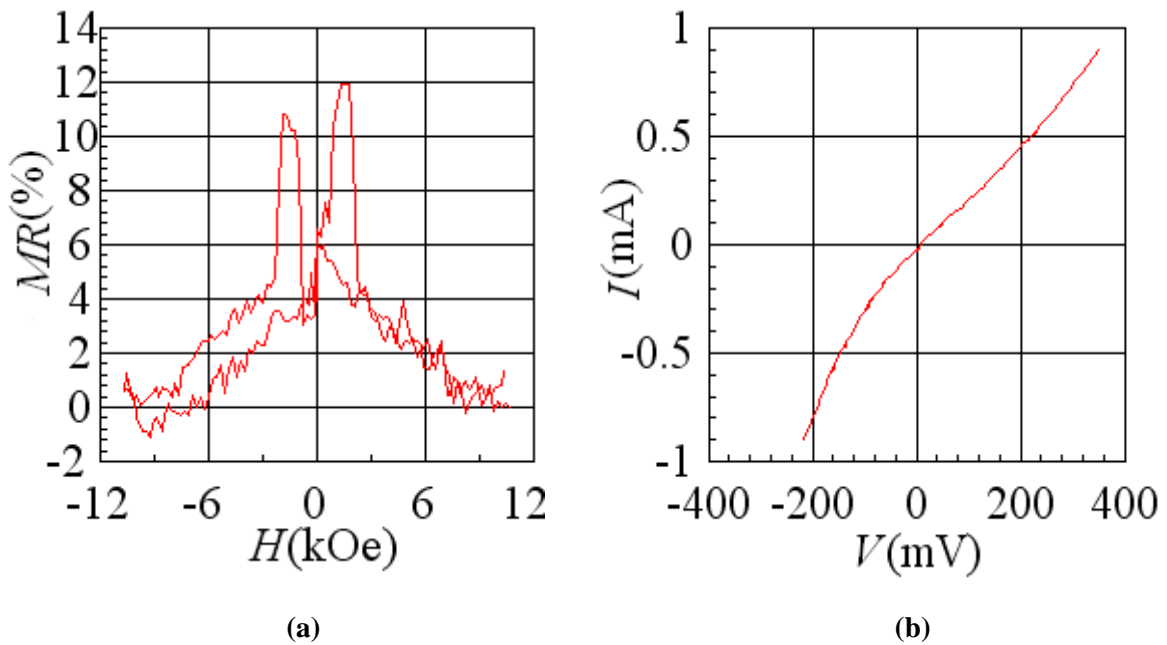


Fig. 3.20. (a) MR and (b) I - V measured for the $10 \times 10 \mu\text{m}^2$ sample.

Figures 3.19 and 3.20 show (a) MR loops and (b) I-V curves obtained for microfabricated MTJs with $10 \times 10 \mu\text{m}^2$ and $15 \times 15 \mu\text{m}^2$ junction sizes, respectively [38]. The MTJ with $10 \times 10 \mu\text{m}^2$ exhibited small MR ratio of $\sim 3\%$ and almost linear I-V curve, which indicates that there exist some defects in or peripheral of the barrier layer. On the other hand, the MTJ with $15 \times 15 \mu\text{m}^2$ showed rather high TMR ratio of $\sim 12\%$, and non-linear I-V curve which is typical in tunneling junctions. However, the gradual increase of the TMR in the range of H from 0 to 7 kOe and asymmetric $I-V$ characteristics are considered to be the results of the insufficient exchange coupling between the low coercive TbFe and CoFe and partial oxidization of CoFe or TbFe layer, respectively. These should be removed by optimizing the thickness of the layer structure, oxidization condition, and photolithography process.

3.6 Conclusion

In this chapter, magnetic properties of RE-TM alloys in particular TbFe was investigated. Their spin dependent tunneling was studied by fabricating p-MTJ having TbFe using lithography technique. These alloys have various unique properties for thermomagnetic writing, such as high perpendicular anisotropy, tunable Curie temperature and coercivity. The magnetic properties are also sensitive to the ferrimagnetic ordering of the RE and TM moments, which can be adjusted by the composition of the alloys. However, the poor chemical stability and low room temperature TSP values of RE-TM alloys would likely prevent them from application in the MTJ. To address the above issue, it is simple and feasible way to insert CoFe interlayer with high spin polarization between the barrier and RE-TM layer. A highly spin polarized thin interlayer will create a highly spin polarized tunneling current.

Moreover, the insertion of a CoFe interlayer can also improve the chemical stability of these junctions so much. The two TbFe layer with high and low coercivities act as a pinned and a free layer, respectively. Using a CoFe interlayer between TbFe layer and Al₂O₃ barrier, a TMR around 12% can be achieved at room temperature. The TMR is expected to be improved by optimizing the multilayer thickness, oxidization process, and photolithography process. The potential of high TMR, as well as the tunable coercivity was shown in this Chapter, which makes RE-TM alloys as promising candidates for thermally assisted MRAM.

References

- [1] P. Chaudhari, J.J. Cuomo, and R.J. Gambino, *Appl. Phys. Lett.*, **22** (1973) 337.
- [2] R.J. Gambino. Rare earth-transition metal amorphous alloy media. In R. J. Gambino and T. Suzuki, editors, *Magneto-Optical recording Materials*. IEEE Press, 2000.
- [3] S. Tsunashima, *J. Phys. D: Appl. Phys.*, **34** (2001) R87.
- [4] A.E. Clark and H. Belson, *Phys. Rev. B*, **5** (1972) 3642.
- [5] N.C. Koon and A. Schindler, F. Carter, *Phys. Lett. A*, **37** (1971) 413.
- [6] J. Shih, T. Chin, Z. Sun, H. Zhang, and B. Shen, *IEEE. Trans. Magn.*, **37** (2001) 2681.
- [7] J. J. M. Ruigrok, R. Coehoorn, S. R. Cumpson, and H. W. Kesteren, *J. Appl. Phys.*, **87** (2000) 5398.
- [8] H. Saga, H. Nemoto, H. Sakeda, and M. Takahashi, *Jpn. J. Appl. Phys.*, **38** (1999) 1839.
- [9] T. Ikeda and S. Tsunashima, *J. Magn. Soc. Jpn.*, **24** (2000) 563 (in Japanese).
- [10] N. Nishimura, T. Hirai, A. Koganei, T. Ikeda, K. Okano, Y. Sekiguchi, and Y. Osada, *J. Appl. Phys.*, **91** (2002) 5246.
- [11] T. Ikeda, M. Onoe, S. Tsunashima, *J. Magn. Soc. Jpn.*, **3** (2003) 109.
- [12] I. A. Campbell, *J. Phys. F*, **2** (1972) L47.
- [13] Novel materials for magnetic tunnel junctions, Christian Kaiser, Ph.D Dissertation, RWTH Aachen University, Germany, 2004.
- [14] G. S. Cargill, and T. Mizogouchi, *J. Appl. Phys.*, **49** (1978) 1753.
- [15] M. H. Kryder, *Annu. Rev. Mater. Sci.*, **23** (1993) 411.
- [16] R. Hasegawa, B. E. Argyle, and L. J. Tao, *AIP Conf. Proc.* **24** (1975) 110.
- [17] R. K. Wangsness, *Phys. Rev.*, **91** (1953) 1085.

- [18] R. J. Gambino and J. J. Cuomo, *J. Vat. Sci. Technol.*, **15** (1978) 296.
- [19] T. Egami, C. D. Graham, Jr., W. Dmowski, P. Zhou, and P. J. Flanders, *IEEE Trans. Magn.*, **23** (1987) 2269.
- [20] Y. Suzuki, S. Takayama, P. Kirino, and N. Ohta, *IEEE Trans. Magn.*, **23** (1987) 2275.
- [21] S. Tsunashima, H. Takagi, K. Kamegaki, T. Fujii, and S. Uchiyama, *IEEE Trans. Magn.*, **14** (1978) 844.
- [22] H. Takagi, S. Tsunashima, and S. Uchiyama, *J. Appl. Phys.*, **50** (1979) 1642.
- [23] M. Ohkoshi, M. Harada, T. Tokunaga, S. Honda, and T. Kusuda, *IEEE Trans. Magn.*, **21** (1985) 1635.
- [24] H. J. Leamy and A. G. Dirks, *J. Appl. Phys.*, **50** (1979) 2871.
- [25] J. J. Rhyne: Bulk Magnetic Properties. In *Magnetic Properties of Rare Earth Metals*. (edited by R. J. Elliott), pp. 156. Plenum Press, London, New York (1972).
- [26] S. Hashimoto, Y. Ochiai, M. Kaneko, K. Watanada and K. Aso, *IEEE Trans. Magn.*, **23** (1987) 2278.
- [27] R. Carey, D. M. Newman, and B. W. J. Thomas, *J. Phys. D: Appl. Phys.*, **28** (1995) 2207.
- [28] T. Iijima and I. Hatakeyama, *IEEE Trans. Magn.*, **23** (1987) 2626.
- [29] T. Iijima, *Appl. Phys. Lett.*, **50** (1987) 1835.
- [30] M. Kobayashi, M. Asano, K. Kawamura, and S. Ohno, *IEEE Trans. J. Magn. Jpn.* **TJMJ-1** (1985) 527.
- [31] M. Kobayashi, M. Asano, Y. Maeno, K. Oishi, and K. Kawamura, *Appl. Phys. Lett.*, **50** (1987) 1694.
- [32] T. Masubuchi, Master Dissertation, Nagoya University, 2005 (in Japanese).
- [33] D. J. Monsma and S. S. P. Parkin, *Appl. Phys. Lett.*, **77** (2000) 883.
- [34] G. Hu and Y. Suzuki, *Phys. Rev. Lett.*, **89** (2002) 276601
- [35] D. C. Worledge and T. H. Geballe, *Phys. Rev. Lett.*, **85** (2000) 5182.
- [36] D. J. Monsma and S. S. P. Parkin, *Appl. Phys. Lett.*, **77**(2000) 883.
- [37] N. Arao, Master Dissertation, Nagoya University, 2007 (in Japanese).
- [38] T. Ichikawa, Master Dissertation, Nagoya University, 2007 (in Japanese).

Chapter 4

MFM study of thermomagnetic writing on patterned TbFe films

4.1 Introduction

Magnetic force microscopy MFM [1,2] is a widely used experimental technique in order to investigate the magnetic microstructure of magnetic films and nanostructures since it allows one to visualize the stray field distribution above the surface of a magnetic sample on a 10 nm lateral scale [3,4].

The magnetization reversal process in bulk films is conventionally investigated from two types of remanence curves, the isothermal remanence curve (IRM) and the Direct Current (DC) demagnetization remanence curve (DCD) measured using AGM or VSM [5]. These curves are useful to get information show whether the reversal process is due to domain nucleation or domain wall motion, and these curves also give the distribution of energies associated with each process [6]. However, it is impossible to observe the magnetization process for micron or submicron size structured films. One of the method to investigate the magnetization process of microfabricated structure is

micro-Hall effect [7]. This is useful for the case that the film have perpendicular easy axis such as RE-TM. However, the MFM can not give the most direct information on the magnetization reversal of the microfabricated structure.

Since RE-TM films have a uniaxial perpendicular anisotropy, the domains in the film are oriented either upward downward direction, which exist either an attractive or repulsive force on the magnetized tip, which can be imaged as areas of different contrast in MFM images.

In this study, the MFM is employed not only to study the domain structure of the TbFe films, but also to characterize the thermomagnetic writing on the patterned TbFe film. The critical heating power is also evaluated by observing the domain structure after applying a heating current pulses in same specified increments.

4.2 MFM study of the magnetic structure

MFM detects the force or force gradient between the MFM tip and magnetic sample. The magnetic force acting on the tip can be written as [8]:

$$F_{t-s}(r) = \int \sum_{tip^{i=x,y,z}} \sum_{j=x,y,z} n_j M_i^T(r') \frac{\partial H_i(r+r')}{\partial r_j} dV' \quad (4.1)$$

where $M^T(r')$ is the tip magnetization of the volume element dV' in the tip and $H(r+r')$ is the stray field from the sample position. The consequence of the force directly bends the cantilever beam by the amount of $\delta z = F_n/k_{cb}$, where F_n is the component of the force normal to the cantilever, and k_{cb} is the spring constant of the cantilever. The bending of the cantilever can be detected by the deflection of the laser beam reflected from the top of the cantilever, and the deflection can be used to form MFM images. However, this mode is not commonly employed because such a dc

measurement exhibits poor signal to noise S/N ratio and strong tip dependence. Much higher sensitivity can be achieved in the ac mode by driving the cantilever at (or close to) its resonant frequency to reduce environmental noise [9], and to increase S/N using lock-in techniques or frequency modulation techniques [10]. In the ac mode, the resonance frequency shift df is given by $df/f = (1/2k_{cb})\partial F/\partial n$ (n = tip oscillation direction). An either attractive or repulsive interaction of the magnetic tip with the stray field of the sample leads to a force gradient acting upon the tip which in turn is converted into phase and resonance frequency changes of the cantilever oscillation. Provided that there is no mutual disturbance of the magnetic properties of the tip and the sample [11~13], the results of MFM investigations then allow to characterize the domain structure of a given sample.

To study the localized magnetic structure, there are generally two MFM measurement techniques: 1) *ex situ* measurement which is in the absence of external magnetic field; and 2) *in situ* technique in the presence of magnetic field which is helpful for characterizing in detail and comparing the switching behavior of individual magnetic nanoparticles. In this study, a special measurement technique was used to investigate the magnetization reversal of patterned films during thermomagnetic writing. Unlike the typical in-situ technique which varies an external field, the constant external field was applied to the sample, and a current pulse to generate the local heating was applied. After the application of a current pulse at constant external bias field, MFM images were taken to investigate the magnetization reversal. Consequently, the critical heating power for the thermomagnetic writing can be estimated from the measurement.

The microscope used in this work is a commercial AFM/MFM from Digital Instruments Dimension 3100 scanning probe microscope, operating in their

tapping/liftTM mode equipped with phase detection, which combines constant interaction and constant height modes to separate topographic and magnetic signals. The probes are commercial Co-covered tips with resonant frequency about 90 kHz and spring constant of 0.5 N/m approximately which have been magnetized along the pyramid axis. The lift height for the MFM imaging was typically set to 50 nm.

When imaging with an MFM, one concern is that stray fields from the magnetic tip can modify the micromagnetic structure of the sample. For in-situ measurement of this study, the TbFe films during thermomagnetic writing is “soft-magnetic”, however, the tip was kept away from the surface during the local heating, and the sample returned to room temperature (“hard-magnetic”) when the tip retrace the surface to confirm the magnetization reversal due to the local heating.

4.3 Design of the patterned TbFe films for thermomagnetic writing

As described in chapter 3, TbFe film has high anisotropy and low Curie temperature. In order to employ TbFe in the thermomagnetic writing MTJ, generally the current pulse will be applied through the tunneling junction at the presence of external field. However, in the case of amorphous TbFe, it is considered to be possible to heat the TbFe by flowing a current pulse directly into the film because of its high electric resistivity resulted from the amorphous structure. The direct current pulse heating is a convenient method to carry out a basic experiment on the thermomagnetic writing, since it does not require the complicated MTJ stack and microfabricated TbFe single layer is sufficient. In addition, the direct observation of the domain structure in TbFe by using surface sensitive MFM is possible, which will be helpful to understand the

thermomagnetic writing in detail. This study mainly focused on the required heating power/energy for switching the perpendicular magnetized TbFe depending on the current pulse width, external field, lateral size of TbFe layer. The values estimated in this study will be also applicable in real perpendicular MTJ structure. Thus to perform basic experiments mentioned above, a narrow path structure was microfabricated in the TbFe single layer as shown in Fig. 4.1, which has an element area of $L \times W \mu\text{m}^2$. The narrow path is directly connected to lead wires which are linked to large contact pads. The narrow path, lead wires, and contact pads are made of the same material, TbFe to significantly reduce the fabrication steps.

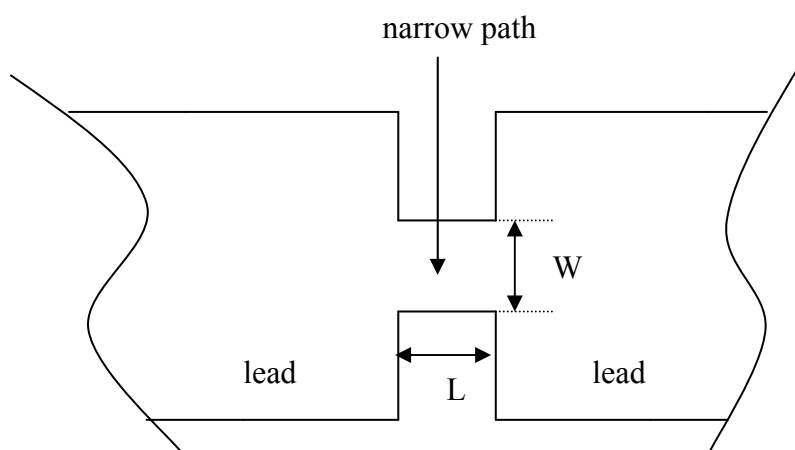


Fig. 4.1. A schematic depiction of the patterned-film for pulse-writing.

If we apply the current pulse to this structure, the high current density will be achieved only in the narrow path and Joule heating to increase the temperature up to Curie point of TbFe. In this study, lithography (both photolithography and EB lithography) and etching processes were used to microfabricate TbFe films.

4.3.1 Fabrication using photolithography and etching process

The process of fabrication using photolithography and etching process to obtain the required pattern is almost the same, as described in chapter 3. The only possible difference is the exposure time in the photolithography which is dependent on the exposure area. Here the exposure time was set to 13 sec, and the process here can be described briefly:

- 1) SiN (10nm) / TbFe (80 nm) / SiN (10nm) trilayer films were prepared using 3-target RF magnetron sputtering system on Si substrate with oxidized surface layer of 500 nm, as shown in Fig. 4.2 .

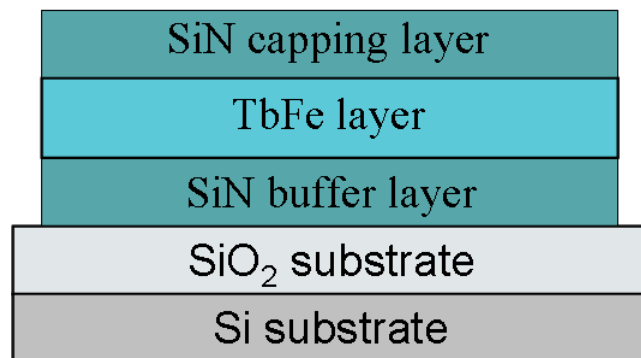


Fig.4.2. The structure of the trilayer films.

- 2) The thin films coated by photoresist (S1813) was exposed through Cr mask by UV light, and the pattern was transferred by the development.
- 3) The sample was etched by Ar⁺ ions produced by ECR plasma source for 20 min.
- 4) The photoresist was striped using Remover 1165.

4.3.2 Fabrication using EB lithography and etching process

The process of EB lithography followed by ECR etching is briefly summarized below:

- 1) The sample SiN (10nm) / TbFe (80 nm) / SiN (10nm) was cleaned with acetone and IPA and baked at 170 °C for dehydration.
- 2) The HMDS was coated as a pre-resist priming layer.
- 3) The EB resist ZEP520A was spin coated with 500 rpm for 5 seconds, and with 1000 rpm for 30 sec. The resist was pre-baked at 170°C for 30 minutes in convection oven.
- 4) The sample with resist was exposed in e-beam irradiation, as shown in the left of Fig. 4.3.
- 5) After the exposure, the resist was dipped introduced in the developer (Xylene), and rinsed using IPA. The exposed region of resist by e-beam was removed, as shown in the middle of Fig. 4.3.
- 6) The Ar⁺ ion etching was carried out to transfer the pattern of the resist to the sample.
- 7) The resist was striped by O₂ plasma ashing by using ECR sources and/or chemical (ZDMAC) washing in the ultrasonic bath. The required pattern was obtained, as shown in the right of Fig. 4.3. Optical microscope image of the microfabricated sample (top view) is shown in Fig. 4.4.

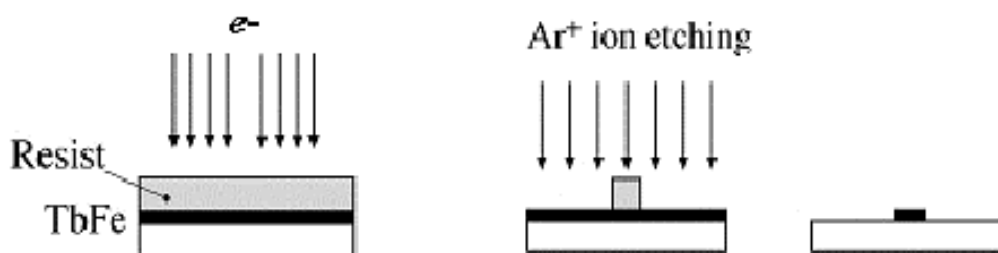


Fig.4.3. The process of EB-lithography followed by ECR etching.

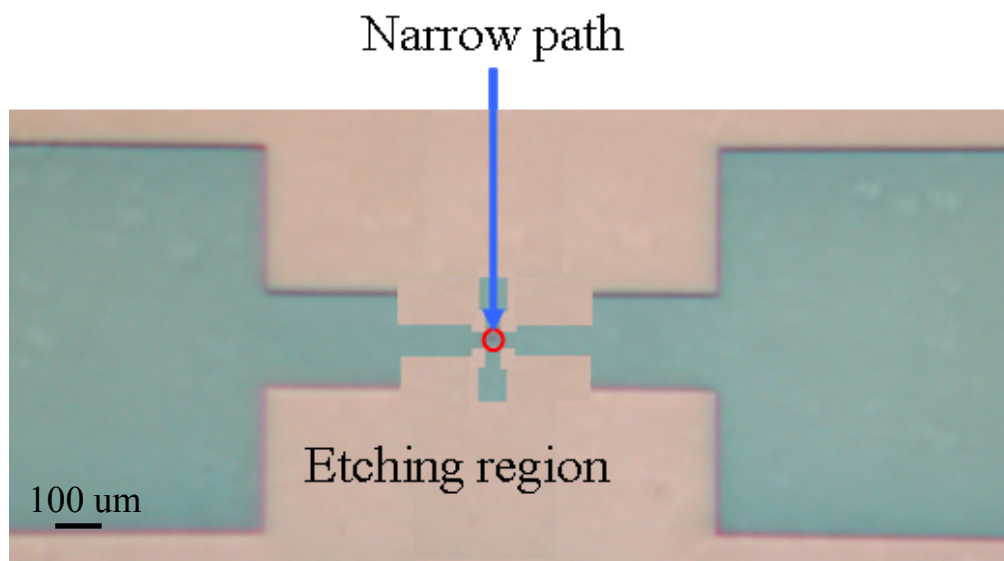


Fig. 4.4. Optical microscope image after the fabrication (top view).

4.4 Experimental setup

After fabrication, the sample was fixed on the circuit board which has a matching resistance of 50Ω and a reference resistance. The wire bonding was used to make contacts between the pads of the patterned films and the circuit board. The heating pulse produced by a pulse generator can be applied to the patterned film through 50Ω co-axial cable. The circuit board with the sample was placed on the permanent magnet which produces 100 Oe perpendicular to the sample surface. The permanent magnet and the sample was fixed on the MFM stage to image the domain structure after the thermomagnetic writing performed by applying a current pulse under the external field. The reference resistance to monitor the waveform of the applied current pulse was varied from 500 to 800Ω depending on the sample resistance. The reference resistance should have the same resistance as that of the connected patterned film to achieve the

rectangular waveform of the current pulse. Figure 4.5 shows the schematic diagram of the experimental setup.

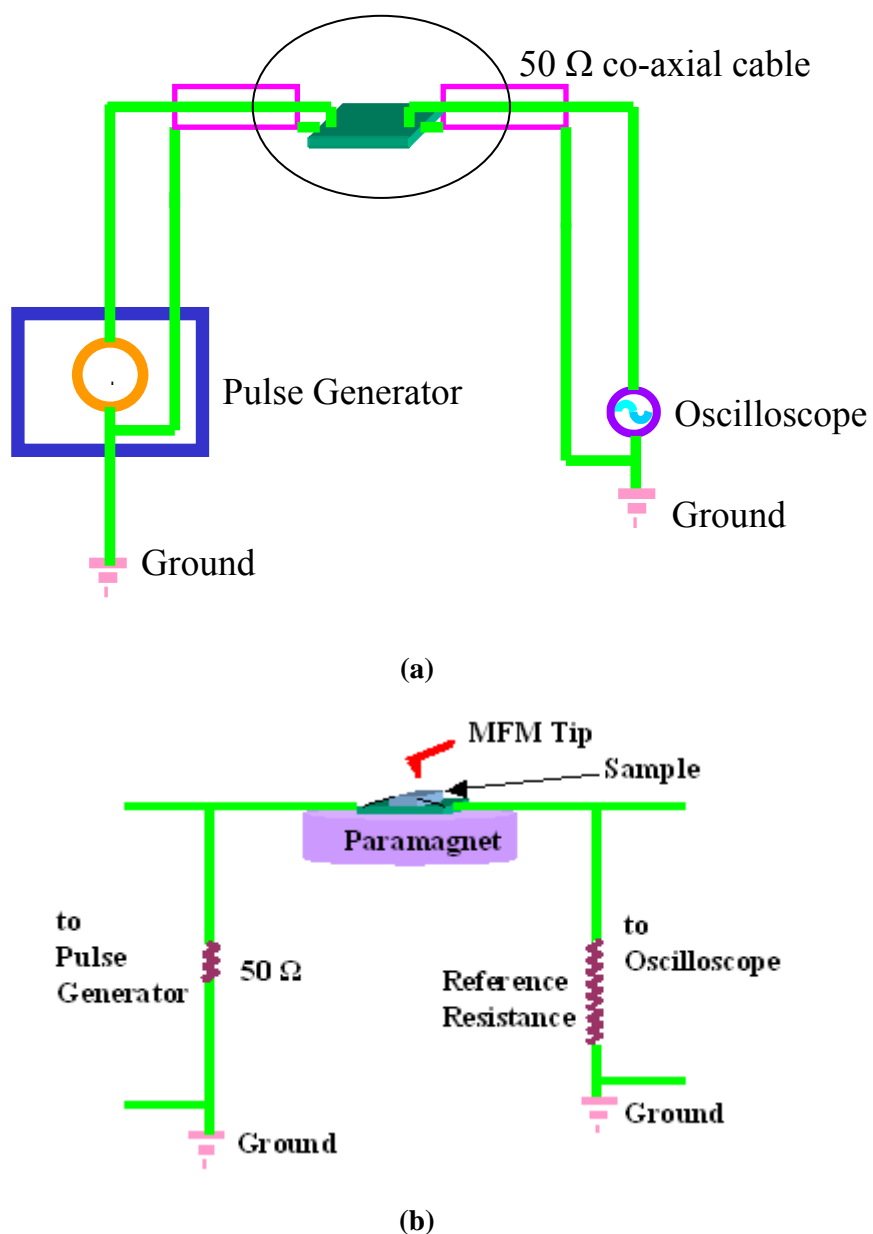


Fig. 4.5. (a) A schematic diagram of the experimental setup and (b) local magnifying the schematic diagram of the circuit.

4.5 Study of the thermomagnetic writing

4.5.1 The material properties of TbFe films for thermomagnetic writing

The thermomagnetic writing was employed on the patterned Tb₂₀Fe₈₀ thin film. Its resistivity is about 160 $\mu\Omega$ cm. The coercivity of the films was measured using a magneto-optical Kerr effect (MOKE) at various temperatures.

Figure 4.6 shows the dependence of the coercivity H_c on temperature. The required switching field decreases significantly with an increase in film temperature. The switching field decreases from 2400 to 100 Oe with film heating from room temperature to around 90 °C. The Curie point T_c of the Tb₂₀Fe₈₀ film is estimated to be about 120 °C, which agrees with that previously reported [14].

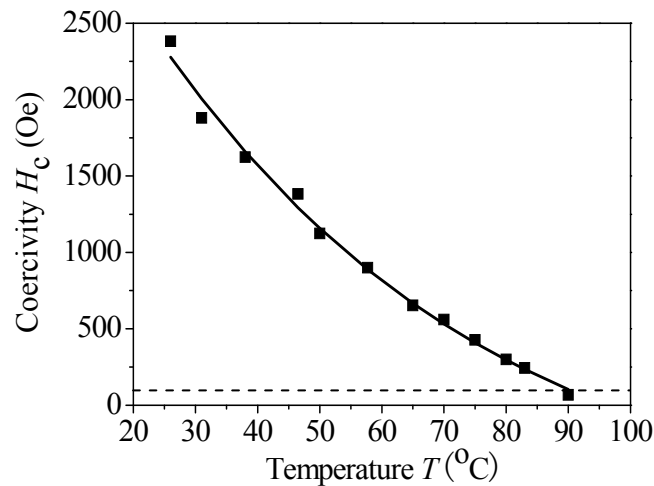


Fig. 4.6. Temperature dependence of Tb₂₀Fe₈₀ film coercivity.

The compensation temperature of this type TbFe alloys is below room temperature due to the fact the film is TM-rich alloys, which is indicated from the polarity of Kerr rotation angle.

4.5.2 Study of the thermomagnetic writing on patterned films fabricated by photolithography

Figure 4.7 shows MFM images of the film fabricated by the photolithography technique. Fig. 4.7(a) is the MFM image taken just after the micro fabrication. Clear contrast of stripe domains was observed in the whole area except for the etched region. Fig. 4.7(b) shows MFM image of the same film after applying a pulse current of 9mA with the pulse duration of 1 μ s in a magnetic field of +500 Oe. A black domain

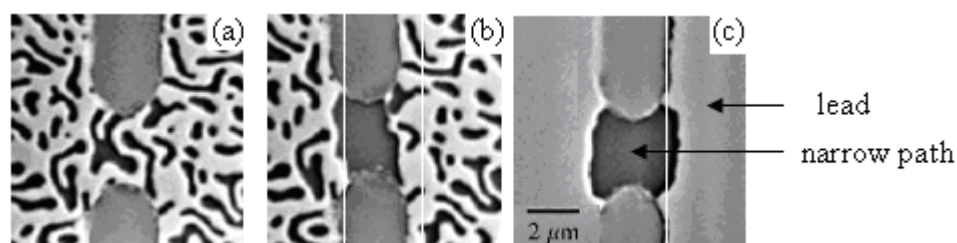


Fig. 4.7. MFM images of photolithography fabricated TbFe element of $2 \times 2 \mu\text{m}^2$ square. (a) before thermomagnetic writing, (b) after writing applying a field of +500 Oe, and (c) after writing in a field of +500 Oe for the initially saturated sample in a field of -15 kOe.

appeared in the narrow path region where the current has been concentrated and the local temperature increase is expected due to the Joule heating by the high current density. The estimated current density was $3.7 \times 10^6 \text{ A/cm}^2$ which will produce the Joule heating energy of 1.3 nJ and power of 1.3 mW in the narrow path. Figure 4.7 (c) shows the case the sample that was initially saturated by applying a field of -15 kOe after the application of 9mA current pulse under the external field of +500 Oe. Thermomagnetic writing was confirmed in the region of the narrow path.

Figure 4.8 shows the results of the thermomagnetic writing on photolithography fabricated TbFe, for the current pulse duration of 100 ns. Magnetic contrast showing demagnetized state for the film just after the fabrication as shown in Fig. 4.8 (a). The

patterned film was saturated by applying -5 kOe field, as shown in Fig. 4.8 (b). When an current pulse of 20 mA corresponding current density of 7.81×10^6 A/cm², was applied in the narrow path under the presence of a magnetic field of +500 Oe, the local magnetization reversal due to the thermomagnetic writing was confirmed, as shown in the Fig. 4.8(c).

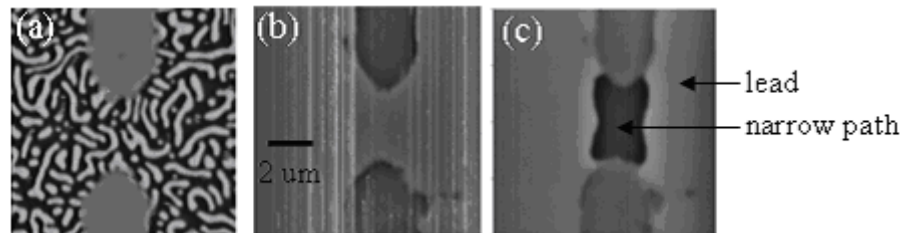


Fig. 4.8. MFM images of photolithography fabricated TbFe element of $2.8 \times 3.2 \mu\text{m}^2$. (a) before thermomagnetic writing, (b) after saturation by -5 kOe, (c) after thermomagnetic writing by a current pulse of 20 mA under a field of +500 Oe.

4.5.3 Study of the thermomagnetic writing on patterned films fabricated by EB lithography

In 4.5.2, thermomagnetic writing on the photolithography fabricated TbFe was studied as a preliminary experiment. If we consider the high density and high speed MRAM, the “writing” field, pattern size and the pulse duration should be decreased further. In order to discuss the critical heating power for the thermomagnetic writing to be used for designing the high density thermally assisted MRAM. EB lithography technique to obtain the patterned film down to deep submicron size was employed. The magnetic domain structure was checked after applying by using magnetic force microscopy (MFM) to evaluate the minimum current pulse required for writing on the patterned-films. The size of patterned film and etching depth were measured by AFM.

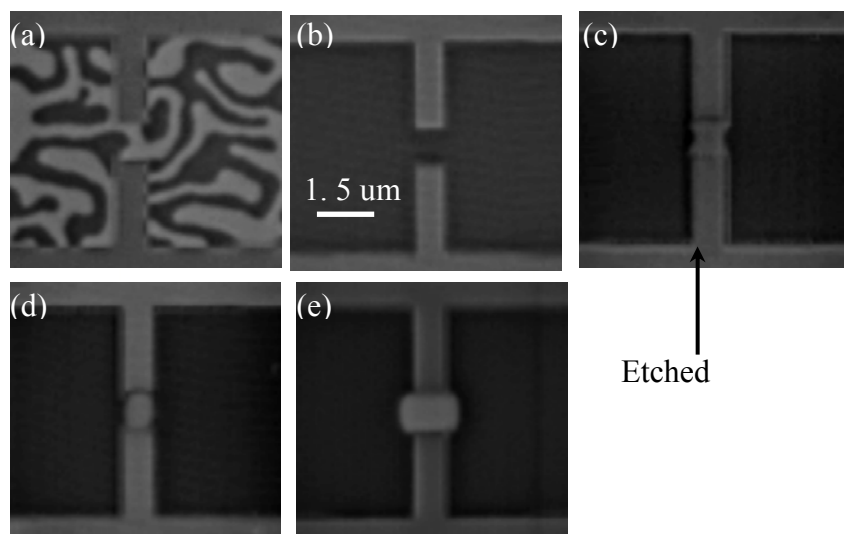


Fig. 4.9. MFM images of patterned-film with $0.8 \times 0.8 \mu\text{m}^2$. (a) before thermomagnetic writing in demagnetization state; (b) after being magnetized upward; after thermomagnetic writing by applying 100 ns pulse width with (c) 3.35 mA, (d) 3.52 mA and (e) 3.86 mA current amplitude in the presence of downward 100 Oe field.

Figure 4.9 shows MFM images of patterned- film with a narrow-current path of $0.8 \times 0.8 \mu\text{m}^2$ size. Figure 4.9 (a) is the MFM image taken just after the micro fabrication, and magnetization perpendicular to the film plane produces clear dark and bright contrast of the image. The magnetic domain structure was observed in narrow path and lead regions, and no magnetic contrast was seen in the etched region, which means the successful fabrication of TbFe patterned film. The magnetization of the patterned TbFe can be saturated by applying an upward external magnetic field of 5 kOe as shown in Fig. 4.9 (b). The magnetization state remains unchanged just as in Fig. 4.9 (b), until a current amplitude exceeds 3.26 mA under a downward field of 100 Oe. This indicates the temperature does not rise sufficiently above the threshold value by Joule heating so that the required for a magnetization reversal is still larger than the external field of 100 Oe. An inverted magnetic domain was formed when the current amplitude is 3.35 mA as shown in Fig. 4.9 (c), whereas, the concave shaped magnetic domain was formed in

this writing condition and the boundary between narrow path and lead have not yet been switched. It is associated with low temperature of the boundary in comparison to that of the center region of the narrow path, which may be associated with the heat loss to the lead from the narrow path due to the heat diffusion into the lead wires. When the current amplitude is increased to 3.52 mA, the magnetic domain of the element was just switched completely as shown in Fig. 4.9 (d). When the amplitude is increased to 3.86 mA, the reversed magnetic domain is extended to the leads, which were composed of the same material as the part of the narrow path, as depicted in Fig. 4.9 (e).

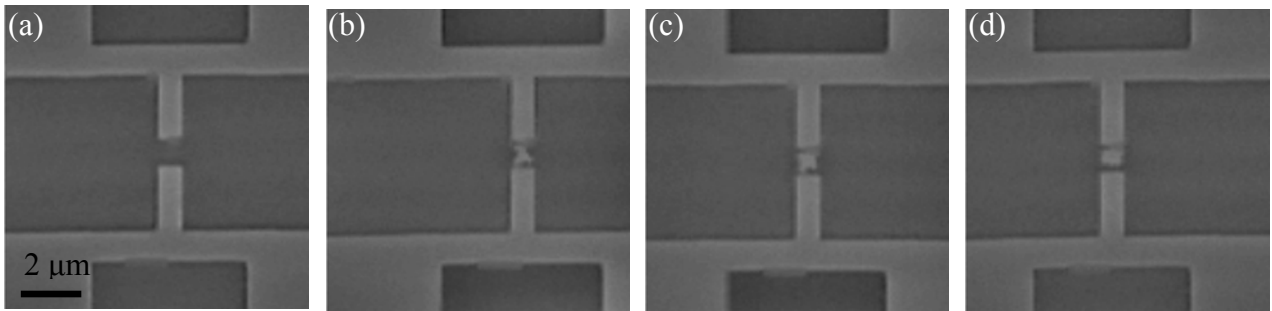


Fig. 4.10. MFM images of patterned-film with $0.86 \times 0.86 \mu\text{m}^2$. (a) after saturated upward; after thermomagnetic writing by applying 10 ns pulse width with (b) 8.13 mA, (c) 8.37 Ma, and (d) 8.6 mA current amplitude in the presence of downward 100 Oe field.

The same experiment was done in the case that the pulse duration was decreased to 10 ns. The MFM images from the patterned film of $0.86 \times 0.8 \mu\text{m}^2$ are shown in Fig. 4.10. The patterned film was saturated by applying upward field of -10 kOe (upward), and the different color can be clearly observed between the film and etched regions, as shown in Fig. 4.10 (a). The magnetization in the narrow path region was reversed by the thermomagnetic writing using a current pulse of 8.13 mA (power density is $1.79 \text{ mW}/\mu\text{m}^2$) under 100 Oe downward field. When the heating current is increased to 8.6

mA ($2.0 \text{ mW}/\mu\text{m}^2$), the complete reversal of the magnetization in the narrow path was confirmed.

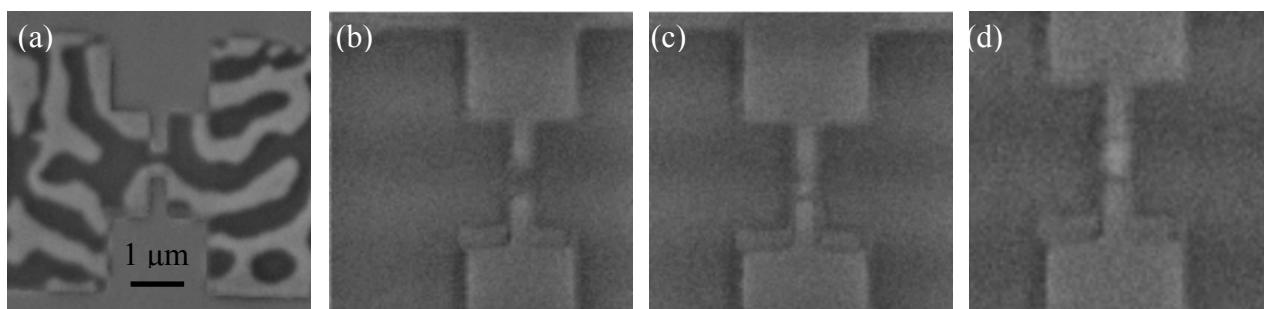


Fig. 4.11. MFM images of patterned-film with current path of $0.47 \times 0.39 \mu\text{m}^2$. (a) before thermomagnetic writing in demagnetization state; (b) after being magnetized upward; after thermomagnetic writing by applying 10 ns pulse width with (c) 4.60 mA, (d) 4.67 mA.

It is interesting to study the thermomagnetic writing on the deep submicron patterned films. Figure 4.11 shows the MFM images taken from the patterned-film with a narrow path of $0.47 \times 0.39 \mu\text{m}^2$. The clear magnetic contrast can be observed in the film region at the demagnetization state (see Fig. 4.11 (a)). After the magnetization saturation (as shown in Fig. 4.11 (b)), the thermomagnetic writing was carried out. The critical heating current can be estimated to be 4.67 mA by checking the MFM images of Fig. 4.11 (c) and (d). The associated power density was $2.0 \text{ mW}/\mu\text{m}^2$ which is same as the value estimated for $0.86 \times 0.86 \mu\text{m}^2$ TbFe. This means that the size dependence of the required power density for the thermomagnetic writing is not so significant in these fabrication sizes.

Figure 4.12 shows the MFM images of the $0.38 \times 0.28 \mu\text{m}^2$ patterned TbFe films. Figure 4.12 (a) is the MFM image taken just after the micro fabrication. Clear magnetic contrast of maze domains showing demagnetized state is observed in the whole area

except for the etched region. In the presence of downward field of 100 Oe, the magnetization in the narrow path was just completely inverted when the amplitude of heating pulse arrives at 5.7 mA, as shown in Fig. 4.12 (c). The associated critical heating power density and energy density are $4.7 \text{ mW}/\mu\text{m}^2$ and $23.3 \text{ pJ}/\mu\text{m}^2$, respectively.

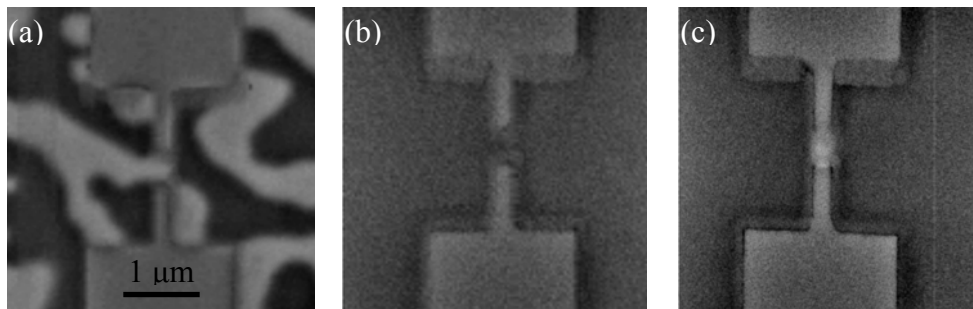
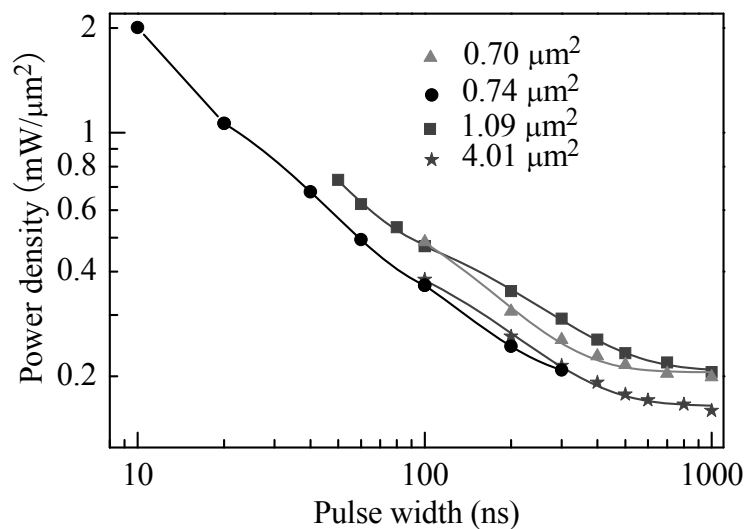


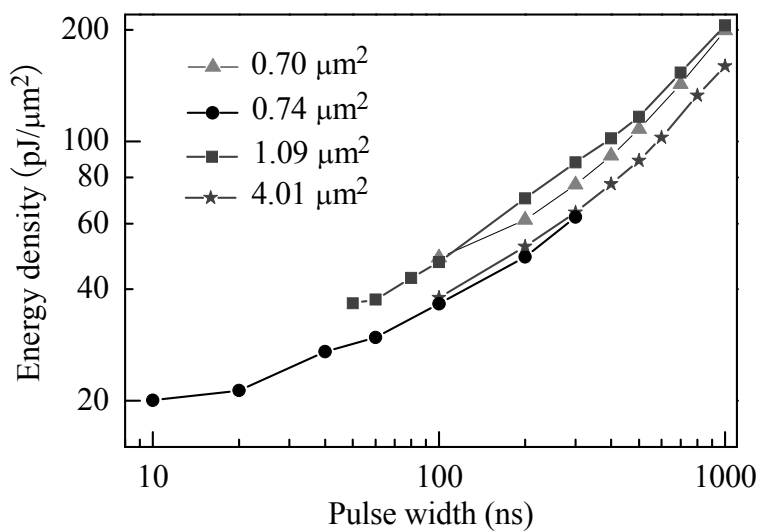
Fig. 4.12. MFM images of patterned film with the current path of $0.38 \times 0.28 \mu\text{m}^2$. (a) before thermomagnetic writing in demagnetization state; (b) after being magnetized upward, and (c) after thermomagnetic writing using pulse width of 5 ns at current amplitude of 5.7 mA with downward field of 100 Oe.

4.5.3.1 The dependence of power and energy densities on the pulse width

The values of required power and densities are plotted as a function of pulse width ranging from 10 to 1000 ns for 4.01, 1.09, 0.74, $0.70 \mu\text{m}^2$ patterned films at the presence of 100 Oe external field, as shown in Fig. 4.13. For all the elements, the required power densities decrease and the energy densities increase with increasing pulse duration. The required power density for writing using the pulse duration of 10 ns is estimated to be around $P = 2 \text{ mW}/\mu\text{m}^2$, which corresponds to the energy density of $E = 20 \text{ pJ}/\mu\text{m}^2$.



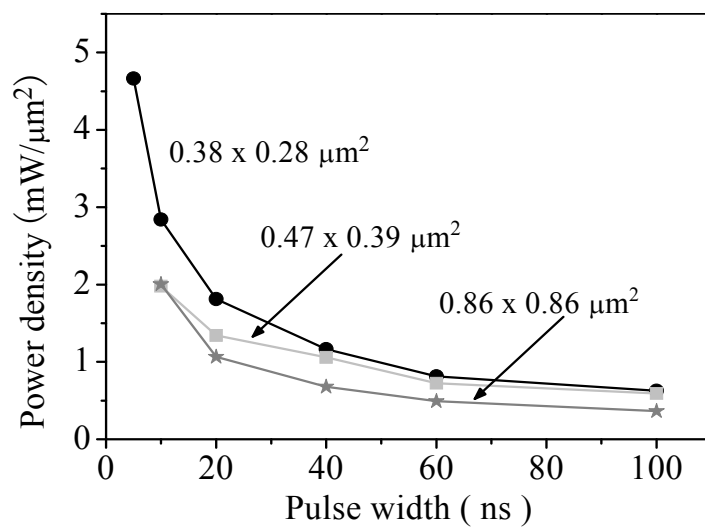
(a)



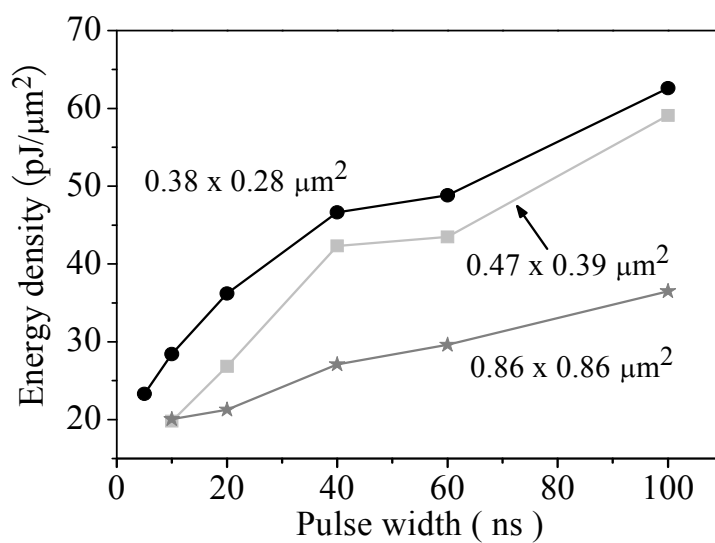
(b)

Fig. 4.13. Write (a) power density and (b) energy density as a function of pulse width for 4.01, 1.09, 0.74, and 0.70 μm² patterned films at the presence of 100 Oe external field.

The dependence of the required power/energy densities on the pulse width for the deep submicron patterned films at the presence of 100 Oe external field, is shown in Fig. 4.14. The power density decreases by 87% from $4.67 \text{ mW}/\mu\text{m}^2$, when the pulse width decreases from 5 to 100 ns for $0.38 \times 0.28 \mu\text{m}^2$ patterned film, while the energy density increases by 168.6% from $23.31 \text{ pJ}/\mu\text{m}^2$. And the required power density decreases from about $2 \text{ mW}/\mu\text{m}^2$ to 0.6 and $0.37 \text{ mW}/\mu\text{m}^2$ for $0.47 \times 0.39 \mu\text{m}^2$ and $0.86 \times 0.86 \mu\text{m}^2$ patterned films, respectively, when the pulse width ranging from 10 to 100 ns. The associated energy density increases from $20 \text{ pJ}/\mu\text{m}^2$ to 59 and $36.5 \text{ pJ}/\mu\text{m}^2$, respectively. For the two deep submicron ($0.38 \times 0.28 \mu\text{m}^2$ and $0.47 \times 0.39 \mu\text{m}^2$) patterned films, the energy density increases quickly with the pulse width compared to the case of the submicron ($0.86 \times 0.86 \mu\text{m}^2$) patterned film, which might be related to the size of the patterned film and the heat diffusion length in the SiO_2 for a given pulse width. The heat diffusion length in SiO_2 at 100 ns is estimated to be 420 nm which is almost equal to the lateral size of the small patterned films. This means that the heat diffuses into SiO_2 layer three dimensionally. While, in the large patterned film, the heat diffuses rather one dimensionally, and thus small energy density is considered to be sufficient to increase the temperature of the patterned films up to writing temperature (Curie temperature).



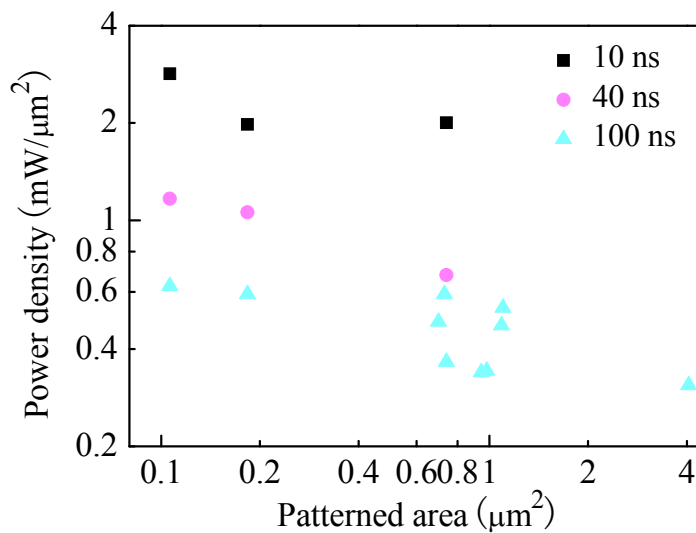
(a)



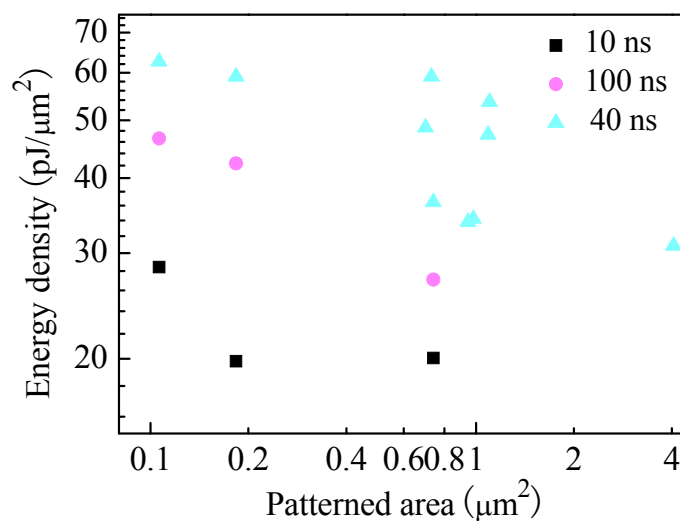
(b)

Fig. 4.14. Required (a) power density and (b) energy density plotted as a function of pulse width for patterned films with the size of $0.38 \times 0.28 \mu\text{m}^2$, $0.47 \times 0.39 \mu\text{m}^2$ and $0.86 \times 0.86 \mu\text{m}^2$ at the presence of 100 external field.

4.5.3.2 The dependence of power and energy densities on the size



(a)



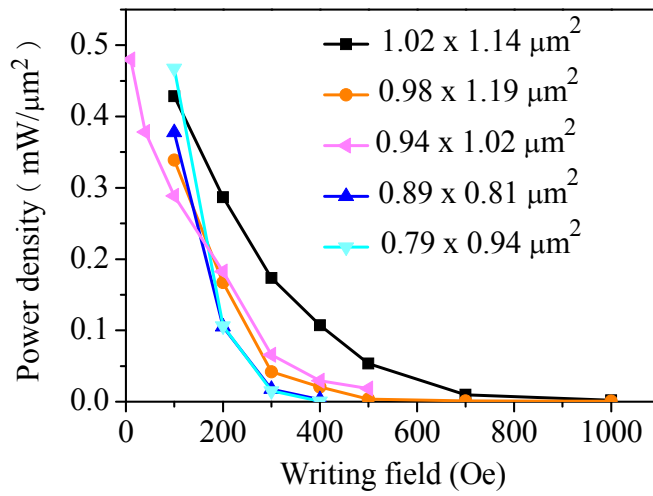
(b)

Fig. 4.15. (a) power density and (b) energy density required for the writing of various sized patterned films at the presence of 100 Oe external field. The results for pulse widths of 10, 40 and 100 ns are shown.

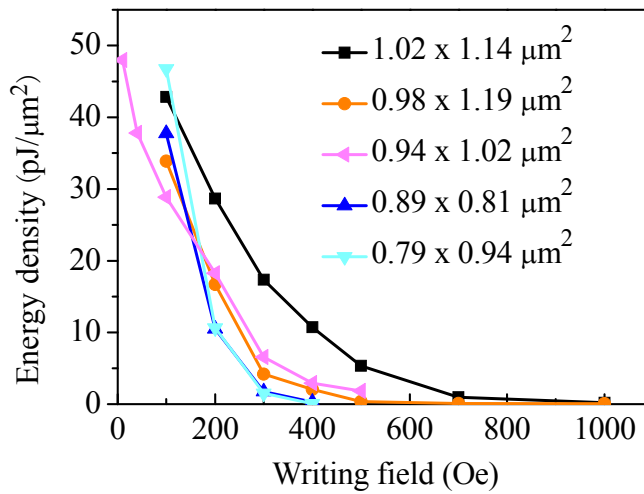
The required power for a given pulse width also depends on the patterned film size. The heating power and energy densities as a function of the patterned film area at the presence of 100 Oe external field are shown in Fig. 4.15 plotting the experimental data. It can be seen that required write power/energy density increases as the patterned film area is scaled down. When the dimension of the patterned film is much larger than the heat diffusion length at a given pulse width, the dependence of the required power/energy density on the patterned area becomes insignificant since the heat diffusion could be approximated as one-dimensional heat flow. We should note that the required energy density for short pulse writing (10 ns) is much smaller than that for long pulse writing (40 and 100 ns) and the dependence of the power/energy density on the patterned area becomes insignificant.

4.5.3.2 The dependence of power and energy densities on the writing field

The heating power and energy densities as a function of writing field for the 100 ns current pulse are shown in Fig. 4.16. The values of required power and densities are plotted as the writing field ranging from 10 to 1000 Oe for 1.02×1.14 , 0.98×1.19 , 0.81×0.89 , $0.79 \times 0.94 \text{ } \mu\text{m}^2$ patterned films. For all the elements, the required power and the energy densities decrease with increasing writing field. Moreover, the required power and energy densities decrease rapidly with increase of the writing field in the small writing field, while decrease slowly in the large writing field. This is associated with the fact that the coercivity of thin film decreases rapidly and then slowly with increase of the temperature. It seems that the smaller patterned films are more sensitive to the writing field compared to the large ones.



(a)



(b)

Fig.4.16. Required heating (a) power density and (b) energy density dependence on the writing field for patterned films with the size of 1.02×1.14 , 0.98×1.19 , 0.94×1.02 , and 0.79×0.94 μm², and the pulse width of the heating pulse is 100 ns.

4.6 Summary

The patterned films were fabricated using photo-lithography or EB lithography, followed by Ar⁺ ion etching process. From the MFM image taken just after the micro fabrication, the magnetic domain structure was only observed in narrow path and lead regions, and no magnetic contrast was seen in the etched region, which means the successful fabrication of TbFe patterned film. Thermomagnetic writing was performed on micro-fabricated TbFe film by applying a current pulse to the film itself under the external field. The critical current (the minimum current for successful writing) was estimated from MFM measurement after the application of a current pulse whose amplitude was elevated with small step. The dependence of required power and energy densities on the patterned film size, pulse width and writing field was investigated. The dependence of the heating power/energy density on the pulse width was experimentally measured for pulse widths ranging from 5 up to 1000 ns. For all the elements, the required power densities decrease and the energy densities increase with increasing pulse duration. The required power density for writing using the pulse duration of 10 ns is estimated to be around $P = 2 \text{ mW}/\mu\text{m}^2$, which corresponds to the energy density of $E = 20 \text{ pJ}/\mu\text{m}^2$. Thermally assisted switching at low power density ($\sim 4.7 \text{ mW}/\mu\text{m}^2$) and energy density ($\sim 23 \text{ pJ}/\mu\text{m}^2$) is found to be possible for deep submicron patterned RE-TM alloys using a 5 ns current pulse. The required energy density for short pulse writing (10 ns) is much smaller than that for long pulse writing (40 and 100 ns) and the dependence of the power/energy density on the patterned area becomes insignificant. The required power and the energy densities decrease with increasing writing field for all patterned films. Moreover, the required power and energy densities begin to decrease rapidly and then slowly with increase of the writing field.

References

- [1] Y. Martin and H. K. Wickramasinghe, *Appl. Phys. Lett.*, **50** (1987) 1455.
- [2] J. J. Saenz, N. Garcia, P. Grütter, E. Meyer, H. Heinzelmann, R. Wiesendanger, L. Rosenthaler, H. R. Hidber, and H. J. Güntherodt, *J. Appl. Phys.*, **62** (1987) 4293.
- [3] Y. Martin, D. Rugar, and H. K. Wickramasinghe, *Appl. Phys. Lett.*, **52**(1988) 244.
- [4] A. Di Carlo, M. R. Scheinfein, and R. V. Chamberlin, *Appl. Phys. Lett.*, **61**(1992) 2106.
- [5] Y. C. Hsieh, S. N. Gadetsky, M. Mansuripur, and M. Takahashi, *J. Appl. Phys.*, **79** (1996) 5700.
- [6] T. Thomson, K. O'Grady, *J. Phys. D*, **30** (1997) 1566.
- [7] J. Schmidt, G. Skidmore, S. Foss, E. Dan Dahlberg, C. Merton, *J. Magn. Magn. Mater.*, **190** (1998) 81.
- [8] R. Wiesendanger and H. J. Güntherodt, *Scanning Tunneling Microscopy II*, Springer Ser. Surface Science, Vol. 28 (Springer, Berlin, Heidelberg 1992).
- [9] Y. Martin and H. K. Wickramasinghe, *Appl. Phys. Lett.*, **50** (1987) 1455.
- [10] T. R. Albrecht, P. Grutter, D. Horne and D. Rugar, *J. Appl. Phys.*, **69** (1991) 668.
- [11] P. Grütter, D. Rugar, H. J. Martin, G. Castillo, S. E. Lambert, C. J. Lin, O. Wolter, T. Bayer, and J. Greschner, *Appl. Phys. Lett.*, **57** (1990) 1820.
- [12] O. Wolter, T. Bayer, and J. Greschner, *J. Vac. Sci. Technol. B* **9** (1991) 1353.
- [13] W. Rave, L. Belliard, M. Labrune, A. Thiaville, and J. Miltat, *IEEE Trans. Magn.*, **30** (1994) 4473.
- [14] N. Heiman, K. Lee, and R. I. Potter, *AIP Conf. Proc.* **29** (1976) 130.

Chapter 5

Dynamic heating in patterned TbFe films

5.1 Introduction

It is important for understanding of the experiment results to analyze the heat diffusion during thermomagnetic writing. In this chapter, the dynamical heating process of the patterned RE-TM films was systematically studied. The simulation of the heat diffusion was carried out. The simulation method is presented in section 5.2 and results are discussed in section 5.3. Data reveal two different heating regimes depending on the heating current pulse duration. The influence of the current pulse width and narrow path area on the required power/energy density are compared with the experiment results in section 5.4 and 5.5, respectively.

5.2 Simulation method

Simulation of the thermomagnetic writing process has been already done in various works [1~7]. The first modeling of a RE-TM alloys, GdCo, was studied by Huth [2]. This model is valid when the wall motion process dominates and writing process can be described by the expansion or contraction of a domain wall. However, this model is

obviously not applicable for the writing process which gives rise to multidomain behavior. To account for the cases where many independent nucleation sites appear to be active, the “nucleation field” model was introduced by Suits et al [7]. In the “nucleation field” model, the criterion for the initiation of magnetization reversal is a comparison of total internal field, H_t , which consists of demagnetization field plus applied field H_a , with a nucleation field H_n :

$$H_t = H_d + H_a > H_n \quad (5.1)$$

For reversal of a small region to occur, the total field in that region must be at least as large as H_n , which is the field required to nucleate the domain reversal.

In our experiment, the external field and the temperature dependent coercivity was just compared as a rough approximation. In the TbFe near the compensation composition, the magnetization becomes quite small due to the antiferromagnetic coupling between Tb and Fe moments as described in section 5.2.2, and the demagnetization field was estimated to be smaller than 100 Oe writing field. Thus as the first order approximation, the effect of the demagnetization field was neglected

5.2.1 Determination of thermal parameters and temperature profile

In order to estimate the temperature distribution in the patterned films during and after the application of the current pulse, three-dimensional heat flow in the multilayer structure was simulated by an alternating direction-implicit technique to solve the heat equation [8]. A cylindrical coordinate system was used to reduce the calculation time.

$$c_n(r, z, t) \frac{\partial T(r, z, t)}{\partial t} - k_n(r, z, t) \left(\frac{\partial^2}{\partial r^2} + \frac{\partial}{r \partial r} + \frac{\partial^2}{\partial z^2} \right) T(r, z, t) = g(r, z, t) \quad (5.2)$$

Here, c_n and k_n are the specific heat capacity and the heat conductivity of the n -th layer respectively, T is temperature, and t is time. The Joule heating of the narrow path was assumed to be a heat generation with circular symmetry $g(r, z, t)$. When the electrical leads are much thinner than the surface area of the narrow path, the influence of heat dissipation into the leads can be neglected. In the simulation model, we omit the electrical leads and the thin SiN layers that have similar thermal conductivity to the SiO₂ substrate [9~11]. A schematic of the simulated structure is shown in Fig. 5.1. It is assumed that the ambient temperature is 25 °C.

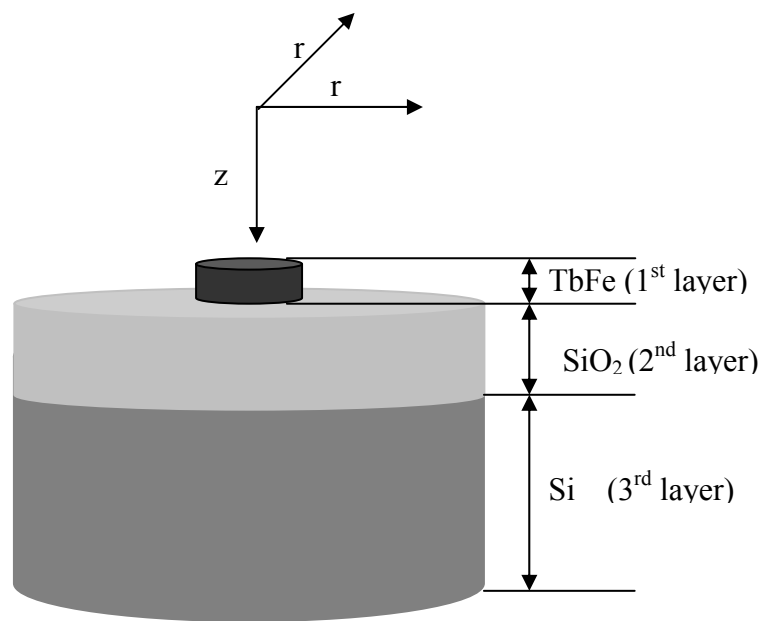


Fig. 5.1. Schematic depiction of multilayer structure based on cylindrical coordinate system used in heat flow simulation.

The bulk values of the thermal conductivity and heat capacity reported in Refs. 11 and 12 were assumed for the Si substrates and oxide layer (500 nm SiO₂), and they are summarized in Table 5.1. However, bulk values are not applicable for the thin metallic film layers and, in general, there is a substantial difference in the thermal conductivity

between thin film and the bulk form. In the temperature region of interest, the thermal conductivity K of the film can be deduced from its electrical conductivity. For our TbFe film, the contribution from conductive electrons, K_{el} , is estimated to be $0.045 \text{ W cm}^{-1} \text{ deg}^{-1}$ using the Wiedemann-Franz law, and the lattice contribution, K_{la} , is estimated to be about 1/3 of K_{el} [13]. The sum of these two components, $0.06 \text{ W cm}^{-1} \text{ deg}^{-1}$, was taken to be the total thermal conductivity of the film. The heat capacity of TbFe was obtained from Ref. 10, and is also given in Table 5.1.

Table 5.1. Thermal parameters used in the simulation.

Materials	Specific heat ($\text{J cm}^{-3} \text{ deg}^{-1}$)	Thermal conductivity ($\text{W cm}^{-1} \text{ deg}^{-1}$)	Reference
Si	1.63	1.5	12
SiO ₂	1.67	0.015	11
TbFe film	2.4	0.06	

5.2.2 Calculation of the stray field

To estimate the stray field, the shape of microfabrication is shown in Fig. 5.2. Fig 5.2 (a) is the top-view image of the microfabricated films. The magnifying image of central part is depicted in Fig. 5.2 (b). The average stray field from lead or outer to narrow path S_i ($i=1,2\dots 10$) can be expressed by,

$$\bar{H}_{st} = \frac{1}{L^2} \iint_{\text{narrow}} dx_0 dy_0 \sum_{\text{narrow}} \sum_{i=1}^{10} \iint_{S_i} \frac{2hm(x,y)dxdy}{[(x-x_0)^2 + (y-y_0)^2 + h^2]^{3/2}} \quad (5.3)$$

Here, L is the length or width of narrow path, respectively. $M(x,y)$ is the local magnetization at point (x,y) in S_i region. While point (x_0,y_0) belongs to the narrow path.

In this study, we assume that the magnetization M of S_i is equal to the saturation magnetization M_s at room temperature, and is 80 emu/cc, since the M - H loop of the TbFe was square and the temperature of S_i will not be far from the room temperature during thermomagnetic writing. $2h$ is the thickness of the films (80 nm).

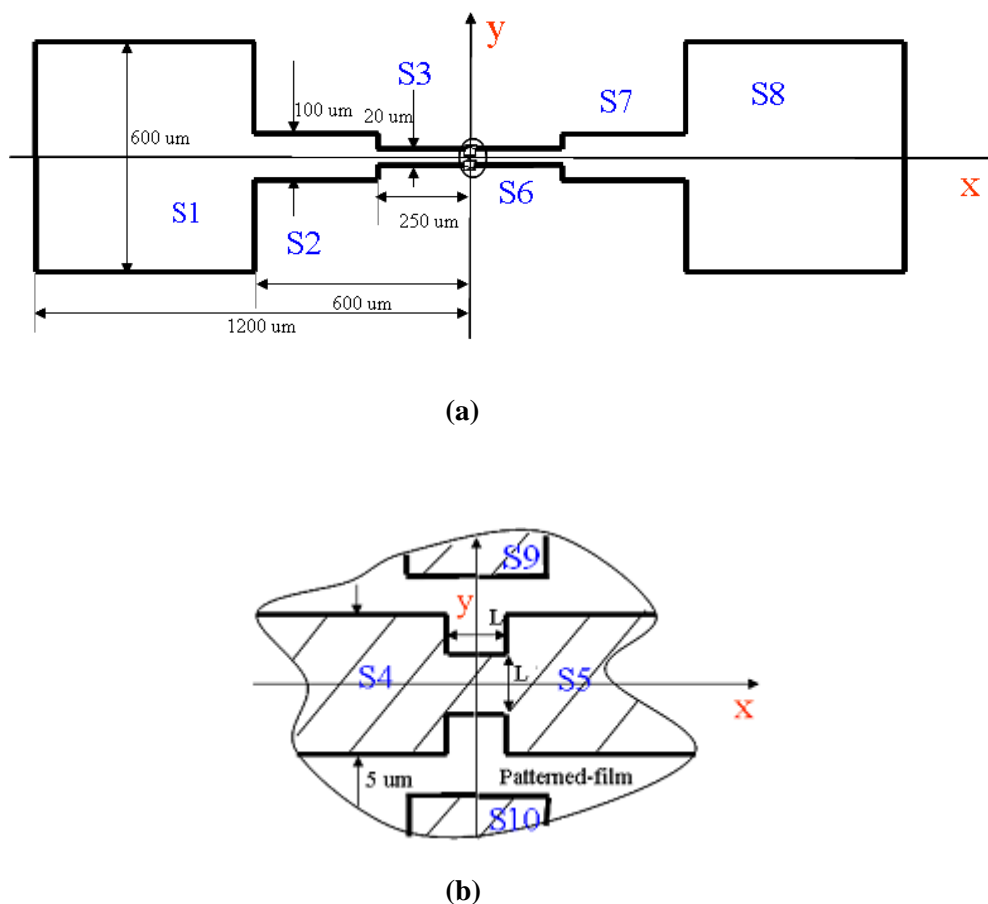


Fig. 5. 2. The (a) top-view and (b) local magnifying center part schematic diagram of microfabricated TbFe films.

The estimated stray fields at the origin for different patterned size are listed in Table 5.2.

Table 5.2. The value of stray field H_{st} for different size patterned film (L is length or width)

L (μm)	H_{st} (Oe)
2	11.8
1	24.2
0.5	49.5

As seen in Table 5.2, the stray field at the center of the narrow path is inversely proportional to L . Therefore, the stray field may be considered when the length of the narrow path L becomes much smaller, while it can be omitted for large sized pattern.

5.3 Numerical simulation

In this simulation, the stray (demagnetization) field from the outside of the narrow path has been omitted. This approximation will cause no problem if the temperature dependence of the coercivity is rather sharp. In this condition, the criterion for the initiation of magnetization reversal is only a comparison of applied field H_a , with local coercivity field H_c from the experiment. If the local coercivity is equal to or less than the applied field (100 Oe used in this study), it was assumed that the magnetization reversal occurs. In other words, if the temperature of the patterned films is equal to or higher than 90 °C at which the local coercivity is less than 100 Oe from MOKE measurements, the domain was assumed to reverse during the thermomagnetic writing process.

Numerical simulations were carried out considering the heat flow into the trilayer shown in Fig. 5.1. The average temperature over the TbFe patterned films is considered

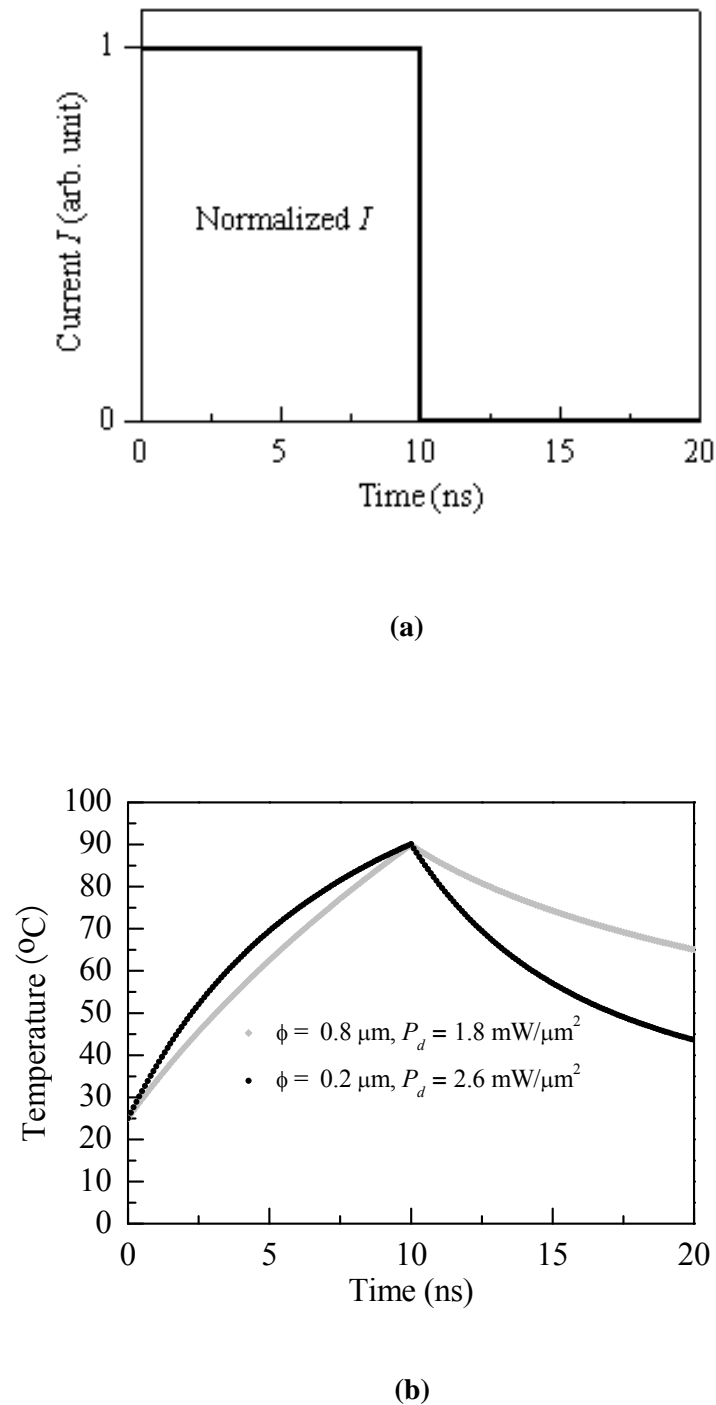


Fig. 5.3. (a) Current pulses used in the numerical calculations of temperature distribution in the trilayer, (b) Temperature evolution with time for two different TbFe layers with diameters of 0.8 μm and 0.2 μm , in which predetermined maximum temperature (90 $^{\circ}\text{C}$) is reached.

to be the temperature of the TbFe layer. The radial distribution of the temperature of the TbFe layer becomes significant when a long pulse width is assumed (typically > 20 ns), while the temperature is rather uniform for a short pulse width (< 20 ns). Figure 5.3 (b) shows the time dependence of temperature in TbFe layers with two different diameters: 0.8 and 0.2 μm , in which the current density was adjusted so that the temperature at 10 ns became 90 $^{\circ}\text{C}$. At this appointed temperature, 90 $^{\circ}\text{C}$, the magnetization of TbFe used in the experiment can be switched by applying 100 Oe external field. In this simulation, we assumed an ideal rectangular input current pulse, whose rise and fall times are zero, as depicted in Fig. 5.3 (a). Although the two curves have the same trend of temperature rising with time, they clearly show that the response time becomes faster for the TbFe of smaller diameter. This indicates that the thermomagnetic scheme has a great potential for application in ultrahigh-density MRAM design.

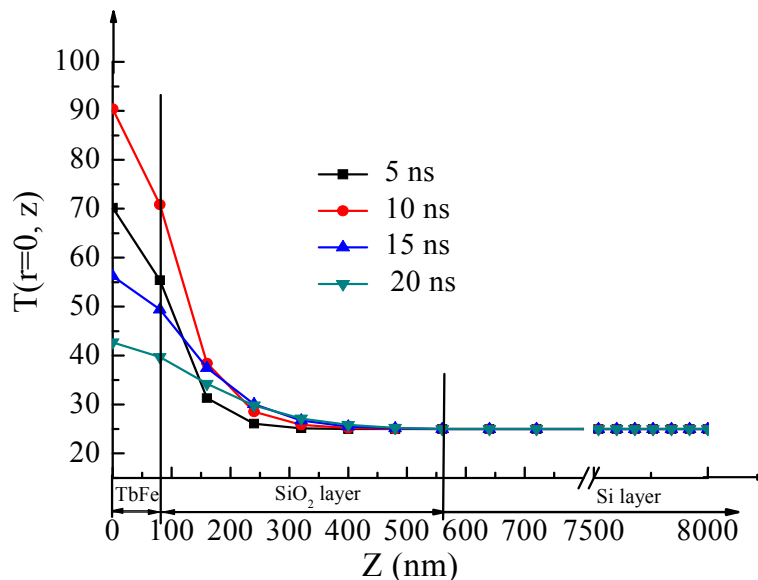


Fig. 5.4. Trilayer's temperature vs z at the center ($r = 0$) for several instants of time. At $t = 0$ the trilayer has been at ambient temperature (25 $^{\circ}\text{C}$). The current pulse is shown in Fig. 5.3 (a).

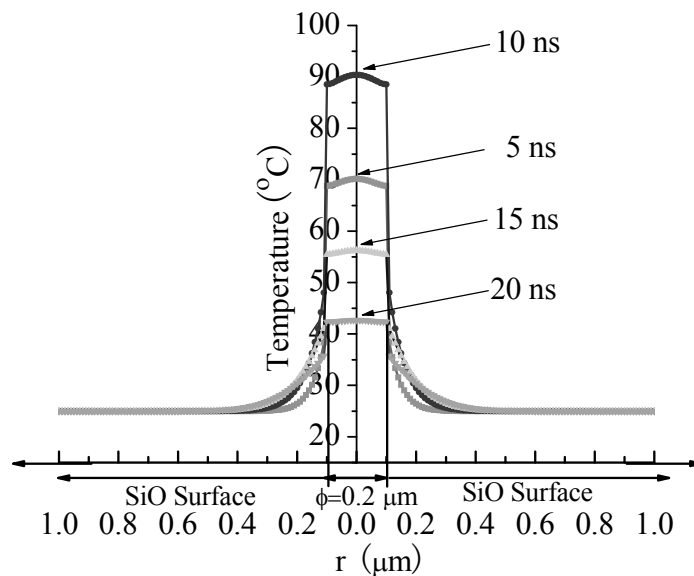
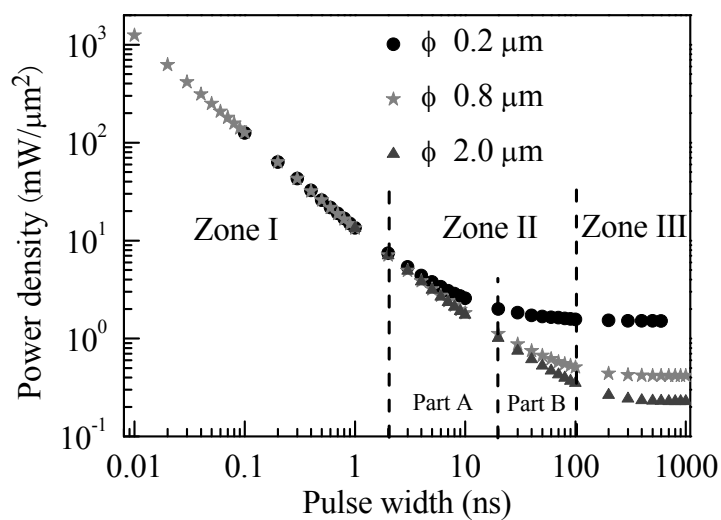


Fig. 5.5. Radial temperature distribution of the TbFe films and SiO surface at several instants of time. The heating pulse is shown in Fig. 4(a), and the diameter of heat generation (TbFe layer) is $0.2 \mu\text{m}$.

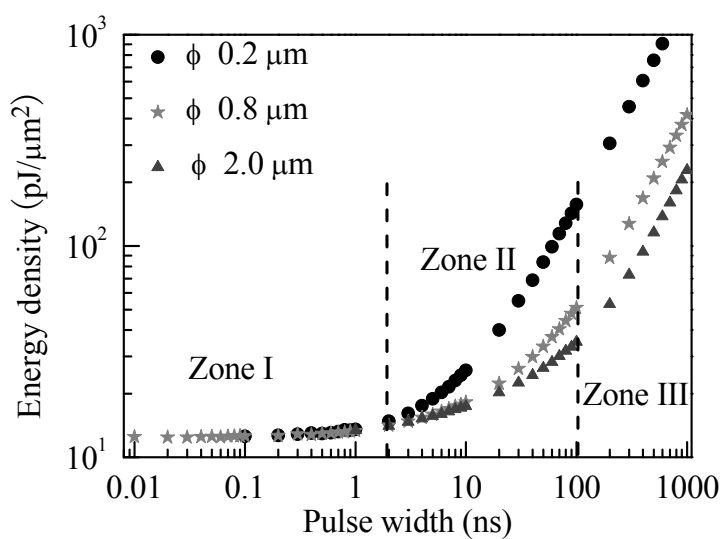
The heat generated in the TbFe layers diffuses in all directions and creates a complex pattern of temperature profiles. For the current pulse shown in Fig. 5.3 (a) temperature profiles of the trilayer are plotted in Figs. 5.4 and 5.5. Figure 5.4 shows temperature vs z at the center ($r = 0$), the curves for four instants of time are shown. At $t = 5 \text{ nsec}$, while the heating pulse is still on, the film has a high temperature; some of its energy is escaping to the SiO_2 layer. At $t = 10 \text{ nsec}$, with the heating pulse extinguished completely, the TbFe layer has the highest temperature and the film is cooling down. At $t = 15 \text{ nsec}$, the SiO_2 and Si substrate are absorbing most of the film's thermal energy. Finally at $t = 20 \text{ nsec}$, only 10 nsec after the heating pulse is turned off, the temperature begins to distribute uniformly throughout the trilayer. Figure 6 shows the radial temperature distribution on the TbFe and SiO surface for the same four instants of time. The radial distribution of the temperature in the TbFe layer is rather uniform for all

instants of times.

Figure 5.6 shows the pulse width dependence of the power and energy densities necessary to reach the appointed temperature of 90 °C, for three patterned films with different diameters of 2, 0.8 μm, and 0.2 μm. Three distinct zones characterizing the heating process are observed. In zone I, the energy density becomes almost independent of the pulse width and cell size, as shown in Fig. 5.6 (b), which would correspond to the situation of a fully isolated system in an adiabatic process, because the generated heat is essentially confined to the TbFe layer. In this process, the heat transfer equation can be simplified to $P = c\Delta T / \Delta t$. Here P is power density. Thereby, the temperature increase, ΔT , is dominated only by the energy density applied and the specific heat capacity of the metal layer. Then the energy density necessary for $\Delta T = 65$ °C increases with pulse width. When the pulse width ranges from 2 to 100 ns (zone II), the energy density begins to increase with pulse width in the energy density plot. In this zone, the thermal diffusion length λ ($= \sqrt{2k_n \Delta t / c_n}$) is estimated to be shorter than the thickness of the SiO₂ layer (500 nm). Therefore, the heat dissipation is essentially confined to the SiO₂ layer that has low thermal conductivity. For the two larger patterned films ($\phi = 2$ and 0.8 μm), the diameter of the heat source is larger than or comparable to the thermal diffusion length λ , which means that heat diffusion along the film normal direction becomes significant rather than the diffusion in the in-plane direction. The difference in the required power/energy density for the same pulse width between $\phi = 2$ and 0.8 μm patterned films is minor. However, this difference between two large-pattern films and small-pattern films ($\phi = 0.2$ μm) becomes significant when the pulse width increases from 20 to 100 ns in zone II. It is described by the fact that heat begins to diffuse into



(a)



(b)

Fig. 5.6. (a) Power density and (b) energy density necessary to reach predetermined temperature of 90°C plotted as a function of pulse width, for patterned films with diameters of 0.2, 0.8, and 2 μm .

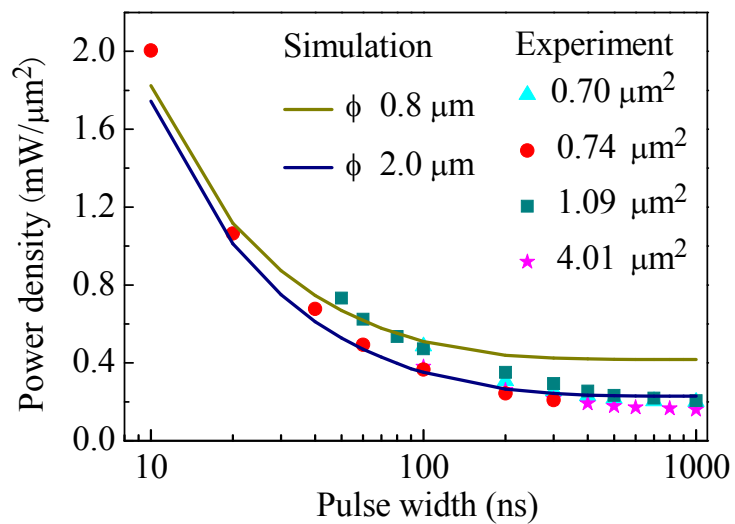
the SiO₂ layer obviously three-dimensionally when the pulse width is more than 20 ns for 0.2 μm patterned films. With a further increase of the pulse width (> 100 ns) in zone III, the heat will flow into the high-thermal-conductivity Si layer through the SiO₂ layer. This causes the required power density to decrease slowly with the increase of pulse duration. When the pulse duration is more than 300 ns, the whole system reaches a quasi-steady state corresponding to an equilibrium between Joule heating and heat flow into the substrates. For the heat diffusion process, our simulation data show that the fitting of the required writing power density in each zone can be expressed as:

$$P(t) = P_0 - \Delta P(1 - \exp(-(t - t_0)/t_i)) \quad (5.4)$$

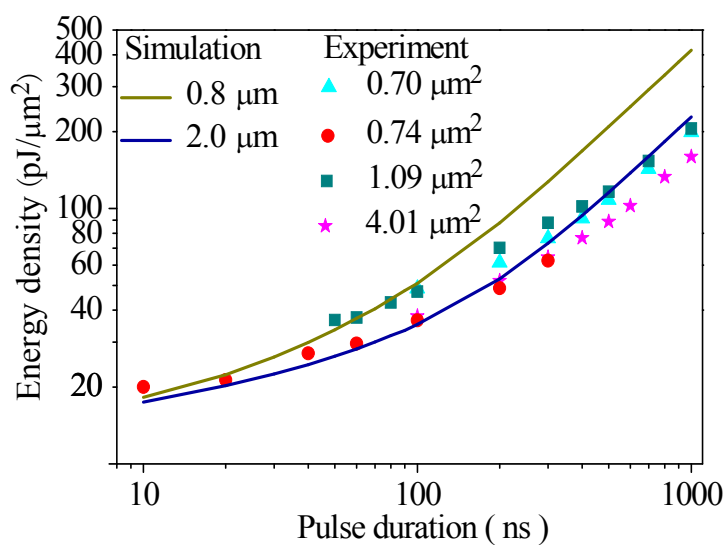
where $P(t)$ is the required write power density for pulse width t , P_0 is the write power density at the beginning time of specific zone t_0 , ΔP is the power density decrease due to the contribution from the heat dissipation into SiO₂ / Si, and t_i is the characteristic time. The characteristic time t_i is estimated to be about 4.0 and 80 ns for zones II and III, respectively, in this case.

5.4 Pulse width dependence

The power density necessary to write the patterned TbFe films was measured in the manner as described in chapter 4. Figure 5.7 shows the comparison of the dependence of the required power/energy density on the pulse width between experiment and simulation. In the experiment, the required power densities decrease and the energy densities increase with increasing pulse duration, which agrees well with the simulation. We believe that the present experimental results fall in the range of zones II and III in the simulation. The characteristic times of zones II and III can be evaluated from the fit of the function to the experimental data and are about 20 and 150 ns, respectively. From



(a)



(b)

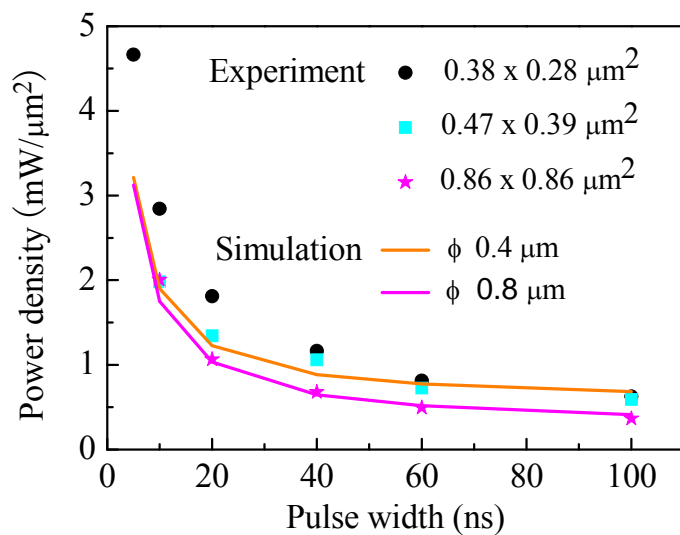
Fig. 5.7. Measured and simulated write (a) power density and (b) energy density as a function of pulse width.

the Fig. 5.7, we can see that the difference of required power/energy density between

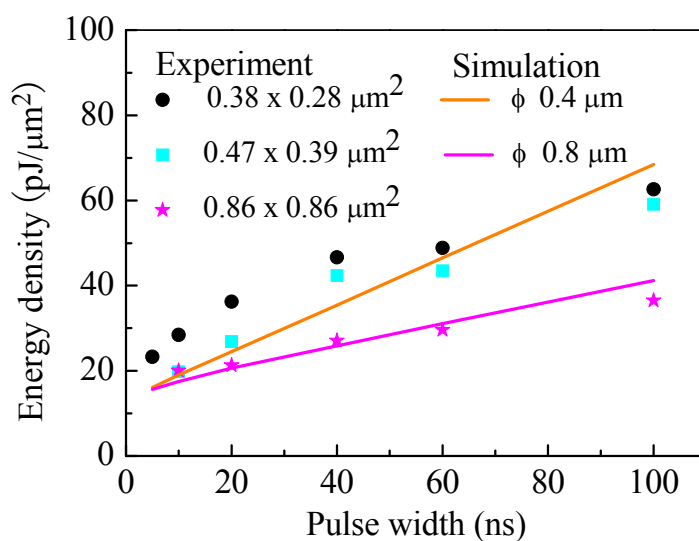
the experiment and simulation is minor when the pulse width less than 300 ns, but this difference becomes obvious with further increase of the pulse width. This is due to the fact that the current pulse also flows the lead and produces the heat during the thermomagnetic writing. Thereby, the temperature increase of the leads elevates the substrates temperature for long current pulse.

The required power density for writing using the pulse duration of 10 ns is estimated to be around $P = 2 \text{ mW}/\mu\text{m}^2$, which corresponds to the energy density of $E = 20 \text{ pJ}/\mu\text{m}^2$, which is much smaller than the values for writing using the switching of exchange bias ($P \sim 100 \text{ mW}/\mu\text{m}^2$, $E \sim 100 \text{ pJ}/\mu\text{m}^2$) reported in ref. 14. In ref. 14, the junctions are sandwiched by the top and bottom metallic leads, resulting in the large required power density. The present experiment on the TbFe layer can be regarded as a case of good thermal isolation, so we can conclude that writing using a small power of $\sim 2 \text{ mW}/\mu\text{m}^2$ is possible for the thermally assisted scheme.

The thermomagnetic writing on the patterned film of deep submicron was employed and the pulse duration dependence was also studied. The dependence of the required power/energy densities on the pulse width from experiment and simulation is shown in Fig. 5.8. For a given temperature increase and patterned film, we can know that the required energy density is only determined by the heat dissipation from the heat diffusion equation. For the two deep submicron ($0.38 \times 0.28 \mu\text{m}^2$ and $0.47 \times 0.39 \mu\text{m}^2$) patterned films, the energy density increases quickly with the pulse width compared to the case of the submicron ($0.86 \times 0.86 \mu\text{m}^2$) patterned film, which might be related to the size of the patterned film and the heat diffusion length in the SiO_2 for a given pulse width. As mentioned in 5.3, heat diffusion length in SiO_2 at 100 ns is estimated to be 420 nm which is almost equal to the lateral size of the small patterned films. This means



(a)



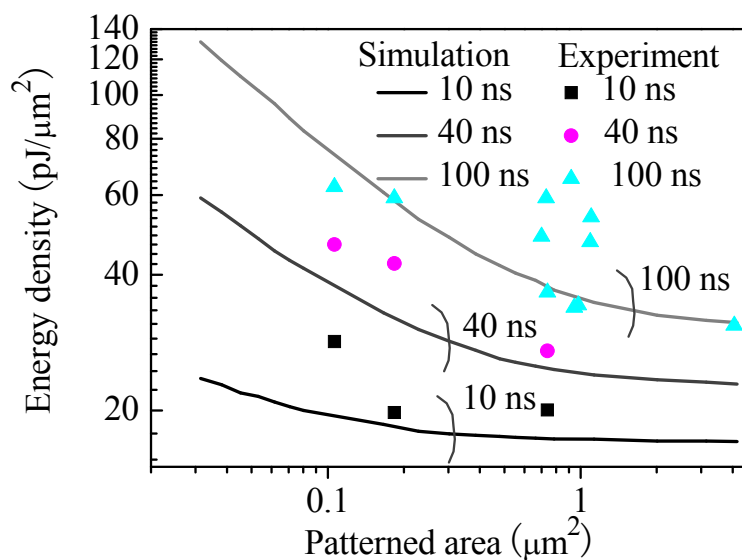
(b)

Fig. 5.8. Required (a) power density and (b) energy density plotted as a function of pulse width from the experiment for patterned films with the size of $0.38 \times 0.28 \mu\text{m}^2$, $0.47 \times 0.39 \mu\text{m}^2$ and $0.86 \times 0.86 \mu\text{m}^2$, and from simulation for Φ 0.4, and 0.8 μm patterned films.

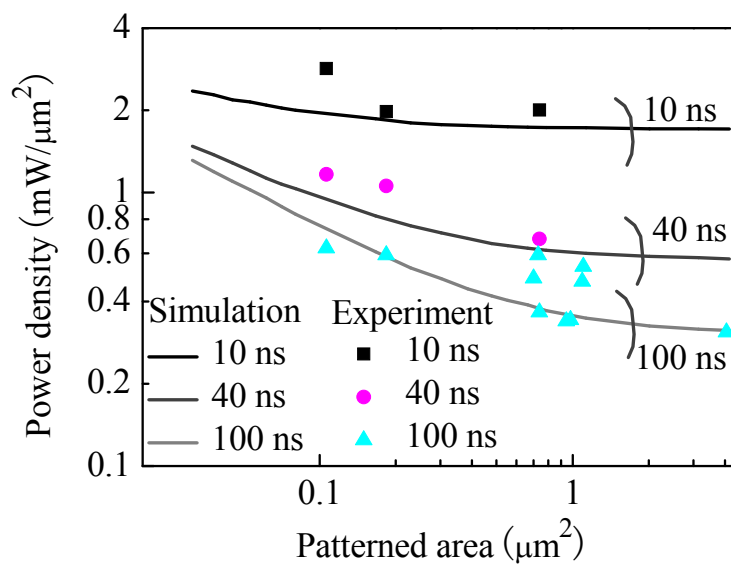
that the heat diffuses into SiO₂ layer three dimensionally. While, in the large patterned film, the heat diffuses rather one dimensionally, and thus small energy density is considered to be sufficient to increase the temperature of the patterned films up to writing temperature (Curie temperature). In the investigated range of pulse width (from 10 ns to 100 ns), we found that the required power/energy density from experiment agrees well with that from simulation.

5.5 Size dependence

The required power for a given pulse width also depends on the patterned film size. The heating power and energy densities as a function of the patterned film area are shown in Fig. 5.9 plotting the experimental data together with the simulation results. It can be seen that required write power/energy density increases as the patterned film area is scaled down. This is observed in both experimental and simulation results. When the dimension of the patterned film is much larger than the heat diffusion length at a given pulse width, the dependence of the required power/energy density on the patterned area becomes insignificant since the heat diffusion could be approximated as one dimensional heat flow. The experimental results agree well with the simulation. The difference in the required power/energy density between the experiment and the simulation will be associated with the heat diffusion into leads, which is not taken into account in the simulation, and the stray field from leads comprised of TbFe alloys. This stray field cannot be neglected compared to the external field (100 Oe) when the surface area becomes very small. We should note that the required energy density for short pulse writing (10 ns) is much smaller than that for long pulse writing (40 and 100 ns)



(a)



(b)

Fig. 5.9. Measured and simulated (a) power density and (b) energy density required for the writing of various sized patterned films. The results for pulse widths of 10, 40, and 100 ns are shown.

and the dependence of the power/energy density on the patterned area becomes insignificant.

The power and energy densities required for the writing using 10 ns pulse are roughly $2 \text{ mW}/\mu\text{m}^2$ and $20 \text{ pJ}/\mu\text{m}^2$, respectively, which is comparable to the value for the thermally assisted writing of the MTJ with a thermal isolation layer [15]. If we assume the tunneling junction resistance of $RA \sim 100 \Omega \cdot \mu\text{m}^2$ for making the MTJ using the TbFe memory layer, the current density to achieve the power density of $2 \text{ mW}/\mu\text{m}^2$ is estimated to be around $4.5 \times 10^5 \text{ A}/\text{cm}^2$. This value is less than the critical current density obtained in the spin transfer switching of the MTJ with moderate thermal stability [16], which indicates that the thermally assisted writing at low heating current density will be possible even in deep submicron sized MTJ.

5.6 Conclusion

In this chapter, we studied the dynamic heating of patterned TbFe in the thermomagnetic writing scheme using current pulses. Using an alternating-direction implicit thermal simulation, we found that the energy density required for writing was kept constant at about $13 \text{ pJ}/\mu\text{m}^2$, associated with adiabatic regime, when the pulse width was less than 2 ns.

The effect of pulse width and patterned film area on the required heating power/energy densities was investigated by the experiment and the thermal simulation. The required power densities decrease and the energy densities increase with increasing pulse duration. This is observed both in experimental. The simulation agrees well with the experiment result for the micron, submicron even deep submicron narrow path when the pulse width less than 300 ns. But the difference of the required power/energy density

between the experiment and simulation results becomes obvious when the pulse width more than 300ns, which is due to the heating produced by the leads.

The effect of patterned film area on the required heating power/energy densities was also studied by both the experiment and the thermal simulation. In the case of long current pulse of 100 ns, the heat diffuses predominantly into the SiO₂ layer, which results in large variation of required power/energy density with the patterned area. While for the short current pulse width of 10 ns, the required power/energy density becomes rather independent on the patterned area. We can conclude that perpendicularly magnetized RE-TM alloys are expected to be a thermally assisted MRAM cell which is possible to write at low heating current density even in a deep submicron sized cell.

References

- [1] W. D. Doyle, G. K. Goldbrg, and W. E. Flannery, *IEEE Trans. Magn.*, **6** (1970) 548.
- [2] B.G. Huth, *IBM J. Res. Develop.*, **18** (1974) 100.
- [3] M. Mansuripur and G. A. N. Connell, *J. Appl. Phys.*, **55** (1984) 3049.
- [4] M. Takahashi, N. Ohta, S. Takayama, Y. Sugita, M. Yoshiro, and K. Shigematsu, *IEEE Trans. Magn.*, **22** (1986) 931.
- [5] M. Mansuripur and G. A. N. Connell, *J. Appl. Phys.*, **61** (1987) 3334.
- [6] P. Hansen, *J. Appl. Phys.*, **62** (1987) 216.
- [7] J.C.Suits, D. Rugar, and C. J. Lin, *J. Appl. Phys.*, **64** (1987) 252.
- [8] M. Mansuripur, G. A. N. Connell, and J. W. Goodman: *Appl. Opt.*, **21** (1982) 1106.
- [9] X. Xun, C. Peng, and M. Mansuripur: *Appl. Opt.*, **39** (2000) 4355.
- [10] X. Xun, C. Peng, and M. Mansuripur: *Appl. Opt.*, **41** (2002) 4596.
- [11] J. C. Suits, D. Rugar, and C. J. Lin: *J. Appl. Phys.*, **64** (1988) 252.
- [12] F. A. Bout, J. A. Mittereder, W. T. Anderson, and D. E. Ioannou: *Solid-State Electron.*, **46** (2002) 123.
- [13] R. J. Anderson: *J. Appl. Phys.*, **67** (1990) 6914.
- [14] R. C. Sousa, M. Kerekes, I. L. Prejbeanu, O. Redon, B. Dieny, and J. P. Nozières, *J. Appl. Phys.*, **99** (2006) 08N904.

-
- [15] S. Cardoso, R. Ferreira, F. Silva, and P. P. Freitas : J. Appl. Phys., **99** (2006) 08N901.
- [16] Z. Diao, A. Panchula, Y. Ding, M. Pakala, S. Wang, Z. Li, D. Apalkov, H.Nagai, A. Driskill-Smith, L.Wang, E. Chen, and Y. Huai, Appl. Phys. Lett., **90** (2007), 32508.

Chapter 6

General Conclusion

The studies performed in the framework of this thesis were focused on the thermomagnetic writing on patterned TbFe films for MRAM application. This thesis mainly study on materials properties of RE-TM alloys, perpendicular MTJ comprised of RE-TM films and thermomagnetic writing on the patterned TbFe. This study indicates the possibility that future MRAM has high thermal stability and low power consumption. Therefore, this study gives the results that the thermally assisted MRAM is one of the promising candidates for the high density MRAM.

In chapter 1, the issues in conventional memory technique has been briefly presented. Numerous emerging memory technologies have shortly been described. MRAM have been emphasizezely discussed as one of the candidates for the so-called universal memory. Thermally assisted MRAM have been introduced to improve the thermal stability, write selectivity and power consumption in MRAM applications. RE-TM alloys have been considered as the candidate materials for thermally assisted perpendicular MRAM. The purpose of the present study is the investigation of perpendicular MTJ using RE-TM alloys and thermomagnetic writing on patterned TbFe

films, aiming to realize the thermally assisted perpendicular MRAM using RE-TM alloys.

In chapter 2, the sample deposition, microfabrication techniques and measurement methods have been introduced. RF magnetron sputtering used in this study has been introduced. The lithography (including photo- and EB lithographies) and etching/liftoff techniques have been described in detail. The process of microfabrication has been listed. The methods of the measurements on magnetic properties, microstructure, and spin transport properties used in this study have been described.

In chapter 3, the magnetic properties, their temperature dependence and spin polarization of RE-TM alloys have been discussed. In particular, TbFe has been investigated in this study. TbFe alloys have various unique properties for thermomagnetic writing, such as high perpendicular anisotropy, tunable Curie temperature and strong temperature dependence of coercivity. The magnetic properties are also sensitive to the composition due to the ferrimagnetic ordering of the RE and TM moments. The p-MTJ comprised of TbFe was fabricated using lithography technique and their spin dependent tunneling has been studied. Using a CoFe interlayer between TbFe and AlO barrier a TMR around 12% can be achieved at room temperature. The TMR is expected to be improved by optimization of the interlayer thickness and fabrication process. The potential high TMR, as well as the tunable coercivity with temperature, amorphous structure and high uniaxial anisotropy of RE-TM alloys make them promising candidates for thermally assisted MRAM.

In chapter 4, the MFM has been introduced to investigate the domain structure of the patterned films. MFM measurement has been performed to study the magnetic reversal of patterned film during thermomagnetic writing. The patterned TbFe films

have been fabricated by photo-lithography and EB lithography, followed by etching process. From the MFM image taken just after the micro fabrication, the magnetic domain structure was only observed in narrow path and lead regions, and no magnetic contrast has been seen in the etched region, which means the successful fabrication of TbFe patterned film. Thermomagnetic writing was performed on micro-fabricated TbFe film by applying a current pulse to the film itself under the external field. The dependence of required power and energy densities on the patterned film size, pulse width and writing field was investigated. The dependence of the heating power/energy density on the pulse width was experimentally measured for pulse widths ranging from 5 up to 1000 ns. For all the elements, the required power densities decrease and the energy densities increase with increasing pulse duration. The required power density for writing using the pulse duration of 10 ns is estimated to be around $P = 2 \text{ mW}/\mu\text{m}^2$, which corresponds to the energy density of $E = 20 \text{ pJ}/\mu\text{m}^2$. Thermally assisted switching at low power density ($\sim 4.7 \text{ mW}/\mu\text{m}^2$) and energy density ($\sim 23 \text{ pJ}/\mu\text{m}^2$) is found to be possible for deep submicron patterned RE-TM alloys using a 5 ns current pulse. The required energy density for short pulse writing (10 ns) is much smaller than that for long pulse writing (40 and 100 ns) and the dependence of the power/energy density on the patterned area becomes insignificant. The required power and the energy densities decrease with increasing writing field for all patterned films.

In chapter 5, we have studied the dynamic heating of patterned TbFe in the thermomagnetic writing scheme. Using an alternating-direction implicit thermal simulation, we have found that the energy density required for writing was kept constant at about $13 \text{ pJ}/\mu\text{m}^2$, associated with adiabatic regime, when the pulse width was less than 2 ns. The effect of pulse width and patterned film area on the required

heating power/energy densities was investigated by the experiment and the thermal simulation. The required power densities decrease and the energy densities increase with increasing pulse duration. This is observed both in experimental. The simulation agrees well with the experiment result for the micron, submicron even deep submicron narrow path when the pulse width less than 300 ns. But the difference of the required power/energy density between the experiment and simulation results becomes obvious when the pulse width more than 300ns, which is due to the heating produced by the leads. The effect of patterned film area on the required heating power/energy densities have been investigated by the experiment and the thermal simulation. In the case of long current pulse of 100 ns, the heat diffuses predominantly into the SiO₂ layer, which results in large variation of required power/energy density with the patterned area. While for the short current pulse width of 10 ns, the required power/energy density becomes rather independent on the patterned area. We can conclude that perpendicularly magnetized RE-TM alloys are expected to be a thermally assisted MRAM cell which is possible to write at low heating current density even in a deep submicron sized cell.

The power and energy densities required for the writing using 10 ns pulse are roughly 2 mW/ μm^2 and 20 pJ/ μm^2 , respectively, which is comparable to the value for the thermally assisted writing of the MTJ with a thermal isolation layer. If we assume the tunneling junction resistance of $RA \sim 100 \Omega \cdot \mu\text{m}^2$ for making the MTJ using the TbFe memory layer, the current density to achieve the power density of 2 mW/ μm^2 is estimated to be around $4.5 \times 10^5 \text{ A/cm}^2$. This value is less than the critical current density obtained in the spin transfer switching of the MTJ with moderate thermal

stability, which indicates that the thermally assisted writing at low heating current density will be possible even in deep submicron sized MTJ.

Acknowledgements

When I first arrived at Nagoya, I was a snot-nosed kid with no background whatsoever in solid state physics and no experience on microfabrication. Having grown up a little during my time here, I've found that I'm still snot-nosed, but at least I now know a thing or two about solid state devices. There are many people who have contributed greatly along the way and I'd like to take a moment to express my sincere gratitude and appreciation.

First of all, I would like to express my gratitude to my supervisor Prof. Shigeru Tsunashima who has been a very good supervisor, advisor and mentor throughout my years at the Nagoya University. Thank you for giving me the chance to do a Ph. D in one of the best groups in the field and for always showing interest in the work I did. His continuous guidance, advice and valuable comments throughout the discussion of the results are much appreciated. His knowledge, expertise, and patience were essential for completing this work. I very much enjoyed discussing experimental and theoretical aspects of our work, always learning something new. I have benefited tremendously from many opportunities he has given to me. As your last remaining Ph.D student, I wish you the best in your remaining years at Nagoya University and in any future endeavors.

I would also like to express my sincere thanks to Prof. Satoshi Iwata of Department of Quantum Engineering, Nagoya University for his invaluable experience, cordial guidance, many insightful suggestions throughout my work and for all the help he has given me.

I am also very grateful to Prof. Hidefumi Asano of Department of Crystalline Materials Science, Nagoya University for critical reading of the manuscript and for his kindness to serve on my defense committee.

Special thanks to Ass. Prof. Takeshi Kato for his guidance and valuable advices in the progress of my research and thank you for imparting some of the wisdom of your discipline to me while managing to keep everything running smoothly, without which, it would have been impossible to complete this dissertation within the prescribed time. His broad knowledge and diligence impressed me very much.

I am very much indebted to Ass. Prof. Reiko Furuya of International Academic Exchange office, Graduate School of Engineering, Nagoya University for her kind helps in my life.

Mr. M. Kumazawa is greatly appreciated for experiment assistance and for always being ready to help with any problem in facilities.

I would like to thank secretary Ms. Chizuko Shirasawa and all staffs of Student Affairs Office, Graduate school of Engineering, especially Ms. Shina Kawazu for the efficient assistance.

I would like to acknowledge my colleague Mr. Takeshi Ichikawa for making some perpendicular MTJ discussed in section 3.5.2.5.2.

I also thank all past and present members of Spin Electronics, Solid State Devices group (Tsunashima Lab) and Quantum Nanoelectronics, Quantum Spin Devices Group (Iwata Lab), Nagoya University, who shared the best and the worst moments with me, especially those with whom I worked more closely, Ms. W. Liu, Mr. K. Makihana, Mr. K. Nakazawa, Mr. R. Niiya, Mr. T. Konagai, Mr. K. Mishima, Mr. T. Yamada, Mr. M.

Acknowledgements

Yamashita, Mr. H. Kato, and Y. Yamauchi for their help in innumerable occasions, fruitful discussions and friendship.

I would like to thank Professor Zuoyi Li and Xiaofei Yang at Huazhong University of science and technology, China, for their support, help and encourage.

I would like to thank my whole family who support me in finance, spirit and mind. Very special thanks to my father Mr. Qingnian You and my mother Ms. Yuqin Zhu, my uncle Mr. Yansheng Peng, my two elder brothers Mr. Jingyun You and Leiyun You, and my sister Ms. Lingyun You with their family, and my father-in-law Mr. Zhengyi Song and my mother-in-law Ms. Lingna Xiong for their love and their unconditional help, support and encouragement.

I never forget the ultimate and endless supports from my wife, Ms. Min Song, during my studying in Japan. Without support and encourage from her, it would be too hard to finish my Ph. D. I would like to especially thank her love, encouragement, support and willingness to assistant this entire document in its early stages.

I would also like to acknowledge the financial support from Government of Japan (offering Monbukagakusho Scholarship) and Japan Student Services Organization (offering Honors Scholarship), and COE 21st century “Information Nano-Devices Based on Advanced Plasma Science” during my studying in Nagoya University, Japan.

List of achievements

I. Papers

	Title	Journal	Authors
1	The influence of annealing on the structural and magnetic properties of C/CoCrPt/CrTi trilayer recording media	J. Magn. Magn. Mater., Vol. 208, pp. 419-423, (2004)	Zuoyi Li, Long You, Zhen Li, Xiaofei Yang, Xiaomin Chen, Fang Jin, and Gengqi Lin
2	Effect of Nb content on the microstructure and magnetic properties of CoCrPtNb/CrTi/C thin films media for glass substrate	J. Alloy. Comp., Vol. 388, pp. 293-296, (2005)	Zuoyi Li, Long You, Min Song, Xiaofei Yang, Zhen Li, Yongshi Hu, and Gengqi Lin
3	Effect of Cr and CrTi underlayers on magnetic and structural properties of CoCrPt thin film media	J. Rare Metal Mater. Eng., Vol. 34, pp. 1517-1519, (2005)	Li Zuoyi, You Long, Song Min, Yang Xiaofei, Li Zhen, Cheng Xiaomin, and Lin Gengqi
4	Study on Preparation and Properties of CoCrPtNb/CrTi/C Multilayer Films for Recording Media	J. Rare Metal Mater. Eng., Vol. 34, pp. 1802-1805, (2005)	Li Zuoyi, You Long, Yang Xiaofei, and Lin Gengqi
5	The magnetic properties of sputter-deposited and annealed CoCr/CoCrPt recording media	J. Mater. Design, Vol. 27, pp. 223-225, (2006)	Xiaofei Yang, Long You, Min Song, Gengqi Lin, and Zuoyi Li
⑥	Magnetic force microscopy study of thermomagnetic writing on micron- and submicron-patterned TbFe	Jpn. J. Appl. Phys., Vol. 46, pp. 1003-1005, (2007)	L. You, T. Kato, S. Tsunashima, and S. Iwata
⑦	Dynamic heating in micron- and submicron-patterned TbFe films	Jpn. J. Appl. Phys., Vol. 47, pp. 146-149, (2008)	L. You, T. Kato, S. Tsunashima, and S. Iwata
⑧	Thermomagnetic writing on deep submicron patterned TbFe films by nanosecond current pulse	J. Magn. Magn. Mater. (submitted)	L. You, T. Kato, S. Tsunashima, and S. Iwata

II. International Conferences

Title	Conference	Authors
1. Thin Electromagnetic Wave Absorber Containing Fe-Co Alloy for Quasi-Microwave Band	IEEE International Magnetics Conference, Nagoya, Japan, HS-03 (Apr. 4-8, 2005)	Yan Nie, Huahui He, and Long You
2. Thermomagnetic writing on deep submicron patterned TbFe films by nanosecond current pulse	52nd Conference on Magnetism and Magnetic Materials, Florida, USA, HP-04 (Nov. 5-9, 2007)	L. You, T. Kato, S. Tsunashima, and S. Iwata

III. Japan Conferences

Title	Conference	Authors
1. Thermomagnetic writing on micron and submicron patterned-TbFe films by a current pulse	第 30 回日本応用磁気学会学術講演会, 島根大学, 11pF-4, p.112 (2006/9/11-14)	L. You, T. Kato, S. Tsunashima, and S. Iwata
2. 微細加工した TbFe 膜への電流パルスによる熱磁気書き込み	平成 18 年度電気関係学会東海支部連合大会, 岐阜大学, O-090 (2006/9/28-29)	市川剛, You Long, 加藤剛志, 岩田聡, 綱島滋
3. Dynamic heating studies in micron- and submicron-patterned TbFe films	第 31 回日本応用磁気学会学術講演会, 学習院大学, 13pC-16, p.215 (2007/9/11-14)	L. You, T. Kato, S. Tsunashima, and S. Iwata